ANALYSIS OF CONSOLIDATION AROUND DRIVEN PILES IN OVERCONSOLIDATED CLAY

by

Dimitrios G. Niarchos

Diploma in Civil Engineering (2007)
MSc in "Analysis & Design of Earthquake Resistant Structures" (2008)

National Technical University of Athens

Submitted to the Department of Civil an Environmental Engineering in Partial fulfillment of the requirements for the Degree of Master of Science in Civil and Environmental Engineering

at the

Massachusetts Institute of Technology
February 2012

Signature of Author:.....
Department of Civil and Environmental Engineering
January 20, 2012

Certified by:.....
Andrew J. Whittle
Professor of civil and Environmental Engineering
Thesis Supervisor

Accepted by:.....
Heidi M. Nepf
Chair, Departmental Committee for Graduate Students

ANALYSIS OF CONSOLIDATION AROUND DRIVEN PILES IN OVERCONSOLIDATED CLAY

by

Dimitrios G. Niarchos

Submitted to the Department of Civil an Environmental Engineering on January 20, 2012 in Partial fulfillment of the requirements for the Degree of Master of Science in Civil and Environmental Engineering

ABSTRACT

The principal objective of this thesis is to assess the capabilities of an already established analytical framework for understanding and predicting the behavior of piles driven in highly overconsolidated clays (OCR≥4). The skin friction mobilized during pile loading to failure depends on the sequence of preceding events, i.e. pile installation and soil consolidation. This research utilizes the Strain Path Method (SPM) to simulate the disturbance caused by pile installation with a general effective stress soil model, MIT-S1, which is capable of modeling adequately the anisotropic stress-strain response of clays at large OCR. Following the pile installation, one-dimensional, non-linear, coupled consolidation analyses around the pile shaft are performed using the finite element code ABAQUS, simulating the earth and pore pressure equalization. The MIT-S1 model has been integrated within the ABAQUS code.

The MIT-S1 model provides predictions of installation stresses that are generally consistent with prior work by using the MIT-E3 model. However, the research encountered several numerical problems during consolidation. Although some of these numerical issues have not been resolved, they do not appear to affect the current predictions of stresses at the pile shaft.

The main contribution of this research is the extension of the capability offered by the aforementioned analytical framework to cover highly overconsolidated clays (OCR≥4). In general, the results show that the zone of disturbance in in terms of excess pore pressures around the pile generated by the MIT-S1 model is much larger compared to MIT-E3 predictions. This discrepancy leads to different predictions between the two soil models particularly close to the pile shaft at the end of consolidation.

Thesis Supervisor: Andrew J. Whittle
Professor of Civil and Environmental Engineering

ACKNOWLEDGEMENTS

I wish to express my sincere thanks to many individuals, who helped me in my studies and research. Without their help and support, finishing up this research project would not have been possible.

In particular, I would like to thank Professor Whittle, my thesis supervisor for his constant guidance and assistance. His motivation and moral support kept me going through rough times during my master thesis by helping me keeping a sense of perspective. It has been an honor working with him.

Moreover, I would like to thank Yixing Yuan and Antonis Vytiniotis, for the contribution they offered throughout my work. Their technical insights and numerical expertise were critical to the contents of this thesis.

My deepest gratitude also extends to Dr. Lucy Jen for her advice and encouragement on several occasions regarding academic and personal problems. Her time is greatly appreciated.

Special thanks to Evangelia Ieronymaki for just being there for me.

Finally, but most importantly, I would like to thank my family for believing in me throughout this long and challenging phase of my life.

TABLE OF CONTENTS

LIST OF FIGURES

2. Methods for estimating the skin friction of driven piles

3. Steady State Pile Installation

4. Penetration Pore Pressures

LIST OF TABLES

1. INTRODUCTION

The principal objective of this work is to estimate the pore pressure dissipation and the effective stress changes after installation of a driven pile using non-linear, elasto-plastic, anisotropic constitutive models for clays. This study can be divided into two parts: i) the first outlines the analytical framework and its corresponding predictions on effective stresses and excess pore pressures during pile installation providing initial conditions for subsequent testing activities; and ii) the second performs one-dimensional, non-linear, coupled consolidation around the pile shaft simulating the earth and pore pressure equalization.

This research is motivated by the uncertainties involved in predicting the capacity and performance of friction piles driven in clays. Soil resistance is generated at the tip (point resistance) and along the shaft (skin friction). For long piles in clays, the point resistance usually represents a small fraction of the pile capacity. On the other hand, the major portion of pile capacity is derived from skin friction along the shaft, especially when no competent end bearing layer exists. Therefore, the limiting skin friction, f_s, provided by the soil is of primary importance in the design of piles.

Past research involves the formulation of analytical models which are capable of making realistic predictions of pile performance. This sustained research effort included the development of: i)integrated and systematic techniques depicting the mechanics of the pile installation process, i.e. Cavity Expansion Method (Soderberg, 1962; Vesic, 1972; Randolph & Wroth, 1979; Levadoux, 1980) and Strain Path Method (Baligh, 1985, 1986a,b); and ii) effective stress soil models (MIT-E1, Kavvadas, 1982; MIT-E3,

Whittle, 1987) which can describe realistically the constitutive behavior of K_0-consolidated clays which are normally to moderately overconsolidated (OCR≤4).

This study aims to contribute by extending the capability offered by the aforementioned analytical framework to cover highly overconsolidated clays (OCR≥4). To accomplish this goal, a third generation of effective stress models describing adequately the non-linear shear stress-strain behavior at large OCR's, MIT-S1 (Pestana, 1994), is utilized to model pile shaft performance. The results illustrate the effects of installation analysis, soil model, stress history and other factors on the limiting skin friction, f_s, which can be mobilized at the pile shaft. Predictive capabilities and limitations of the analyses are assessed from comparisons with previous analytical results and high quality field data at a number of clay sites.

This thesis consists of the following chapters. *Chapter 2* discusses existing approaches for estimating the limiting skin friction, f_s, of driven piles in clays. To begin with, a summary of the methods, i.e. empirical and rational, used to model and quantify the axial static capacity of a pile in clay is attempted. More specifically, the one-dimensional cylindrical Cavity Expansion Method (CEM) of analysis and the more sophisticated two-dimensional Strain Path Method (SPM) are described in detail. Finally a series of field experiments using extensively instrumented closed-ended steel piles is presented to identify the parameters influence the performance of driven piles.

Chapter 3 gives a brief outline of the two constitutive soil models, i.e. MIT-E3 (Whittle, 1987) and MIT-S1 (Pestana, 1994), that are used to describe the behavior of K_0-consolidated Boston Blue Clay (BBC). Using the installation analyses mentioned above in conjunction with these soil models, the values of the effective stresses in the soil

during steady pile installation are estimated. Closing this chapter, the parameters affecting the installation stresses are examined by investigating: i) the effect of method of analysis; ii) the effect of soil model; and iii) the effect of stress history.

Chapter 4 concentrates on the excess pore pressure changes at the shaft of a pile in Boston Blue Clay (BBC) during pile installation. An evaluation of the installation predictions follows by comparing the analytical results with field/laboratory measurements from several sites.

Chapter 5 summarizes the existing methods used to model and analyze consolidation analyses. Subsequently, this chapter describes the numerical algorithms used to integrate the constitutive relations of MIT-S1in the general purpose finite element code ABAQUS. Following this section, the initial distribution of the pore pressures and the effective stresses estimated in *Chapters 3 and 4* are employed to perform -dimensional, non-linear, coupled consolidation far behind the tip of a cylindrical driven pile in Boston Blue Clay (BBC).

Finally, *Chapter 6* summarizes the main conclusions and findings reached in this study.

2. METHODS FOR ESTIMATING THE SKIN FRICTION OF DRIVEN PILES

2.1 INTRODUCTION

Many offshore structures rely on driven pile foundations for supported anchorage. These deep pile foundations derive their capacity primarily from the shaft resistancce which is mobilized along the pile shaft. A rational procedure for predicting the performance of the "friction piles" may be made by systematically estimating the changes in effective stresses and properties of the soil in all three (3) distinct stages of pile penetration:

1. Pile installation
2. Consolidation around driven piles
3. Pile Loading

This chapter summarizes the existing empirical approaches for assessment of the axial static capacity of a pile in clay. Rational methods attempt to model and quantify the complex stress changes occurring during pile installation, when severe straining of the soil takes place. Subsequently, a summary of the stress fields resulting from the one-dimensional cylindrical Cavity Expansion Method of analysis and the more sophisticated two-dimensional Strain Path Method is introduced. Finally, a series of field experiments using extensively instrumented closed-ended steel piles is presented to outline the parameters influence the performance of driven piles.

2.2 EMPIRICAL APPROACHES

Rational estimates of the limiting skin friction along pile shafts are difficult to obtain because of the very complicated mechanism of pile-soil interaction. Therefore, early design methods relied solely on empirical approaches. Empirical methods equate the limiting skin friction to a measurable or quantifiable initial parameter, such as the undrained shear strength or vertical effective stress, by a factor derived from pile load tests. These methods can be broadly classified into total stress, effective stress or mixed approaches.

2.2.1 Total Stress Approach: the α method

In total stress methods, the limiting skin friction, f_s, is expressed as a fraction of the undrained shear strength, s_u, of the virgin clay,

$$f_s = \alpha \cdot s_u \tag{2.1}$$

where, α is an empirical parameter back-figured from the results of pile load tests. Therefore, the parameter α combines the effect of all factors affecting the limiting skin friction, e.g. the type of clay, dimensions and method of installation of the pile, tome effects, etc.

Terzaghi & Peck (1967) indicate that the soil adjacent to a pile driven into soft clay becomes stronger than the surrounding soil because of the consolidation. They suggest that α equals to unity when the undrained shear strength is determined by means of unconfined compression tests on clay samples (recovered prior to pile driving).

Peck (1958) and Woodward et al. (1961) recommend different values of α (*Figure 2.1*) mostly based on pile load tests in stiff clays (s_u>0.75 TSF). In the same figure, the American Petroleum Institute (API) recommended curve is also shown. It can be seen that the values of α decrease from 1.0 for soft clays (s_u<0.25 TSF) to 0.5 in stiff clays (s_u>0.75 TSF).

Tomlinson (1971) provides design values of the parameter α for piles driven into stiff clays, as shown in *Table 2.1* and *Figure 2.2.*

Flaate (1968), after a comprehensive analysis of a number of pile load tests, suggests that α depends not only on the average undrained shear strength of the clay, but also on the plasticity index, I_p, as shown in *Figure 2.3.*

Flaate & Selnes (1977) compiled results of 44 pile load tests performed mainly on timber piles (length 8-16 m) driven into soft to medium Norwegian clays, and compared the unit average shaft resistance (after subtracting the estimated point resistance) with values of the undrained shear strength measured by means of the field vane test. *Figure 2.4* presents their data and clearly indicates that significant scatter and uncertainty exist in the selection of an adequate value of α (0.4<α<1.6).

A large database, consisting of over a thousand axial load tests on piles, has been assembled under the auspices of API. This database has been used by Randolph & Murphy (1985) as a basis to formulate and assess a new method for calculating the factor α. *Figure 2.5* shows the selected correlations between α and the undrained shear strength, s_u, that fit the experimental data best.

2.2.2 Effective Stress Approach: the β method

It is widely accepted that soil failure is controlled by effective stresses. Therefore, it appears reasonable to estimate the limiting skin friction of piles by means of effective stress methods.

Several authors (Zeevaert, 1959; Eide et al., 1961; Chandler, 1968) proposed equations of the following form estimating the limiting skin friction of driven piles in cohesive soil.

$$f_s = K \cdot \tan\varphi' \cdot \sigma'_{vo} \tag{2.2}$$

where, K is a earth pressure coefficient relating horizontal to vertical effective stresses, φ' is an effective friction angle, equal to the pile-soil interface friction angle, δ' for failure at the interface and σ'_{vo} is the in situ vertical effective stress.

Although this is a reasonable approach, the determination of the coefficient, K, is very complicated. Burland (1973) assumed that the original 'at rest' value (K_0) is a lower bound and, ignoring subsequent changes of stress during pile loading, suggested the relationship:

$$f_s = K_o \cdot \tan\varphi' \cdot \sigma'_{vo} = \beta \cdot \sigma'_{vo} \tag{2.3}$$

Values of the empirical factor β were back-figured from a large number of load tests on concrete, timber and steel piles of lengths up to 50 ft driven in soft to medium clays, giving a range of values of 0.25 to 0.40 with an average of 0.32.

After reviewing data from pile load tests performed by various investigators, Meyerhof (1976) showed that the factor β decreases with the pile length as shown in

Figure 2.6. Meyerhof therefore concluded that in soft and medium clays (e.g. normally consolidated and lightly overconsolidated) deposits the factor β is a function of the overconsolidation ratio, OCR.

2.3 RATIONAL APPROACHES

It is widely accepted that effective stresses control the shear strength of soils. Thus, rational approaches for estimating the limiting skin friction, f_s, attempt to estimate the effective stresses controlling the shearing resistance along pile shafts. A rational approach to deep penetration requires an analytical framework, capable of predicting the soil disturbances around the pile.

The theoretical analysis of penetration remains a very challenging class of problem due to the high gradients of the field variables (displacements, stresses, strains and pore pressures) around the penetrometer, the large deformations and strains in the soil, the complex constitutive behavior of soils (non-linear, inelastic, anisotropic and time dependent material behavior), and the non-linear penetrometer-soil interface characteristics.

All existing theoretical solutions make several simplifying assumptions regarding the soil behavior, the failure mechanism and/or the boundary conditions. Two approximate theoretical methods for the simulation of the installation process have been proposed. Both of these approaches assume kinematic constraints such that the strains in the soil around the pile can be estimated without considering the stress-strain properties.

1. Cavity Expansion Methods (CEM): These methods are widely utilized approach for estimating penetration effects. CEM assume that during the pile installation, the soil is displaced by an expanding cavity (cylindrical or spherical shape). The changes in stresses and pore pressures are predicted using either closed-form solutions (e.g. Soderberg, 1962; Vesic, 1972; Randolph & Wroth, 1979; Levadoux, 1980) or numerical finite element solutions (Randolph et al., 1979).
2. Strain Path Method (SPM; Baligh, 1985): This method assumes that the soil moves relative to the pile tip in the same manner of incompressible, inviscid fluid flow around the tip and that this flow pattern is independent of the shearing resistance of the soil. The flow streamlines are used to determine a set of strain paths for all elements surrounding the penetrometer.

Apart from these two theoretical approaches, three novel numerical methods have recently been proposed to solve the cone penetration problems. These methods include:

1. Dislocation methods (Elsworth, 1991 &1993): This model simulates penetration effects by integrating fundamental solutions for a point dislocation in a poro-elastic medium (i.e., it is limited to assumptions of linear elastic stress-strain behavior).
2. Lagrangian formulation (Abu-Farsakh et al., 1997): This technique simulates penetration effects by adopting the complicated re-meshing schemes for finite element discretization.
3. Large-strain ALE formulation (van den Berg, 1992 & 1994): This technique uses an updated Lagrange approach that decouples the material displacement from the nodal displacement.

All approaches have advantages over the aforementioned theoretical techniques, since they can simulate frictional cone-soil interface as well as drained and partially drained penetration. However, they also have some disadvantages such as requirement for highly efficient interpolation schemes along with computer storage capacity, which result in a longer analysis time and higher expense.

From the summary of the above-mentioned methods together with recent analytical and experimental studies by Aubeny (1992), Lehane (1992) and Varney (1998), it has become evident that the SPM remains a promising theoretical approach for modeling cone penetration, when used in conjunction with a realistic constitutive model. Taking into consideration the above statement, the SPM, as the most appropriate method, is utilized in this study for dealing with pile installation problems. However, for the sake of completeness a specific category of the Cavity Expansion Methods, i.e. cylindrical shape, will be described briefly in the next section.

2.3.1 Cylindrical Cavity Expansion Method (CEM)

Pile installation is modeled as the undrained expansion of a long cylindrical cavity. The radial displacement, u, is the only non-vanishing component of the soil deformation vector. Thus, the infinitesimal increment of the circumferential strain at any time during cavity expansion is given by:

$$\dot{\varepsilon}_{\theta\theta} = \frac{\dot{u}}{R} \tag{2.4}$$

where, R is the current radial coordinate and $\dot{u}$ is the infinitesimal increment of u. Integration of $\dot{\varepsilon}_\theta$ between the initial (undeformed) and the final (after cavity expansion) states, gives the circumferential strain[1],

$$\varepsilon_{\theta\theta} = \ln\left(\frac{R_o}{r}\right) \tag{2.5}$$

of a soil element with radial coordinates R_o and r before and after cavity expansion, respectively. For soft soils undrained deformation is incompressible and, in this case R_o and r are related by:

$$R_o^2 = r^2 - r_o^2 \tag{2.6}$$

where, r_o is the radius of the cavity (pile) after expansion. Combining *Equations 2.6* and *2.7* we get:

$$\varepsilon_{\theta\theta} = -\varepsilon_{rr} = \frac{1}{2}\ln\left[1-\left(\frac{r}{r_o}\right)^{-2}\right] \tag{2.7}$$

$$\varepsilon_{zz} = \gamma_{rz} = \gamma_{r\theta} = \gamma_{\theta z} = 0 \tag{2.8}$$

or, using the transformed strain measures introduced in *Table 2.2* (Kavvadas, 1982):

$$\varepsilon = \mathrm{E}_1 = \mathrm{E}_3 = \mathrm{E}_4 = \mathrm{E}_5 = 0 \tag{2.9}$$

$$\mathrm{E}_2 = \frac{1}{\sqrt{2}}\ln\left[1-\left(\frac{r}{r_o}\right)^{-2}\right] \tag{2.10}$$

Thus, the strain in the soil around the pile after cavity expansion is estimated solely by considering the kinematics of the deformation, i.e. without assuming any stress-strain

[1] since $\dot{u} = -\dot{R}$

model for the soil. A soil model must, however, be used in order to compute the effective stresses corresponding to the estimated strains.

The excess pore pressures caused by the pile installation can be obtained by integrating the stress equilibrium equation in the radial direction,

$$\frac{\partial u}{\partial r} = \frac{\sigma'_{rr} - \sigma'_{\theta\theta}}{r} - \frac{\partial \sigma'_{rr}}{\partial r} \tag{2.11}$$

using the effective stresses computed based on the corresponding soil model.

The modeling of pile installation by means of the cylindrical Cavity Expansion Method is attractive because of the simplifications it offers in the analyses. However, prior studies have found limitations in predictions of stresses and pore pressures at the shaft of model piles (Morisson, 1984; Lehane, 1992; Whittle, 1992).

2.3.2 Strain Path Method (SPM)

The Strain Path Method (SPM) was developed over the period 1975-1985, by Baligh and his colleagues at the Massachusetts Institute of Technology (MIT). Their aim was to provide an integrated and systematic framework for elucidating and predicting pile foundation behavior, interpreting in situ tests, assessing sampling disturbance effects and, in general approaching "deep geotechnical problems" in a consistent and rational manner.

The principal assumption of the SPM method is that the soil deformations and strains are independent of the shearing resistance of the soil, due to the severe kinematic constraints involved in deep penetration problems, and thus can be estimated with reasonable accuracy based only on kinematic considerations and boundary conditions.

Figure 2.7 describes the necessary steps to obtain solutions by means of Strain Path Method. More specifically these steps are the following:

1. Estimate the initial stresses, $(\sigma_{ij})^{o}$, and initial pore pressure, u_o, in the soil prior to penetration.
2. Estimate a velocity field satisfying the conservation of volume (or mass) requirement and the boundary conditions. The velocity field describes the velocity (or rate of deformation) of soil particles as they move around the indenter, which is covered afterwards. For the case of a penetrometer generated by a point source of incompressible material in a uniform flow field (Simple Pile; Baligh 1985), solutions can be obtained in closed form (Baligh, 1985; Teh & Houlsby, 1989).
3. Determine soil deformations by integration along streamlines from the velocity field.
4. Compute the strain rates, ε^{o}_{ij}, along streamlines by differentiating the velocities with the respect to the spatial coordinates.
5. Integrate the strain rates, ε^{o}_{ij}, along streamlines to determine the strain path of different soil elements.
6. At this stage, and in case of undrained shearing of clays, the effective stresses can be determined from the strain path (or history) of various elements by either: (a) an effective stress approach, by determining the deviatoric stresses, s_{ij} $(=\sigma_{ij} - \sigma_{oct}\delta_{ij}$[2]$)$, (b) a total stress approach, by estimating the shear induced pore pressures, u_s, such that the effective stresses, σ'_{ij} $(=s_{ij} - u_s\delta_{ij})$ can be computed.

[2] where δ_{ij} is the Kronecker defined by:
$\delta_{ij} = \begin{cases} 1 & i=j \\ 0 & i\neq j \end{cases}$

7. Given the effective stresses, σ'_{ij}, the pore pressures, u ($=\sigma_{oct} + u_s$) are computed from equilibrium considerations. For axi-symmetric problems, the equilibrium equations in terms of effective stresses can be expressed in a cylindrical coordinate frame as,

$$-\frac{\partial u}{\partial r} = \frac{\partial \sigma'_{rr}}{\partial r} + \frac{\partial \sigma'_{rz}}{\partial z} + \frac{\sigma'_{rr} - \sigma'_{\theta\theta}}{r} \tag{2.12}$$

$$-\frac{\partial u}{\partial z} = \frac{\partial \sigma'_{zz}}{\partial z} + \frac{\partial \sigma'_{rz}}{\partial r} + \frac{\sigma'_{rz}}{r} \tag{2.13}$$

In principle, the pore pressures can be calculated by integrating in either the radial (r) or the vertical (z) direction. If the stress fields are exact, the predicted pore pressures will be independent of the integration path and the stress gradients will satisfy the relation:

$$\frac{\partial g_r}{\partial z} = \frac{\partial g_z}{\partial r} \tag{2.14}$$

This condition is satisfied if the strain paths are compatible with the model used to determine the stresses. However, from step 2, the strains are approximated using potential flow theory and are not compatible with the soil model used in Step 6.

8. Knowing u and σ'_{ij}, the total stresses ($=\sigma'_{ij} + u\delta_{ij}$) can easily be computed at every soil element.

2.3.3 Simple Pile Solution

The Strain Path Method (SPM) hinges on the assumption that soil deformations during deep cone penetration can be estimated with reasonable degree of accuracy by integrating a known velocity field. Baligh (1985) developed a velocity field, also known

as Simple Pile Solution, using a graphical technique to investigate the deep steady quasi-static undrained penetration of an axi-symmetric solid pile in a saturated, incompressible, homogeneous isotropic clay initially subjected to an isotropic state of stress.

2.3.3.1. Fundamentals of Simple Pile Solution

Consider a 3-D spherical source located at ρ=0 which discharges an incompressible material at a rate of volume V per unit time. Using a spherical coordinate system, shown in *Figure 2.8a*, the velocity components of a fluid element located at any radius ρ is given as:

$$u_\rho = \frac{V}{4\pi}\cdot\frac{1}{\rho^2};\ u_\varphi = 0 \qquad (2.15)$$

On the other hand, in a cylindrical coordinate system the non zero velocity components[3] u_ρ^o, u_z^o, are given by:

$$u_\rho^o = \frac{V}{4\pi}\cdot\frac{\sin\varphi}{\rho^2};\ u_z^o = \frac{V}{4\pi}\cdot\frac{\cos\varphi}{\rho^2};\ \rho^2 = r^2 + z^2;\ \varphi=\arctan\frac{r}{z} \qquad (2.16)$$

Figure 2.8a shows the deformation induced by a 3-D spherical source. This deformation grid is exactly the same as the deformation grid generated by a spherical cavity expansion in an incompressible material with radius ρ.

The Simple Pile Solution, shown in *Figure 2.8b*, is derived when a single spherical source discharging incompressible material at a rate (of volume) V per unit time is inserted in a uniform flow field with velocity U in the vertical direction. By superimposing a spherical source and a uniform flow with velocity U in the z direction,

[3] where the superscript "o" refers to the spherical situation

the soil particle velocity components u_r and u_z in a cylindrical coordinate system are given by:

$$u_r = u_r^o;\ u_z = U + u_z^o \tag{2.17}$$

Clearly, the addition of a uniform flow in the z direction changes only the vertical velocity by a uniform amount U. This apparently small deviation from the spherical cavity solution though causes drastic changes in soil deformations and strains.

2.3.3.2. Geometry and soil distortions

Superimposing soil velocities corresponding to a point source and a uniform flow, and using the concept of stream functions in cylindrical coordinates, Baligh (1985) showed that the stream line (or path) of a particle originally located at a radial distance r_o from the pile center line is described by the equation,

$$\left(\frac{r}{R}\right)^2 = \left(\frac{r_o}{R}\right)^2 + \frac{1}{2}\cdot(1+\cos\varphi)$$
$$\varphi = \arctan\left(\frac{r}{z}\right) \tag{2.18}$$

Figure 2.8b represents soil deformations obtained by direct substitution into *Equation 2.19* and observing soil incompressibility. In the special case of r_o=0 corresponding to soil elements initially located at the center line, *Equation 2.19* provides an analytical expression for the geometry of the penetrometer considered, the Simple Pile, having the following characteristics:

- The pile tip (r=0) is located at z=-R/2.
- Far behind the tip, the shaft radius of the Simple Pile $R \rightarrow (V/\pi U)^{1/2}$.

- Theoretically, the radius of the Simple Pile increases indefinitely but, for all practical purposes, it can be assumed to have a uniform radius equal to R from point C in *Figure 2.8b* located 4R behind the tip.

The geometry of the Simple Pile guarantees the absence of a relative normal velocity at the soil-pile interface. Practically this means that solutions presented herein correspond to a rigid pile and that soil particle velocities are in the tangential direction with respect to the pile surface.

The remaining condition required to describe the Simple Pile penetration is the boundary condition in the tangential direction, i.e. along the soil-pile interface. Trying to retain the simplicity of the analysis, it was decided that deformations and strains caused by penetration should become independent of the shearing behavior, (i.e. the problem becomes totally strain controlled). Hence, these results should be considered approximate, since they do not satisfy equilibrium everywhere in the soil. However, this is a good approximation for deep penetration problems, since soil deformations and strains are not seriously affected by the shearing characteristics of the soil (Baligh, 1985). The aforementioned solution techniques are used to determine the velocity, deformation and strains during penetration in this research project.

2.3.4 Effects of Pile Installation

Pile installation causes severe straining of the soil and drastic changes in the soil stresses. A rational estimate of the shaft resistance of piles requires that the mechanism of installation be understood and then formulated in a comprehensive method to perform predictions.

2.3.4.1. Strains in the soil during Pile Installation

In axi-symmetric problems, the strains are described by four non-vanishing components: ε_{rr}, ε_{zz}, $\varepsilon_{\theta\theta}$, ε_{rz}. Taking into account that the soil herein is treated as incompressible, the three normal strains must satisfy the condition of no volume change:

$$\varepsilon_{rr} + \varepsilon_{zz} + \varepsilon_{\theta\theta} = 0 \tag{2.19}$$

Therefore, three strain components are sufficient to fully describe the state of strain. For graphical representation of different states of strain, the E_i-space $\{E_1, E_2, E_3\}$ (Levadoux, 1980), is utilized, defined as:

$$E_1 = \varepsilon_{zz};\ E_2 = \frac{1}{\sqrt{3}}\left(\varepsilon_{\theta\theta} - \varepsilon_{rr}\right);\ E_3 = \frac{2}{\sqrt{3}}\varepsilon_{rz} \tag{2.20}$$

Figure 2.9 shows a strain point in the three-dimensional E_i-space where its distance from the origin is proportional to the octahedral shear strain γ_{oct}:

$$\left[E_1^2 + E_2^2 + E_3^2\right]^{1/2} = \sqrt{2}\gamma_{oct} \tag{2.21}$$

$$\gamma_{oct} = \frac{1}{3}\left[\left(\varepsilon_{rr} - \varepsilon_{zz}\right)^2 + \left(\varepsilon_{zz} - \varepsilon_{\theta\theta}\right)^2 + \left(\varepsilon_{\theta\theta} - \varepsilon_{rr}\right)^2 + 6\varepsilon_{rz}^2\right]^{1/2} \tag{2.22}$$

The octahedral strain, γ_{oct}, representing the second deviatoric strain invariant provides a good measure of overall shear strain levels. Furthermore, the strain paths of conventional strain controlled tests correspond to the three axes; E_1 - triaxial mode; E_2 - pressuremeter or cavity expansion mode; and E_3 - Direct Simple Shear mode, as shown in *Figure 2.9*.

Cylindrical CEM assumes conditions of radial symmetry and hence, restricts the dependence of field variables to the radial coordinate only. Therefore, the components of axial strain, ε_{rr}, and shear strain, ε_{rz}, are zero according to this method. This assumption greatly simplifies the problem and enables solutions to be obtained with a modest level of effort.

Figure 2.10 shows the radial, ε_{rr}, and the circumferential strains, $\varepsilon_{\theta\theta}$, far behind the tip of a long cylindrical pile as a function of the normalized radius, r_o/R, estimated according to the Cavity Expansion and the Strain Path[4] methods. The CEM predicts that the radial and circumferential strains are equal and opposite at all locations because the axial strain vanishes and deformation is incompressible. The predictions of the Strain Path and the Cavity Expansion methods are almost identical, indicating that the effect of the (non-zero) axial strain is small.

Figure 2.10 represents the final strain states after pile installation, and thus does not contain information for the prior strain paths followed by the individual soil elements. The strain paths predicted by the Cavity Expansion and the Strain Path methods are very different: the CEM predicts monotonic radial strain paths between the initial (undeformed) state and the final strain state (after pile installation) for all soil elements, whereas Levadoux & Baligh (1980) show that the SPM predicts large strain reversal and complicated strain paths[5], due to the effect of the pile tip which is neglected by the CEM.

[4] using a 60° tip angle

[5] especially for soil elements located close to the pile wall ($r_o/R<3$-4)

Furthermore, it is well established fact that the effective stresses around the pile are controlled by the strain paths followed during pile driving rather than the final strain states. Thus, the effective stresses predicted by both methods are expected to be different.

Figure 2.11 shows SPM projections of strain paths in (E_1, E_2) and (E_2, E_3) spaces during penetration of a Simple Pile for three soil elements initially located at r_o/R=0.2, 0.5 and 1.0 (i.e. relatively close to the pile axis). The following remarks can be made:

- The straining levels close to the pile are much greater than normally imposed in common laboratory and pressuremeter tests as illustrated by the shaded zones. Therefore, the post peak behavior of the clay should be expected to have an important effect on stresses and pore pressures in the soil close to the pile.
- Ahead of the pile, straining of the soil located near the axis takes place essentially due to E_1 (vertical compression) with possibly some contribution of E_3 well before E_2 (cylindrical cavity expansion) is felt.
- The strains caused by penetration are not monotonic. The reversal of strain paths and the high straining levels caused by penetration have a major influence on stress predictions.

Figure 2.12 shows contour lines of the octahedral strains, γ_{oct}, and strain rates, $\dot{\gamma}_{oct}$, during penetration of a Simple Pile. Further examination of this figure reveals many interesting aspects of deep penetration:

- Contour lines of γ_{oct} provide a good indication of the shearing severity in isotropic clays and conveniently divide the soil mass into an inner plastic zone and an outer elastic domain. In this case the contour of γ_{oct}=2% represents the boundary of the

plastic zone surrounding the Simple Pile in a clay obeying the Von Mises criterion for yielding at this strain level (corresponding to a strain of 4.9% in simple shear). Outside this boundary, the strains are relatively small and the soil does not reach failure and thus significant analytic simplifications are permitted.

- Contour lines of γ_{oct} far behind the tip are virtually identical to those predicted by cylindrical cavity expansion except in the vicinity of the shaft, where the amount of shearing is slightly larger during pile penetration.

The strain contours of $\dot{\gamma}_{oct}$ in case of a Simple Pile consists of spheres centered at the origin located at distance R/2 behind the tip and correspond to a pile with a radius R=1.78cm pushed with a steady velocity U=2 cm/s, as in cone penetration testing. Clearly, the soil is sheared non-uniformly and very rapidly during penetration. For example, the soil in the shaded area (*Figure 2.12*) is strained more than 14,000 times faster than undrained triaxial tests conducted at an axial rate $\dot{\varepsilon}$=0.5% per hour. Such high strain rates have important effects on soil behavior, e.g. increasing the peak strength, decreasing the strain to peak and enhancing strain softening.

2.3.4.2. Installation Stresses and Pore Pressures

Predictions of effective stresses around the pile after installation were made using the MIT-E3 model. The MIT-E3 model (Whittle, 1987) is a generalized effective stress soil model for describing the rate independent behavior of normally to moderately overconsolidated clays (OCR≤8). *Figure 2.13* presents Strain Path (SPM) and cylindrical Cavity Expansion (CEM) predictions of installation stresses and pore pressures around the shaft of a pile in K_0-normally consolidated Boston Blue Clay (BBC) (Whittle, 1993).

The individual stress components are normalized by the in situ vertical effective stress, σ'_{vo}, while radial dimensions are normalized by the radius of the pile, R. Based on these predictions the following comments can be made:

- Although both CEM and SPM predict a similar accumulation of excess pore pressures, $\Delta u_i/\sigma'_{vo}$, in the far field ($3 \leq r_o/R \leq 30$), there are differences in the distribution close to the pile ($r_o/R \leq 3$). The net result is that the CEM predicts excess pore pressures which are typically 20-25% larger than those obtained from corresponding SPM analyses.
- During installation undrained shearing generates positive shear induced pore pressures and there is a corresponding net reduction in the mean effective stress, σ'/σ'_{vo}, close to the shaft ($r_o/R \leq 6$). Differences in the magnitude of σ'/σ'_{vo} for SPM and CEM analyses reflect the differences in strain histories.
- The SPM predicts very low radial effective stresses, σ'_r/σ'_{vo}, and cavity shear stresses[6], q_h/σ'_{vo} acting at the pile shaft. In contrast, CEM analyses give higher values of radial effective stress, σ'_r/σ'_{vo}, and predict that $\sigma'_r/\sigma'_{vo} > \sigma'/\sigma'_{vo}$ over a wide radial zone ($r_o/R \leq 20$). At this point, it has to denoted that strain path predictions of σ'_r/σ'_{vo} are affected significantly by soil properties.

Figure 2.14 presents Strain Path (SPM) predictions of installation stresses and pore pressures far behind the tip of a pile in K_0-normally and lightly overconsolidated BBC (Sutabutr, 1999). The two principal parameters of interest in these analyses are the normalized excess pore pressures, $\Delta u_i/\sigma'_{vo}$, and radial effective stresses, σ'_r/σ'_{vo}, that

[6] $q_h = \frac{\sigma'_r - \sigma'_\theta}{2}$

occur at the pile shaft for overconsolidation ratios, OCR=1.0, 1.5 and 2.0. The results show the following:

- The normalized excess pore pressures, $\Delta u_i/\sigma'_{vo}$, far behind the tip of the pile increase with OCR of the soil, due to the increase in undrained shear strength ratios, s_u/σ'_{vo}.
- For normally and lightly overconsolidated clays (OCR≤2), there is a large net decrease in the radial effective stress close to the pile shaft compared to the far field K_0 condition.

2.3.5 Effects of Soil Consolidation

The shaft resistance of piles in clays increases with time due to pore pressure dissipation and soil consolidation. However, the time to reach the maximum resistance varies significantly because of different soil (e.g. permeability, compressibility) and pile (e.g. radius, permeability) conditions. Pore pressure dissipation rates are needed to estimate the time for the pile to "set up" and thus obtain its full resistance.

Figure 2.15 presents solutions for non-linear, coupled consolidation around a pile following penetration in K_0-normally consolidated BBC, based on the MIT-E3 soil model (Whittle, 1993). Installation pore pressures and stress fields are obtained from the solutions presented in *Section 2.3.4.2.* The predictions are presented using a dimensionless time factor, T, for both Strain Path and cylindrical Cavity Expansion methods. The results show the following:

- The analyses using the SPM predict a final set-up stress ratio[7], $K_c=\sigma'_{rc}/\sigma'_{vo}$, equals to $K_c=0.37$ which is significantly lower than the initial, in situ earth pressure coefficient ($K_0=0.48$).
- Predictions using cavity expansion analysis of pile installation (CEM) show higher set-up ($K_c=0.50$). This results is primarily due to the predicted initial conditions ($K_i=0.33$) since the net change in radial effective stress during consolidation is relatively small.

2.4 FIELD EXPERIMENTS USING INSTRUMENTED PILES

This section describes a series of field experiments using high-quality instrumented piles developed at Imperial College. The purpose of the pile test program was to identify the major factors controlling displacement-pile performance by providing reliable data regarding the physical processes of driven piles.

The instrumented displacement piles were equipped to measure the effective stresses acting at the pile/soil interface during the three main stages of the pile's lifetime (i.e. pile installation; consolidation; and pile loading). The general arrangement of the model pile is shown in *Figure 2.16*. The instruments, used at the three clusters located over the lower 3 m length of the pile, are described in detail by Bond et al. (1991).

The following sections evaluate the experimental data of the instrumented piles from three well-documented pile test sites: i) London clay (Bond & Jardine, 1991); ii) stiff

[7] where σ'_{rc} is the radial effective stress acting on the pile after full dissipation of excess pore pressures

glacial clay (Lehane & Jardine, 1993); and iii) soft estuarine Bothkennar clay (Lehane & Jardine, 1993).

2.4.1 London clay, Canons Park Site

The ground conditions at Canons Park comprise superficial deposits of topsoil, gravel, and silty clay head, overlying heavily overconsolidated London clay. The strength profile for the site has been established from unconsolidated undrained triaxial compression tests on thin-walled jacked samples (Jardine, 1985). In situ overconsolidation ratios range from OCR=25 at depth d=7 m to OCR=45 at depth d=3 m.

Comparing the field data with the two leading theories for predicting the behavior of displacement piles in clay soils (i.e. cylindrical Cavity Expansion Method, CEM; and Strain Path Method, SPM) the following conclusions can be drawn:

- The central assumption of the cylindrical CEM is that pile installation has the same overall effect on the ground as the monotonic expansion of a long cylindrical cavity under undrained plane strain conditions. The validity of this hypothesis can be directly tested by comparing the radial total stresses, σ_r, measured at the end of installation with limit pressures p_{lim} extrapolated from self-boring pressure-meter tests. *Figure 2.17* shows that values of σ_r at Canons Park fall well below p_{lim} values showing the inadequacy of CEM to predict the behavior of displacement piles in high OCR clay.

2.4.2 Glacial clay, Cowden Site

The United Kingdom Building Research Establishment (BRE) developed a test site at Cowden, northeast England, for research into the engineering properties of glacial tills. The BREs site investigation and laboratory testing at Cowden are summarized by Marsland & Powell (1985).

A general observation based on the field data of all instrumented sites is that the rate of penetration has a marked influence on the mobilized skin friction, f_s[8]. More specifically, *Figure 2.18* outlines this rate dependence by including data reported by Lehane & Jardine (1993) and Ponniah (1989) from other jacked piles at Cowden. The rate effect appears to be slight at pile velocities less than about 50 mm/min. However, at faster rates the trend line climbs steeply, with a maximum gradient of about 100% per logarithmic cycle, matching closely the response measured in pile tests in London clay (Bond & Jardine 1991).

2.4.3 Soft marine clay, Bothkennar Site

The UK Science and Engineering Research Council set up a soft clay test bed site at Bothkennar, Scotland, on the southern bank of the Forth estuary. The ground conditions have been investigated thoroughly using state of the art sampling, laboratory testing, and in situ test techniques. Details of these investigations were reported by Hawkins et al. (1989), Hight et al. (1992) and Smith et al. (1992).

[8] based on Total Stress Approach, $f_s=\alpha \cdot s_u$

Comparing the field data of the aforementioned test sites with the results of Bothkennar clay the following remarks related to the consolidation phase can be made:

- The radial total stress changes[9], H/H_i, observed during consolidation in *Figure 2.19* are generally reduced through time, with the greatest relative reductions taking place in the low-OCR sensitive Bothkennar clay. A wider ranging review by Lehane (1992) shows that equalized values of H/H_i decrease with increasing clay sensitivity and reducing OCR.
- The radial effective stresses, σ'_r, recorded at all instrumented sites shown in *Figure 2.20,* is normalized by the corresponding σ'_{rc} values measured at the end of the consolidation process. The pattern recognized is a large overall increase in σ'_r during consolidation at Bothkennar, a relative neutral effect at Cowden and a net reduction of σ'_r in the London clay. Taken together, these data show that the degree of set-up decreases with increasing OCR.

[9] $\frac{H}{H_i} = \left(\frac{\sigma'_r - u_o}{\sigma'_{ri} - u_o}\right)$

Case	Soil Conditions	Penetration Ratio* L/D	$a = \frac{f_s}{s_u}$
I	Sands of sandy gravels overlying stiff to very stiff clays	<20	1.25
		>20	use curve 1 in Figure 2.2
II	Soft clays or silts overlying stiff to very stiff clays	<20	0.40
		>20	0.70
III	Stiff to very stiff cohesive soils without overlying strata	<20	0.40
		>20	use curve 2 in Figure 2.2

* L = length of pile

D = diameter of pile

Note: α values are not applicable to H-section piles. s_u obtained from unconfined compression tests.

Table 2.1: Limiting skin friction values into stiff to very stiff clays (Tomlinson, 1971)

Effective Stresses $\underset{\sim}{\sigma} = (\sigma', S)$	**Strain** $\underset{\sim}{\varepsilon} = (\varepsilon, \mathrm{E})$	**Yield Surface Gradient** $Q = (Q, Q')$	**Plastic Flow Direction** $P = (P, P')$	**Anisotropy** $(1, b)$
$\sigma' = \frac{1}{3}(\sigma_x + \sigma_y + \sigma_z)$	$\varepsilon = \varepsilon_x + \varepsilon_y + \varepsilon_z$	$Q = Q_x + Q_y + Q_z$	$P = P_x + P_y + P_z$	1
$S_1 = \frac{1}{\sqrt{6}}(2\sigma_y - \sigma_x - \sigma_z)$	$E_1 = \frac{1}{\sqrt{6}}(2\varepsilon_y - \varepsilon_x - \varepsilon_z)$	$Q'_1 = \frac{1}{\sqrt{6}}(2Q_y - Q_x - Q_z)$	$P'_1 = \frac{1}{\sqrt{6}}(2P_y - P_x - P_z)$	$b_1 = \frac{1}{\sqrt{6}}(2b_y - b_x - b_z)$
$S_2 = \frac{1}{\sqrt{2}}(\sigma_z - \sigma_x)$	$\mathrm{E}_2 = \frac{1}{\sqrt{2}}(\varepsilon_z - \varepsilon_x)$	$Q'_2 = \frac{1}{\sqrt{2}}(Q_z - Q_x)$	$P'_2 = \frac{1}{\sqrt{2}}(P_z - P_x)$	$b_2 = \frac{1}{\sqrt{2}}(b_z - b_x)$
$S_3 = \sqrt{2}\sigma_{xy}$	$\mathrm{E}_3 = \sqrt{2}\varepsilon_{xy}$	$Q'_3 = \sqrt{2}Q_{xy}$	$P'_3 = \sqrt{2}P_{xy}$	$b_3 = \sqrt{2}b_{xy}$
$S_4 = \sqrt{2}\sigma_{yz}$	$\mathrm{E}_4 = \sqrt{2}\varepsilon_{yz}$	$Q'_4 = \sqrt{2}Q_{yz}$	$P'_4 = \sqrt{2}P_{yz}$	$b_4 = \sqrt{2}b_{yz}$
$S_5 = \sqrt{2}\sigma_{zx}$	$\mathrm{E}_5 = \sqrt{2}\varepsilon_{zx}$	$Q'_5 = \sqrt{2}Q_{zx}$	$P'_5 = \sqrt{2}P_{zx}$	$b_5 = \sqrt{2}b_{zx}$

Table 2.2: Transformed tensorial measures (Kavvadas, 1982)

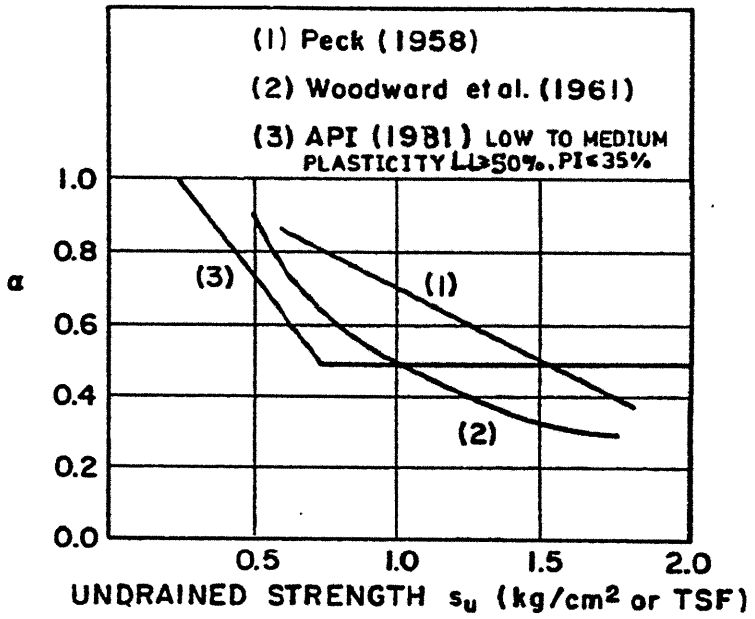

Figure 2.1: Compilation of α factor by Peck (1958), Woodward et al. (1961) & API (1975)

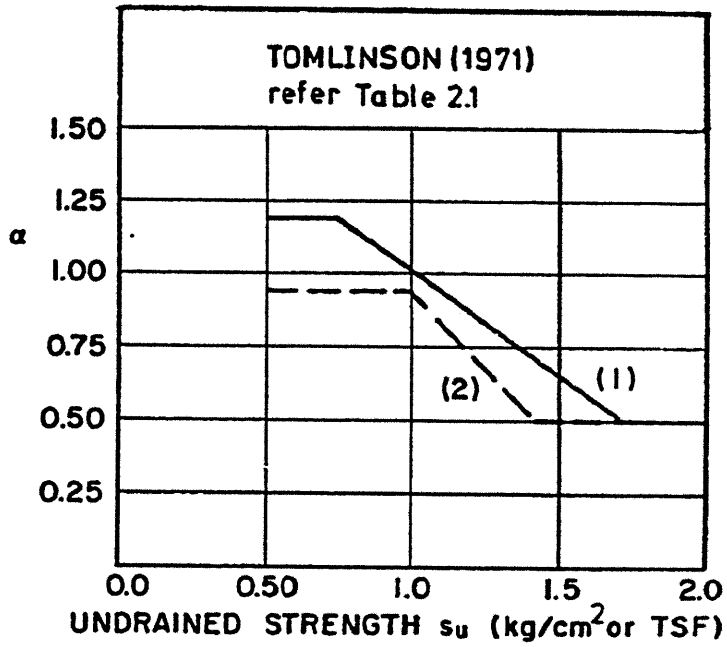

Figure 2.2: Compilation of α factors by Tomlinson (1971)

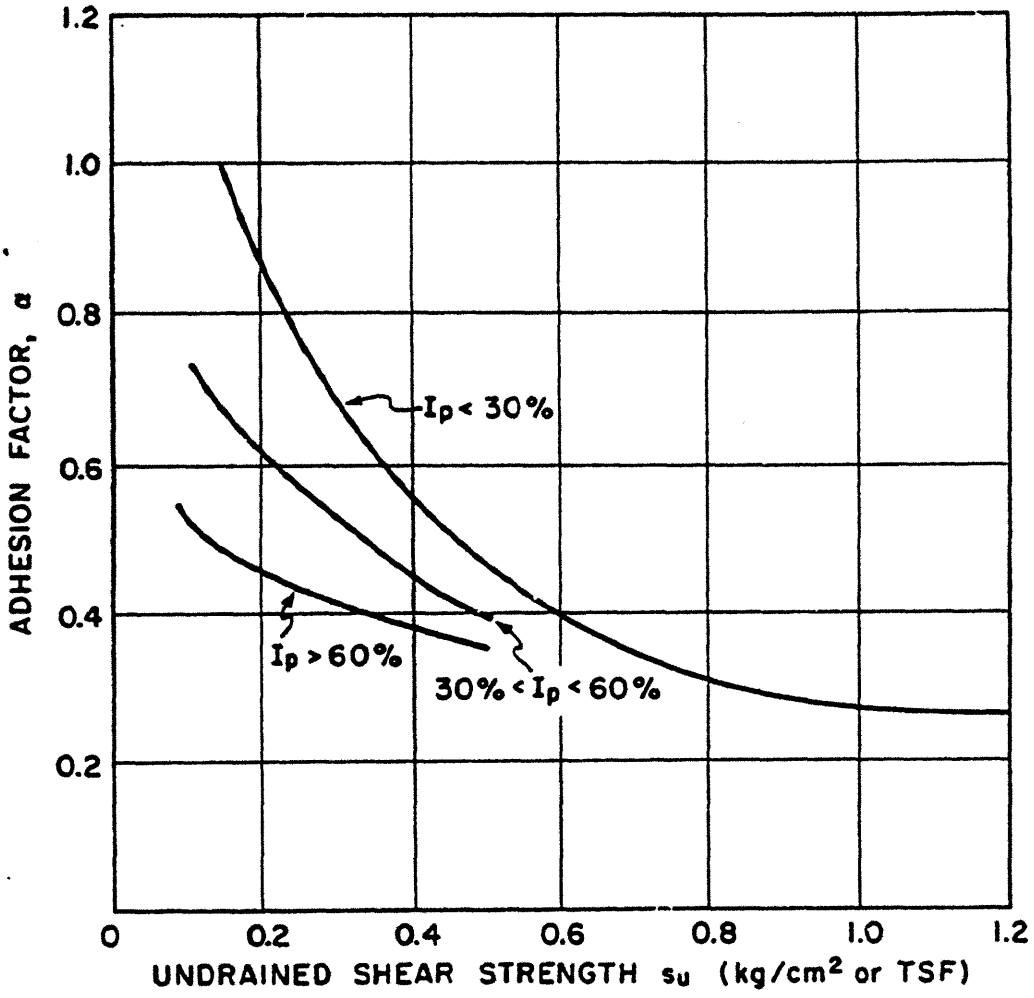

Figure 2.3: Relationship between average adhesion α factor and undrained shear strength for driven piles in clay (Flaate, 1968)

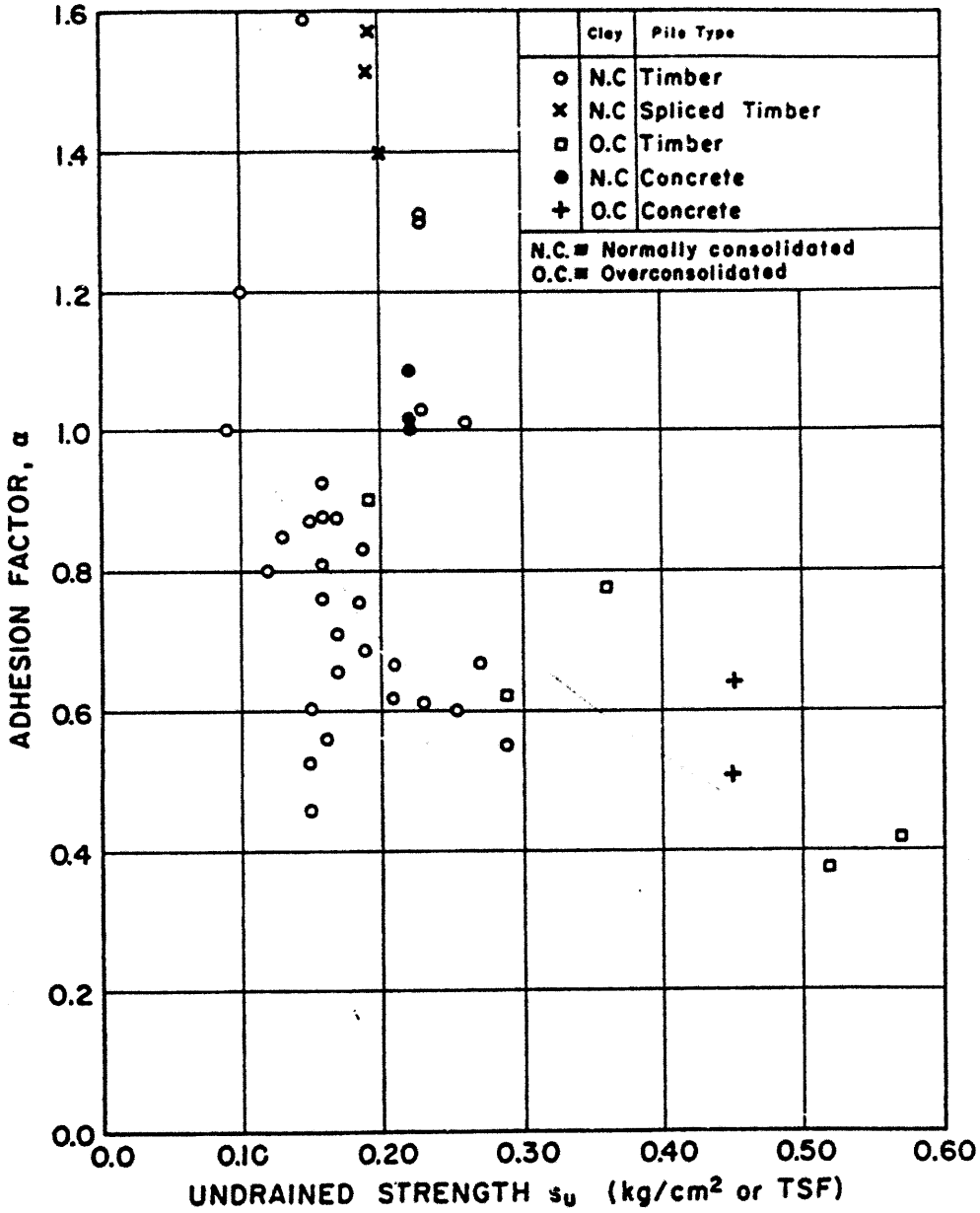

Figure 2.4: Average adhesion factor α versus s_u (Flaate & Selnes, 1977)

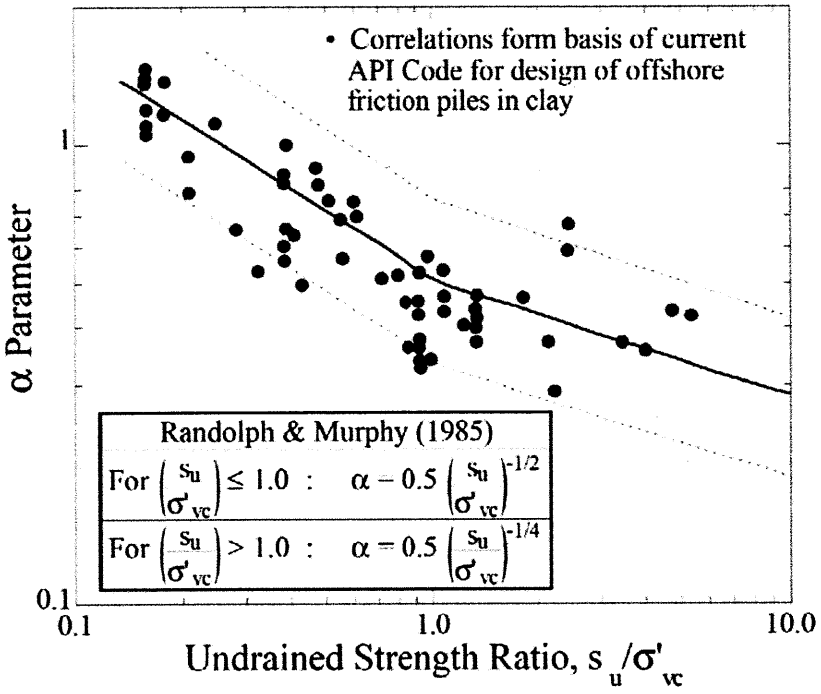

Figure 2.5: Correlations between the α factor and the undrained shear strength ratio, s_u/σ'_{vc} (Randolph & Murphy, 1985)

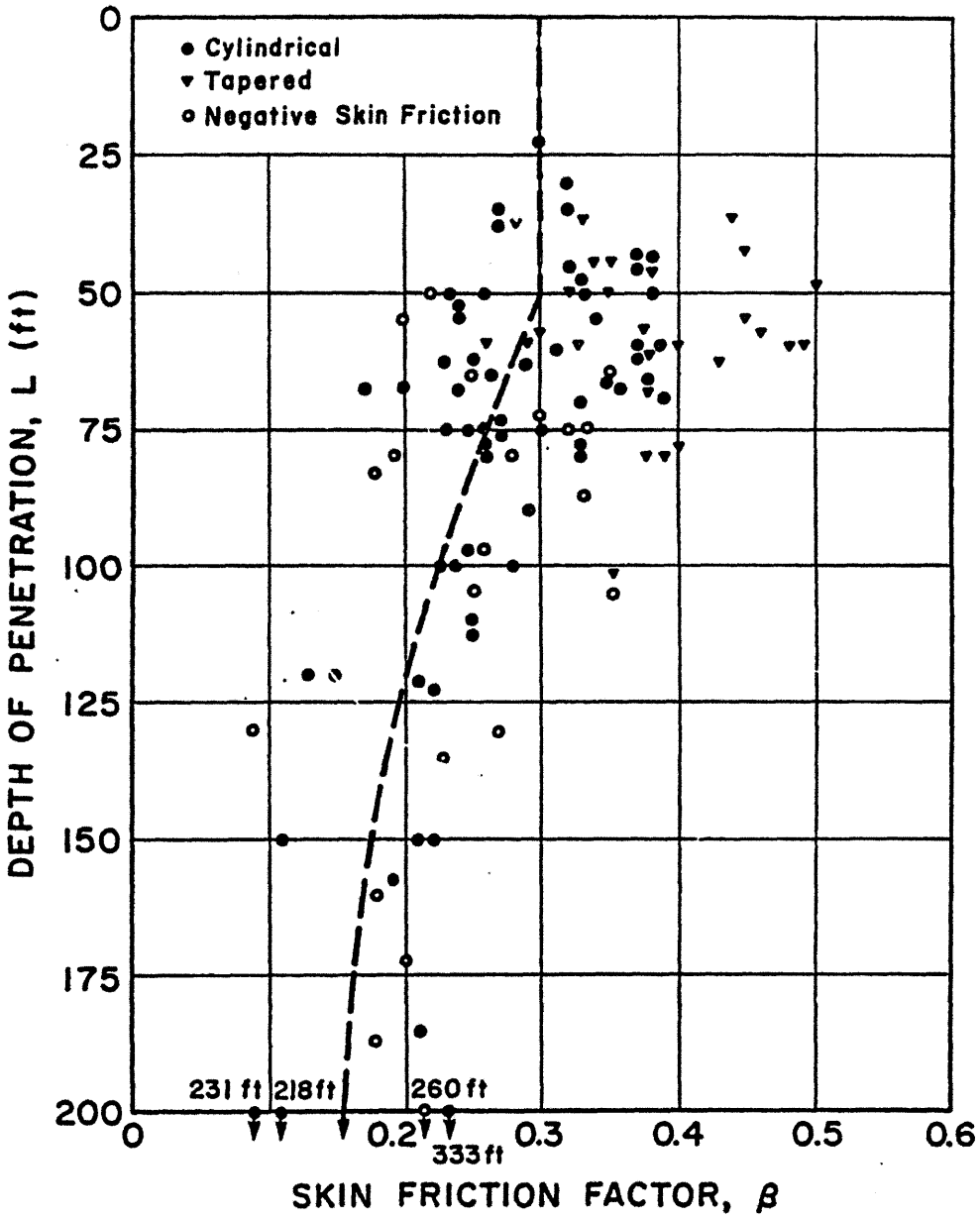

Figure 2.6: Variation of β with depth (Meyerhof, 1976)

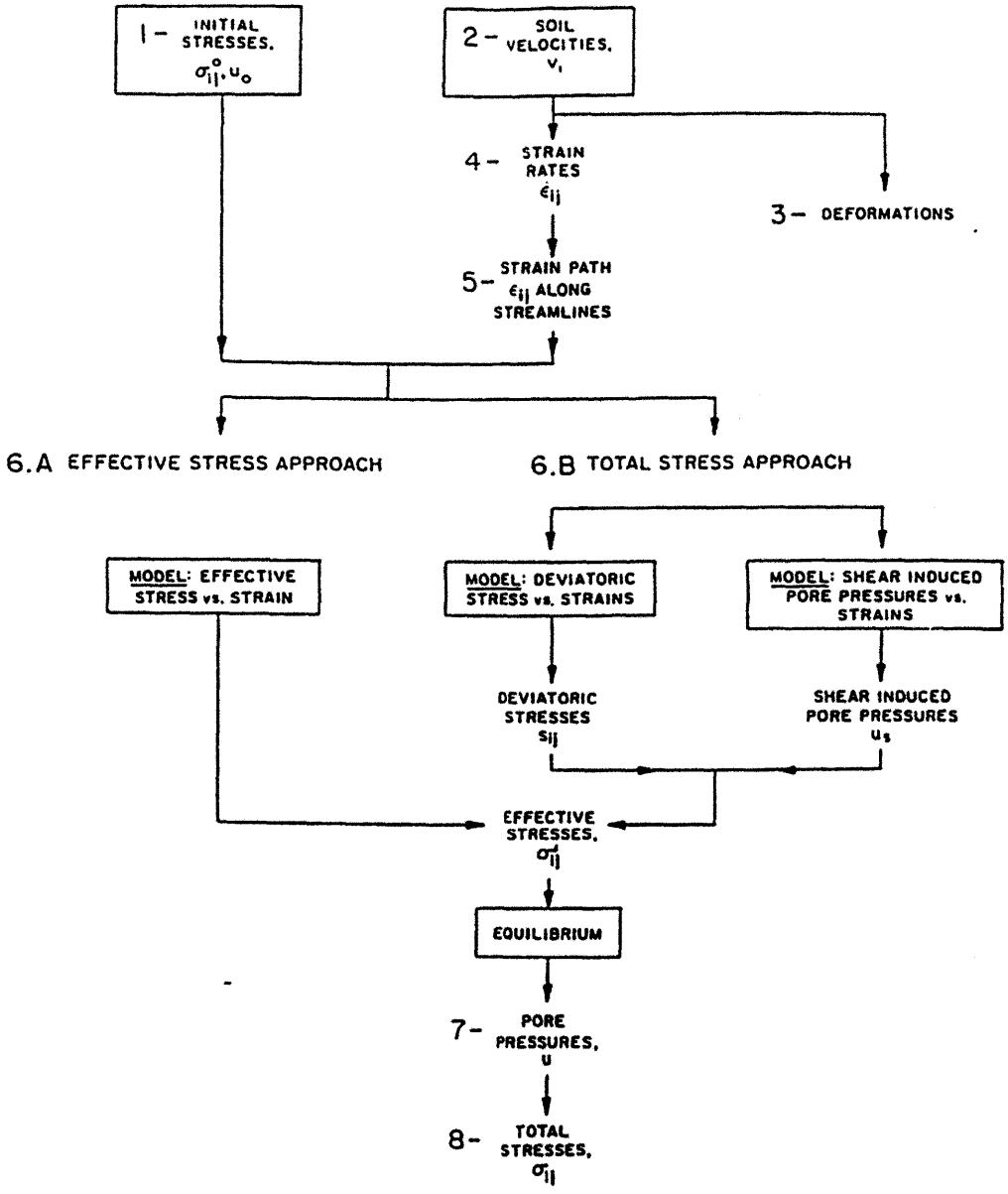

Figure 2.7: Application of Strain Path Method to deep penetration in clays (Baligh, 1985)

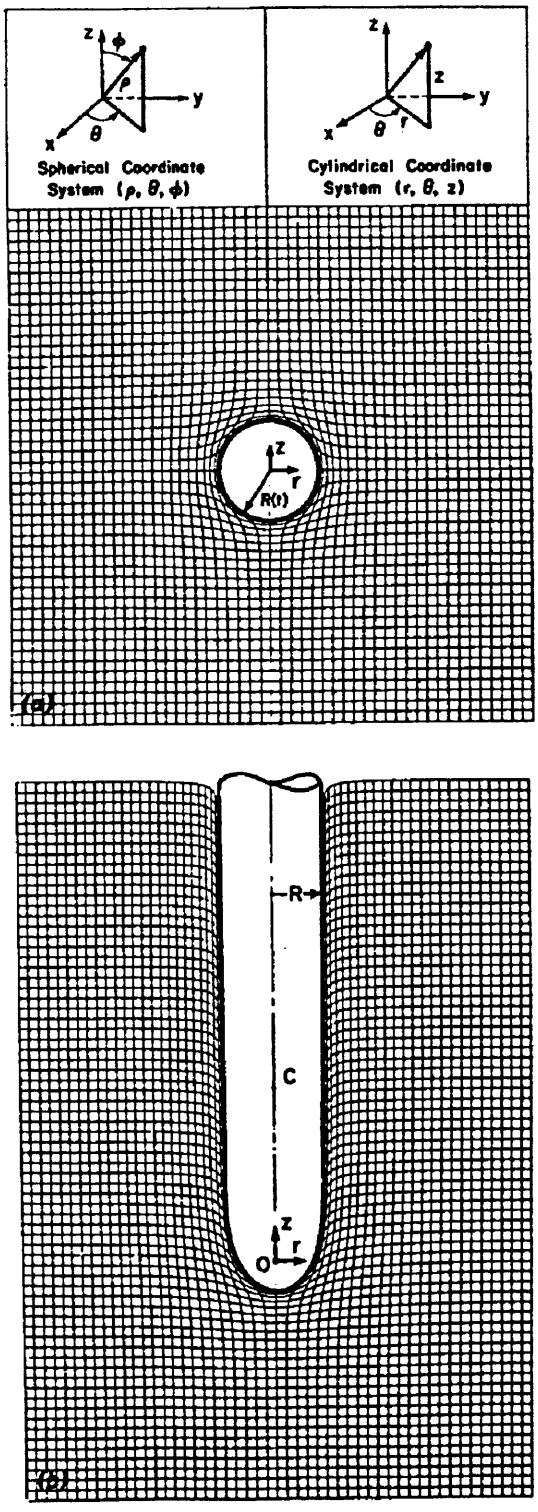

Figure 2.8: Deformation of square grid in saturated clays: (a) Spherical Cavity Expansion; (b) Simple Pile Solution (Baligh, 1985)

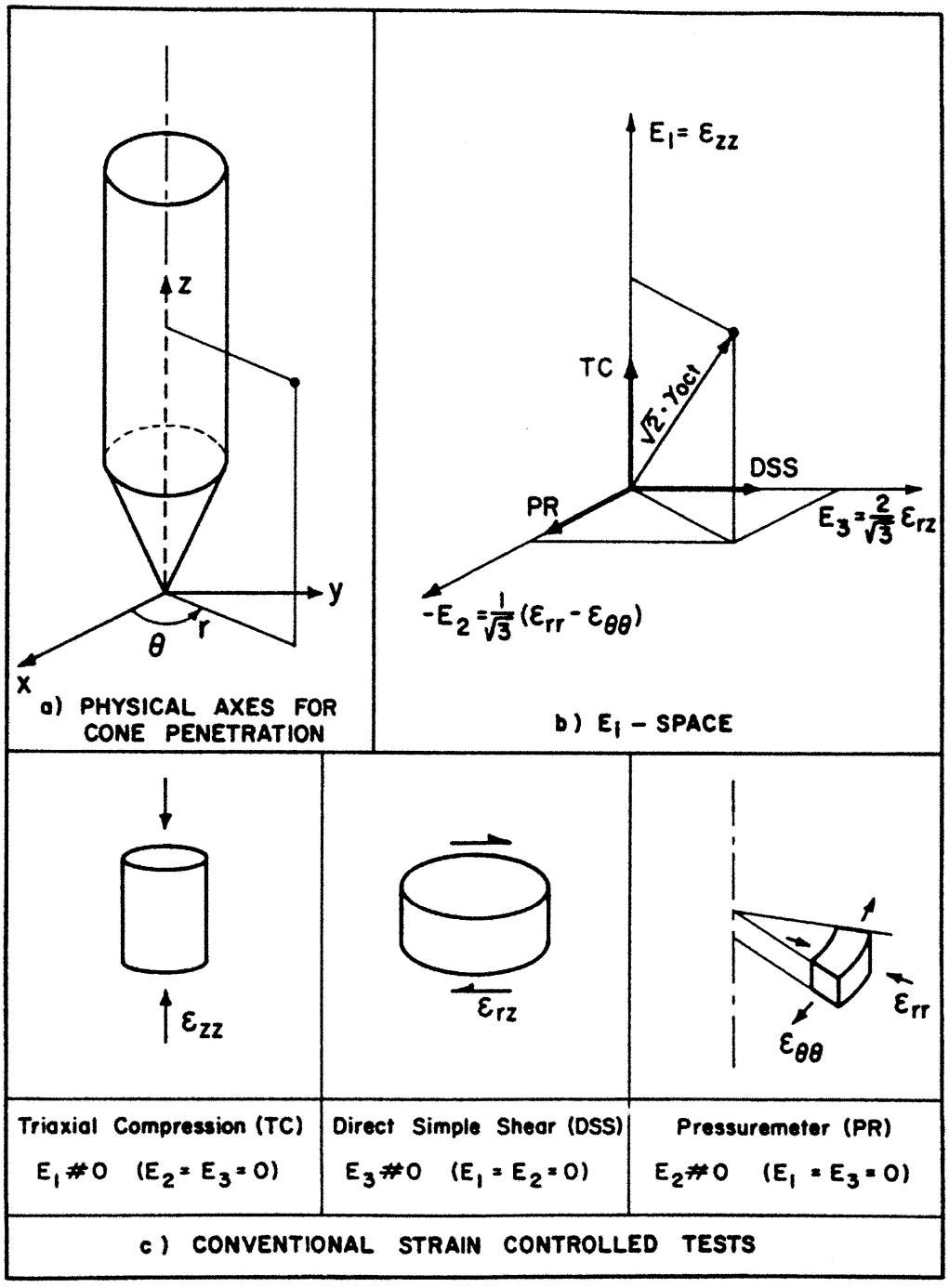

Figure 2.9: Strain representation on E_i-space (Levadoux, 1980)

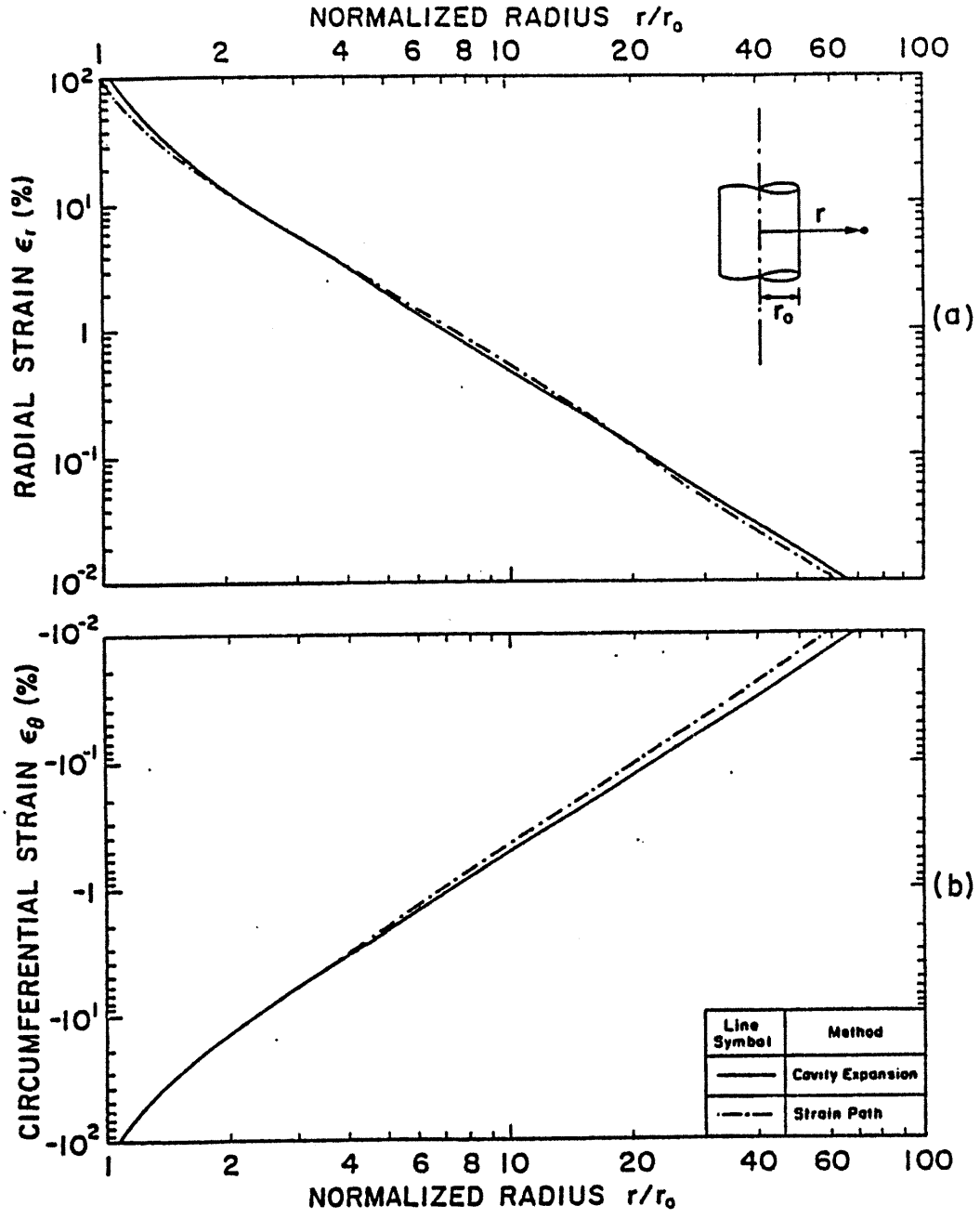

Figure 2.10: Distribution of (a) radial; (b) circumferential strains far behind the pile tip (Kavvadas,1982)

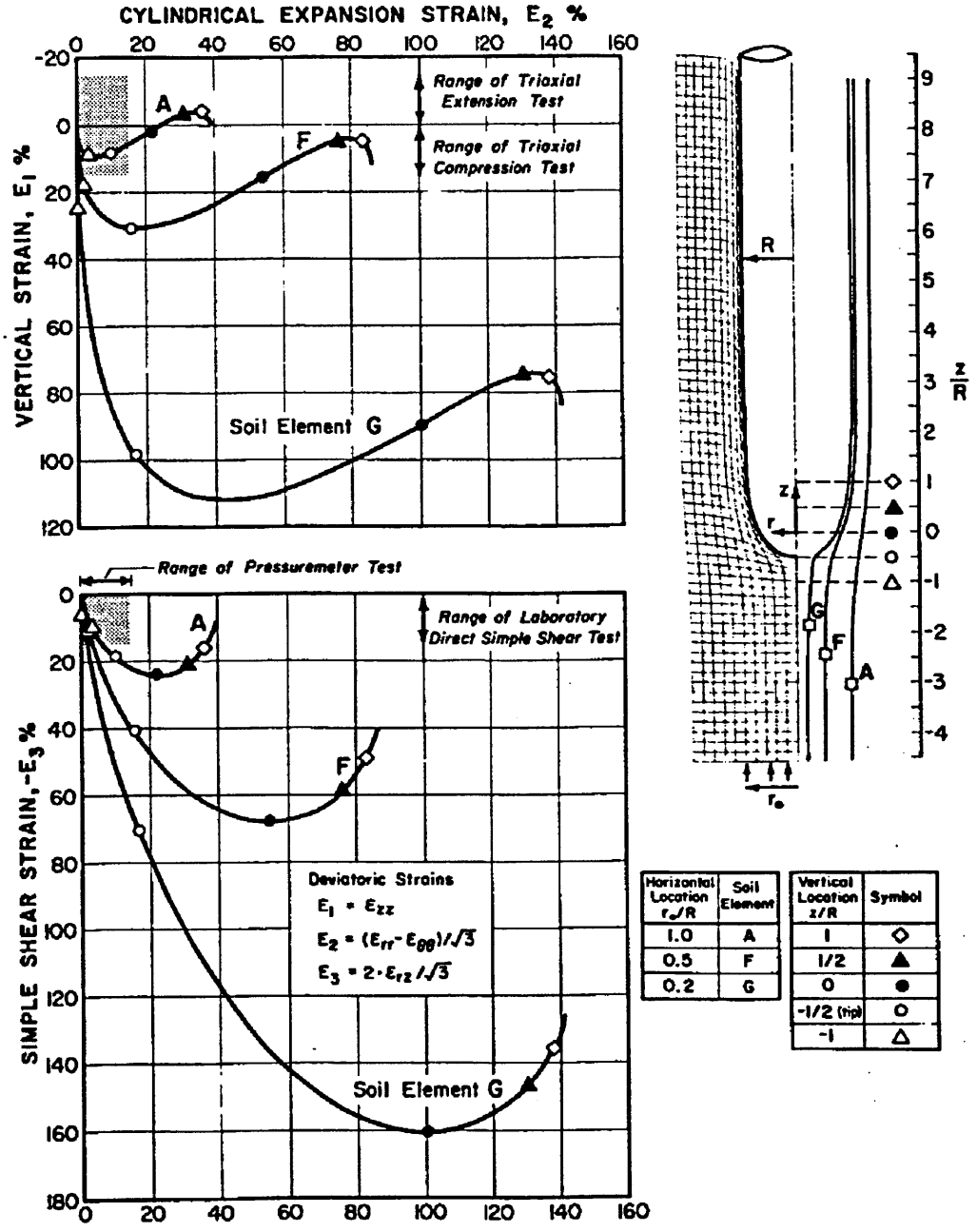

Horizontal Location r_o/R	Soil Element
1.0	A
0.5	F
0.2	G

Vertical Location z/R	Symbol
1	◇
1/2	▲
0	●
-1/2 (tip)	○
-1	△

Figure 2.11: Deviatoric strain paths during Simple Pile penetration (Baligh, 1985)

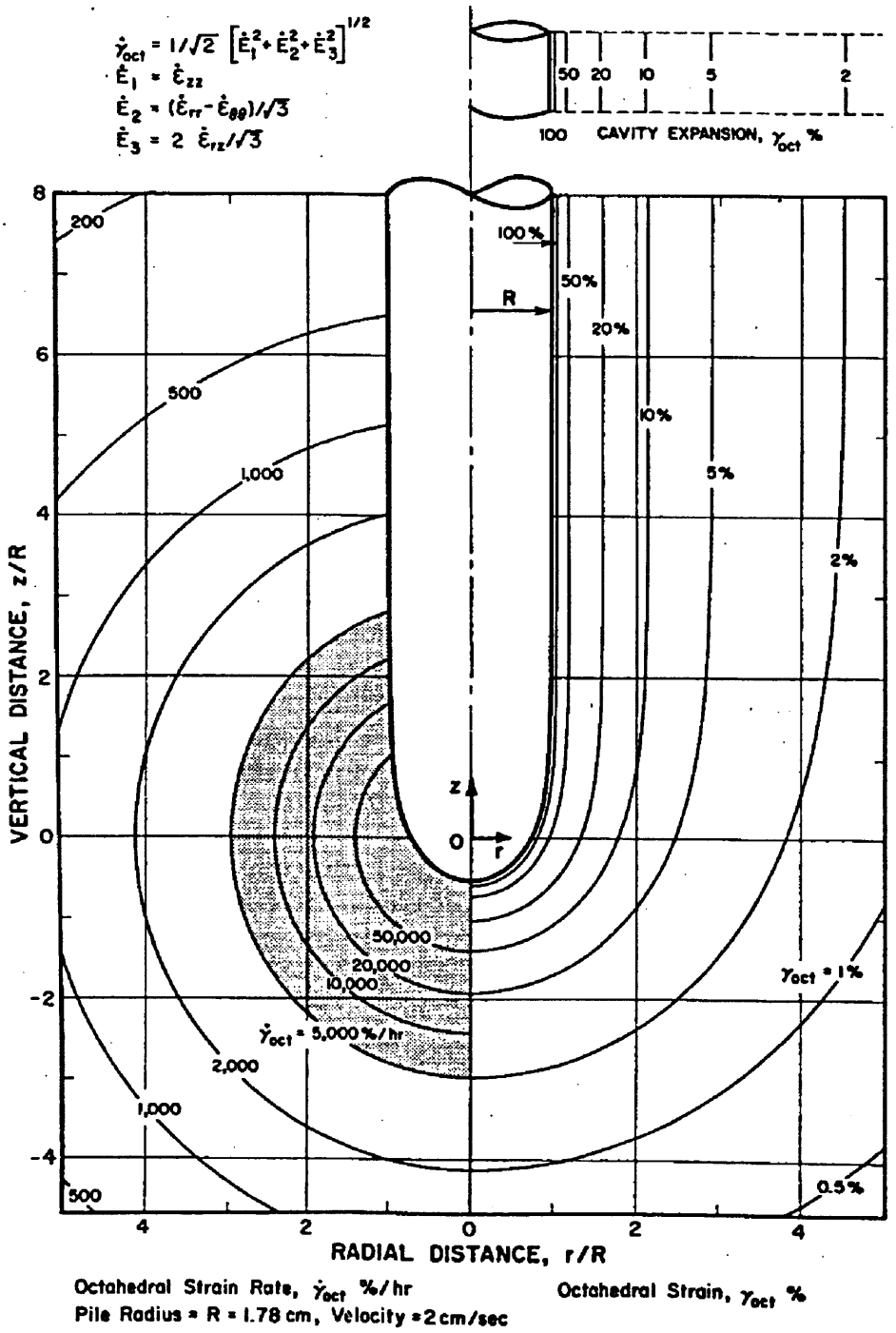

Figure 2.12: Octahedral shear strain and shear strain rate contours during Simple Pile penetration (Baligh, 1985)

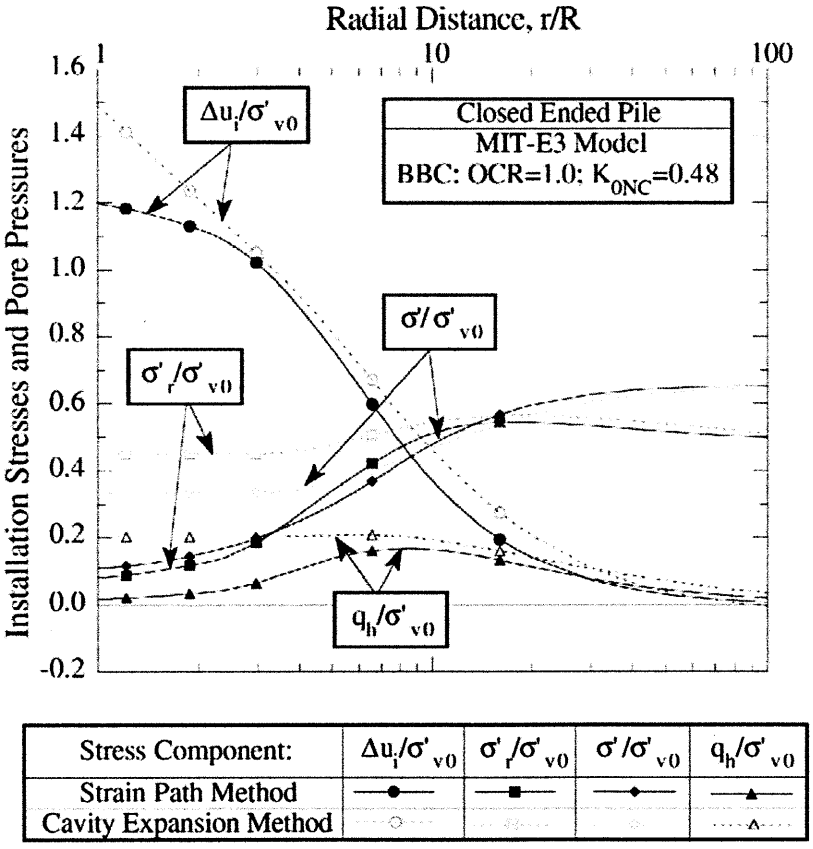

Figure 2.13: Strain path predictions of installation stresses in K_0-normally consolidated BBC (Whittle, 1993)

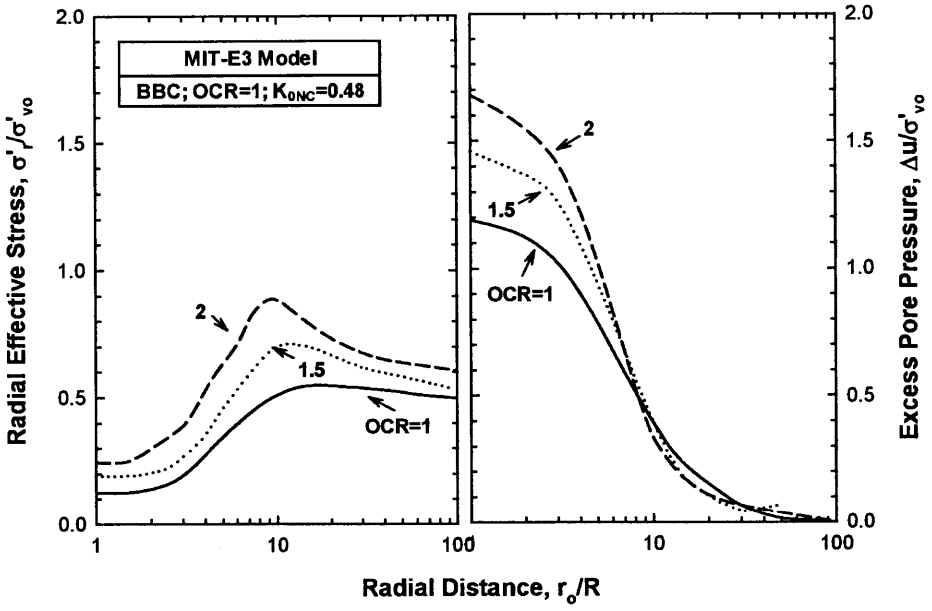

Figure 2.14: Strain path predictions of installation stresses & pore pressures for OCR=1; 1.5; and 2 (Sutabutr, 1999)

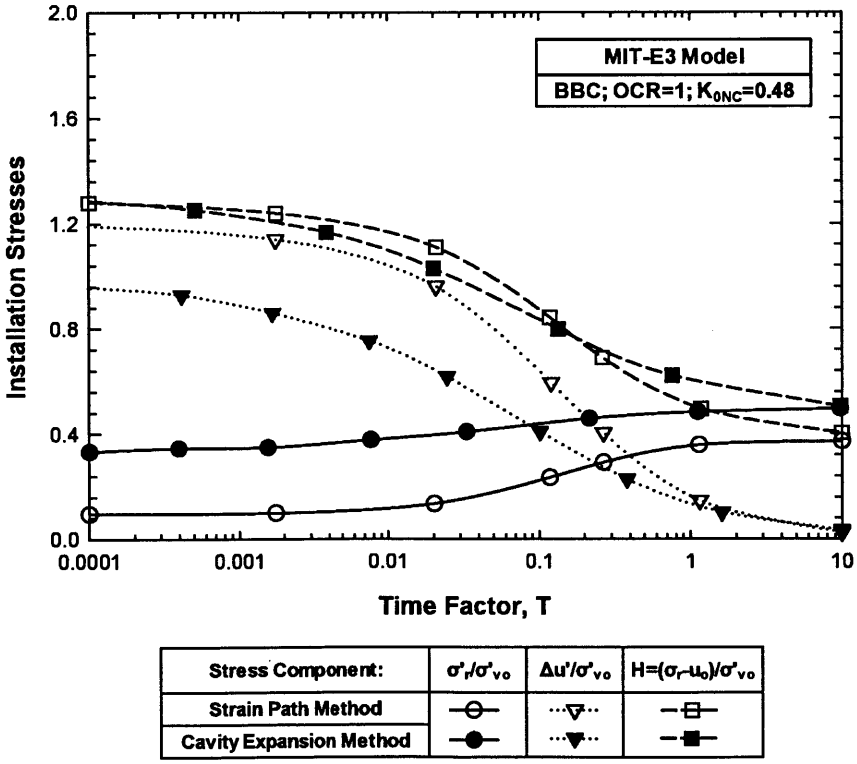

Figure 2.15: Typical predictions of consolidation at the pile shaft in K_0-normally consolidated BBC (Whittle, 1993)

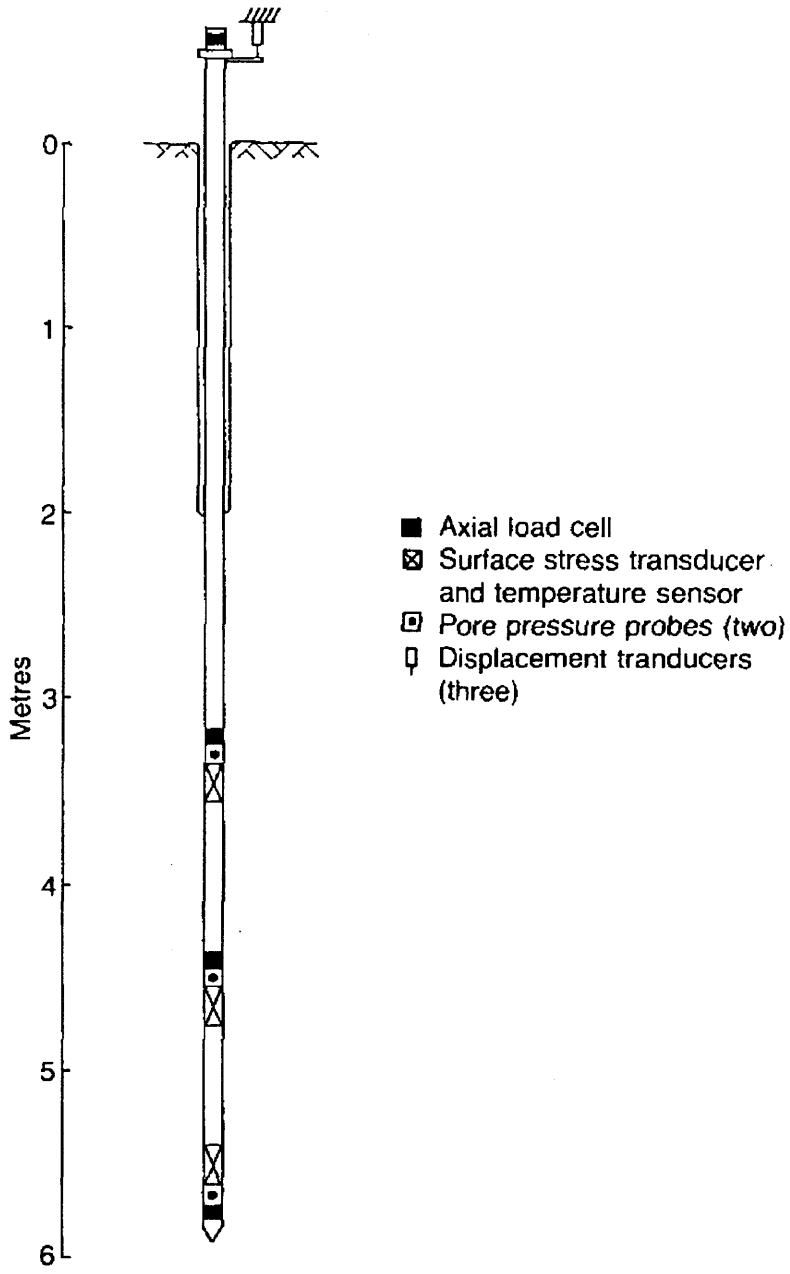

Figure 2.16: Imperial College instrumented pile

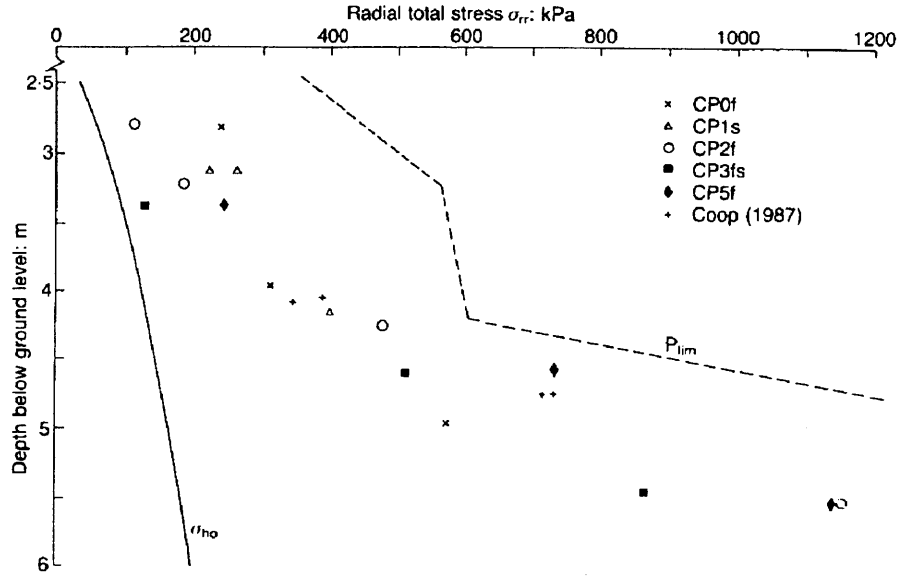

Figure 2.17: Radial total stress measurements at the end of pile installation (Bond & Jardine, 1991; Coop, 1987)

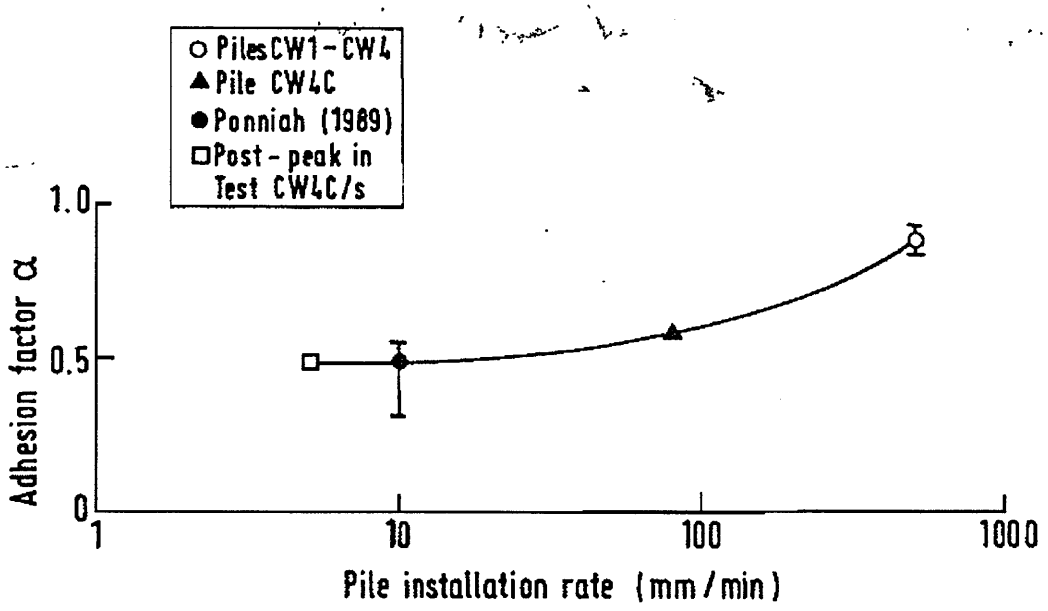

Figure 2.18: Rate dependence of installation shaft resistances (Lehane & Jardine, 1993; Ponniah, 1989)

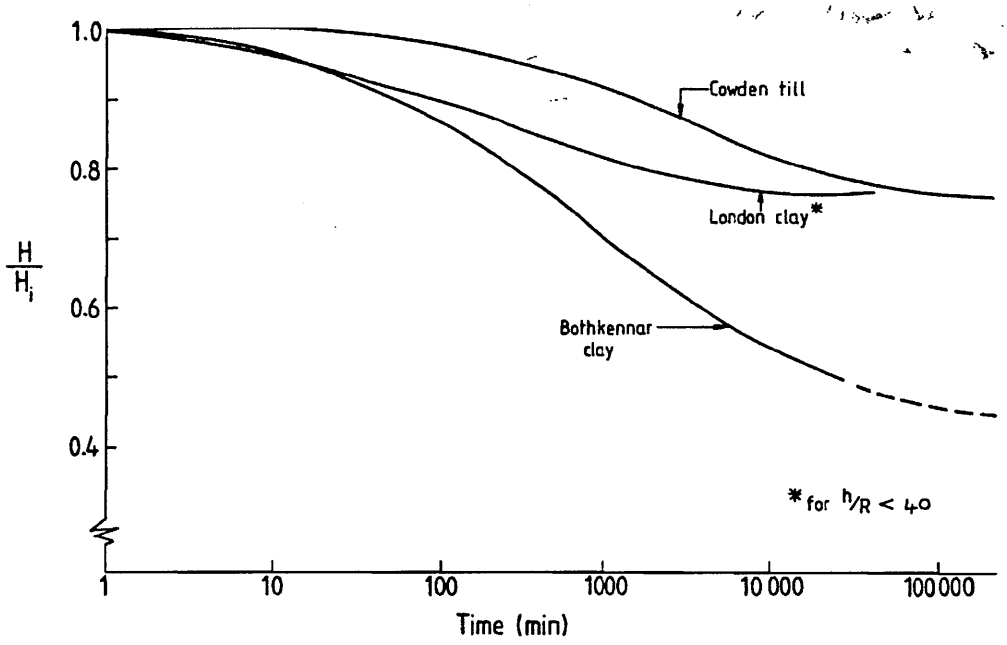

Figure 2.19: Relative reduction in radial total stresses during consolidation (Lehane & Jardine, 1993)

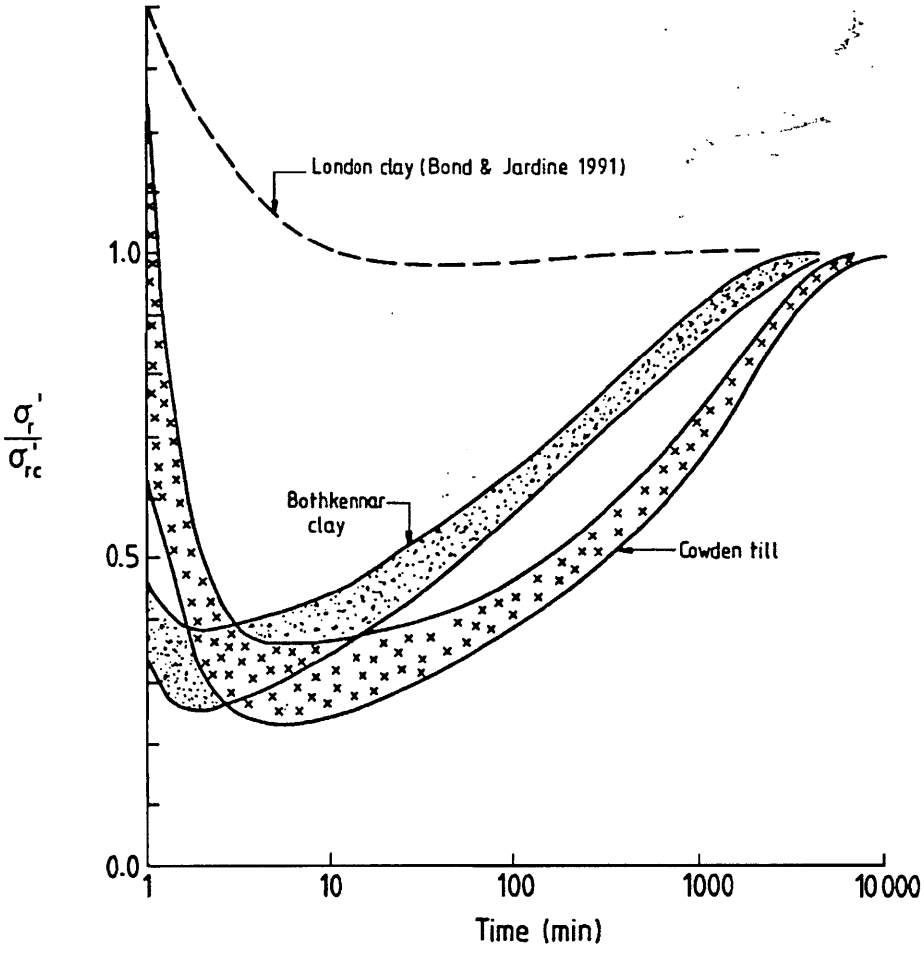

Figure 2.20: Normalized variations of σ'_r during consolidation (Lehane & Jardine, 1993)

3. STEADY STATE PILE INSTALLATION

3.1 INTRODUCTION

The increase in pile capacity with time after installation has been a widely discussed subject over the past 30 years. This phenomenon is usually associated with driven/displacement piles in low permeability soils, where high excess pore pressures are generated during installation.

Analytical predictions of pile installation have been pursued by a number of research groups including: i) Cambridge University, UK (Randolph, 1979; Randolph & Wroth, 1979); ii) University of Houston (O'Neill, 1985; Heydinger & O'Neill,1986); and iii) Massachusetts Institute of Technology (Baligh, 1985; Levadoux, 1980; Kavvadas, 1982; Whittle, 1987; Azzouz et al., 1990).

The analytical methods attempt to simulate the changes of soil stresses and properties around the pile shaft during the different stages in the life of the pile. The extensive research at MIT has produced a series of analytical tools for predicting the performance of friction piles in clays. The analytical tools include: i) Strain Path Method (SPM; Baligh, 1985) for modeling penetration behavior, and ii) a series of effective stress soil models for describing non-linear elasto-plastic response of anisotropic clays, namely MIT-E3 (Whittle, 1987) and MIT-S1 (Pestana, 1994).

The primary objective of this chapter is to combine the MIT-S1 model with the Strain Path Method to predict the effective stresses in the overconsolidated clays during steady

undrained pile installation (Stage 1). These values represent the initial conditions for the consolidation (Stage 2) and thus, they are essential in the rational interpretation of the consolidation that takes place after pile penetration. Subsequently, this chapter endeavors to identify the critical parameters affecting the installation stresses by investigating: i) the effect of method of analysis; ii) the effect of soil model; and iii) the effect of stress history.

3.2 SOIL MODEL AND METHOD OF ANALYSIS

The key step of both analytical frameworks described in *Section 2.3* (i.e. Cavity Expansion Methods, CEM; Strain Path Method, SPM) is that the soil velocities are estimated without reference to the properties of the soil and rely solely on the method of analysis used. This "decoupling" drastically simplifies the problem of modeling pile installation.

Another key decision is choosing the constitutive model to describe the soil behavior. This section reports briefly the soil models used to study pile penetration, along with the analytical procedures used to acquire the strains associated with each analytical framework.

3.2.1 Soil Model

Two constitutive soil models are used to outline the behavior of Boston Blue Clay (BBC). These models are the following:

1. MIT-E3

2. MIT-S1

For the sake of comparison, this section evaluates each soil model by indicating its significant features but its limitations as well.

3.2.1.1. MIT-E3

The MIT-E3 model (Whittle, 1987) was developed over the period 1984-1987 to describe the anisotropic behavior of normally and lightly overcnsolidated clays. It has been used successfully by Aubeny (1992) to predict the performance of piles installed in clays with OCR's up to four (OCR≤4). The model incorporates several important features of soil behavior, including anisotropic hardening, undrained brittleness at low OCR's, small strain (i.e. pre-yield) non-linearity in undrained shear and irrecoverable straining pre-yielding.

Certain features of the individual components of MIT-E3 are worth noting:

- The "perfectly hysteretic" model describes a closed (symmetric) hysteresis loop (such as A-B-A in *Figure 3.1a*). It assumes that the soil is isotropic and its volumetric and shear behavior are uncoupled; and it controls the soil's non-linearity at small strains.
- Bounding surface plasticity alters the unload/re-load path A-B-A by introducing irrecoverable strains (Δ^p) as the stress state approaches the virgin consolidation line (VCL). The clay's behavior is therefore described by the loop A-B-C (*Figure 3.1b*). In this way, every loading cycle produces some plastic straining.

Like all soil models, MIT-E3 suffers from a number of limitations, the principal ones being:

- It over-predicts the maximum stress obliquity in triaxial compression tests for overconsolidated clays. Predictions are less reliable for OCR≥4.
- It tends to underestimate the undrained shear strength in triaxial shear modes.
- The model was designed for rate-independent soils and hence takes no account of rate effects, drained creep, etc.

Table 3.1 summarizes the input parameters used by the MIT-E3 to model the behavior of the behavior of K_0-consolidated Boston Blue Clay (BBC) together with their physical significance and proposed laboratory tests from which these properties can be determined.

3.2.1.2. MIT-S1

Pestana (1994) developed the MIT-S1 model using a unified work capable of describing the behavior of sands, silts and clays. This new model retained the aforementioned basic components of its predecessor (MIT-E3; Whittle, 1987) but in the meantime improved three (3) previously reported limitations of MIT-E3 model (Whittle & Kavvadas, 1994):

1. The stress obliquity is well described, especially at high OCR through the use of one of the input parameters, φ'_m.
2. The model assumes that the yield behavior of K_0-consolidated soils becomes more isotropic with increasing overconsolidation, while MIT-E3 implicitly generates large anisotropy at high OCR.
3. The model simulates the measured tendency of the soil to dilate (negative induced pore pressures) when sheared to large strains in extension tests.

In its most general form, the MIT-S1 uses sixteen (16) input parameters, while only thirteen (13) of these are used for clays. *Table 3.2* summarizes the input parameters used by MIT-S1, together with the laboratory tests from which they can be determined, and gives the specific values to describe the behavior of K_0-consolidated Boston Blue Clay (Pestana, 1994).

Extensive comparisons with measured data from undrained shear tests performed in different modes of shearing and for high overconsolidation ratios (OCR$\leq$32) show that the model: i) gives excellent predictions of maximum shear stress conditions and accurately describes the non-linear shear stress-strain behavior; ii) accurately describes the anisotropic shear stress-strain-strength conditions for different radial consolidation stress histories; and iii) gives more realistic description of mobilized friction angles, especially at large OCR's.

Figures 3.2, 3.3 and 3.4 (Pestana, 1994) compare the computed and measured shear stress-strain behavior for K_0-consolidated BBC in the three modes of shearing which occur during pile installation (see *Figure 2.9*).

Figure 3.2 compares model predictions with measured shear stress-strain behavior of undrained triaxial compression (CK_0UC) and extension (CK_0UE) for K_0-consolidated samples. The MIT-S1 model predicts that the stress-strain behavior is non-linear over the full range of measured strains (no 'distinct' yielding is observed) for both normally and overconsolidated samples. The model gives excellent predictions of the shear-strain-strength behavior for OCR=2,4 and 8 for the database by Sheahan (1991). On the other hand, the observed behavior of the BBC tested by Fayad (1986) for the same nominal OCR's shows a stiffer response at all strain levels with significantly higher ($\simeq$20%)

undrained shear strength especially in the extension tests. The data of Fayad (1986) may be affected by thixotropic properties (strength and stiffness increases with storage time), while the data presented by Sheahan (1991) are considered the most reliable tests performed in resedimented BBC to date.

Figure 3.3 compares model predictions with measured shear stress-strain behavior for undrained Direct Simple Shear tests (CK_0UDSS) on recent resedimented BBC for nominal OCR's=1, 2, 4, 8, 15 and 32 (Ahmed, 1991; Ortega, 1992; Cauble, 1993). At OCR=1, model predictions are in good agreement with the measured stress-strain behavior. At OCR=2 and 4, the model gives excellent predictions of undrained shear strength and maximum stress obliquities (i.e. τ/σ'_v) mobilized in horizontal planes, but significantly over predicts the stiffness for $\gamma<2\%$ for OCR=4. For OCR's 8 and 15 model gives good predictions of undrained shear strength at large strains ($\gamma=10\%$) , but overestimates significantly the shear stiffness throughout the test. Predictions at OCR=32 greatly overestimate the measured stiffness and strength of the clay. *Figure 3.3b* shows that, in general, the model gives good predictions of secant stiffness at low OCR's (<4) at strains typically larger than 1-2%, while significantly overpredicting the stiffness at higher OCR's (≥4) at all levels of strain.

The pressuremeter shear mode (E_2, *Figure 2.9*) is especially important for estimating the effects of pile installation and can be simulated in laboratory element tests using more sophisticated equipment such as the Directional Shear Cell (DSC). *Figure 3.4a* compares the predicted and measured shear stress-strain behavior of K_0-normally consolidated BBC. The DSC measurements at $\delta_{inc}=0^o$ and 90^o are in reasonable agreement with the plane strain data reported by Ladd et al. (1971) and are well described by the MIT-S1

model. The model tends to underpredict the strength and stiffness in tests with Principal stress rotations (i.e. δ_{inc}=45°, 60°), but gives excellent predictions of material response, strength and stiffness for δ_{inc}=75°, as reported by Seah (1990). Overall, the MIT-S1 model gives a good description of the stress-strain (*Figure 3.4b*) for all directions of shearing at strain levels, $\gamma \geq 0.1\%$, but overestimates the small strain stiffness for $\gamma \leq 0.1\%$ for $\delta_{inc} < 60°$.

Taking into consideration the previously mentioned improvements of MIT-S1 over MIT-E3, especially at high OCR, makes MIT-S1 a powerful tool in predicting the behavior of pile penetration in highly overconsolidated clays. The ultimate goal of this work is to describe typical predictions of pile shaft performance using Strain Path analyses in conjunction with MIT-S1 soil model for values of OCR≤16.

3.2.2 Method of Analysis

The two methods described thoroughly in *Section 2.3.1 and 2.3.2*, are utilized to analyze the steady state pile installation. These methods are the following:

1. The cylindrical Cavity Expansion Method (CEM)
2. The Strain Path Method (SPM)

The assumptions used in both methods impose kinematic constraints such that the strains in the soil around the pile can be estimated without considering the stress-strain behavior of the soil. The following sections explain in detail the numerical schemes used to compute the predicted stress changes in soil during pile installation according to each one of the aforementioned methods.

3.2.2.1. Numerical scheme used for CEM

During undrained cavity expansion, all soil elements follow the same (radial) strain path, but each corresponds to a different point along this path depending on its distance r_o/R from the center-line of the cavity. Thus, all soil elements trace the same stress-strain curve (corresponding to the undrained cylindrical cavity expansion mode of deformation) and, their effective stress can be directly computed from the level of strain associated with each soil element (via *Equations 2.8 and 2.9* or *Equations 2.10 and2.11*).

Forty five (45) intervals (i.e. 46 nodal points) are used with interval length gradually decreasing towards the cavity to provide better resolution in the zone of high strain gradients near the cavity wall. The locations of the nodal points are shown in *Table 3.3*.

Solutions are obtained by means of a computer program modified by the author to incorporate MIT-S1 as the constitutive soil model. This program calculates the effective stresses and excess pore pressures during the undrained expansion of cylindrical cavity. *Appendix A* presents a user's manual and a complete listing of this program.

3.2.2.2. Numerical scheme used for SPM

The Strain Path Method (SPM) predictions are determined by means of the procedure explicated in *Section 2.3.2* using the Simple Pile Solution. Analyses are performed using 90 stream-lines to cover the soil mass for $r/R \rightarrow 111.4$. Strain paths are computed over a fixed vertical interval relative to the pile tip, $-190 \leq z/R \leq 200$.

Each stream-line consists of 1332 nodal points. The radial coordinates of the first point (i.e. in front of the pile tip) on each stream-line are shown in *Table 3.4*.

Solutions are obtained by means of a computer program modified by the author to incorporate MIT-S1 as the constitutive soil model. This program calculates the effective stresses and the remaining state variables across a cylindrical pile using the Strain Path Method. *Appendix A* presents a user's manual and a complete listing of this program.

3.3 INSTALLATION EFFECTIVE STRESSES

Pile installation in clays is modeled as the undrained, steady penetration of a rigid axi-symmetric indenter. This section attempts to identify the parameters affecting the pile set-up processes for friction piles in normally to highly overconsolidated clays. The predictions consider the following combination of parameters:

1. Two methods of analysis, cylindrical Cavity Expansion Method (CEM) and Strain Path Method (SPM)
2. Two constitutive soil models, MIT-E3 and MIT-S1 for the reference soil (K_0[10]-consolidated Boston Blue Clay; BBC)
3. Five overconsolidation ratios, OCR=1.0, 2.0, 4.0, 8.0 and 16.0

The strain fields around the indenter are estimated using the assumptions discussed extensively in *Section 2.3.4.1*.

3.3.1 Effect of method of analysis

Installation effective stresses are presented in the form of normalized plots of σ'_r/σ'_{vo}, σ'/σ'_{vo}, $(\sigma'_r-\sigma'_\theta)/2\sigma'_{vo}$ versus the normalized radial distance from the pile shaft, r_o/R. Normalization using the vertical effective stress assumes that the soil exhibits normalized

[10] in situ earth pressure of undisturbed soil; K_0=0.49

stress-strain-strength behavior, and enables comparison with measurements at any depth below the mudline.

Figures 3.5, 3.6 and 3.7 present Strain Path (SPM) and cylindrical Cavity Expansion (CEM) predictions of installation stresses far behind the tip of a pile[11] in K_0-normally consolidated BBC using the MIT-S1 soil model for five (5) overconsolidation ratios, OCR=1.0, 2.0, 4.0, 8.0 and 16. The following remarks can be made:

- For every overconsolidation ratio (*Figures 3.5-3.7*), the method of analysis affects significantly the magnitude and distribution of stresses in the vicinity of the pile wall, $r_o/R \leq 10$.
- For normally or lightly overconsolidated clay (OCR≤4), undrained shearing generates positive shear induced pore pressures and a corresponding net reduction in the mean effective stress, σ'/σ'_{vo}, close to the pile shaft. Differences in the magnitude of σ'/σ'_{vo} for SPM and CEM ($r_o/R \leq 10$; *Figure 3.5 and 3.6a*) reflect how the anisotropic and strain softening properties described by the MIT-S1 model are affected by differences in strain histories.
- The effects of the analysis used to model installation can be seen more clearly in predictions of the radial effective stress, σ'_r/σ'_{vo}, and cavity shear stress, $(\sigma'_r - \sigma'_\theta)/2\sigma'_{vo}$. The SPM predicts very low radial effective stresses and cavity shear stresses acting at the pile shaft for all OCR's. This means that the radial effective stress is similar in magnitude to the mean effective stress ($\sigma'_r/\sigma'_{vo} \simeq \sigma'/\sigma'_{vo}$) for $r_o/R \leq 10$. In contrast, CEM analyses give higher values of radial effective stress

[11] at an elevation z=20R above the tip

and predict that $\sigma'_r/\sigma'_{vo} \geq \sigma'/\sigma'_{vo}$ over a radial zone of $r_o/R \leq 10$ for OCR=1 (*Figure 3.5a*) and escalating to $r_o/R \leq 100$ for OCR=16 (*Figure 3.7*).

3.3.2 Effect of soil model

According to Pestana (1994), the behavior of highly overconsolidated clays (with OCR≤32) measured in laboratory tests can be simulated better using the MIT-S1 rather than the MIT-E3 soil model. Thus, more realistic predictions are anticipated using the MIT-S1 to model the behavior of K_0-consolidated BBC.

Figures 3.8, 3.9 and 3.10 show contour plots of the effective stresses around the Simple Pile using the SPM for OCR's=1, 2 and 4 according to MIT-E3 & MIT-S1. The following effects of soil models can be observed:

- Distributions of radial effective stress, σ'_r/σ'_{vo}, predicted by MIT-S1 for OCR=1 are similar to results for the MIT-E3 model, since distinct differences between these two models occur especially with increasing overconsolidation, as mentioned before. At OCR's=2 and 4 the radial effective stress contours predicted by MIT-S1 are qualitatively similar to MIT-E3 model, with higher values of σ'_r/σ'_{vo} for MIT-E3 acting on the tip of the pile.
- The pattern of mean effective stress, σ'/σ'_{vo}, is similar for both MIT-S1 & MIT-E3 soil models. According to this pattern, σ'/σ'_{vo} decreases from a maximum value at the tip of the pile, to a minimum value on the pile shaft. Hence, the maximum shear-induced pore pressures are along the pile shaft. These results reflect the anisotropic and strain softening behavior of both soil models.

- At a given OCR, the MIT-S1 model predicts similar values of cavity shear stress, $(\sigma'_r-\sigma'_\theta)/2\sigma'_{vo}$, acting on the penetrometer to MIT-E3. Differences in magnitude of $(\sigma'_r-\sigma'_\theta)/2\sigma'_{vo}$ can be attributed to the different anisotropic behavior of the two soil models at high OCR.

3.3.3 Effect of stress history

Figures 3.11 and 3.12 show predictions of the installation stresses around the Simple Pile for the base case analysis (MIT-S1; K_0-consolidated BBC) at OCR's=1, 2, 4, 8 and 16. The results present the following:

- The radial effective stress, σ'_r/σ'_{vo}, reaches a maximum value around the same radial distance (r/R=8) for every OCR apart from low OCR's (OCR=1 and 2), where the maximum value is achieved at far locations around the shaft (r/R=100). It should also be noted that at the far field (r/R=100), the value of σ'_r/σ'_{vo} increases with OCR, since it is direct proportional to the earth pressure coefficient at rest K_0.
- Changes in mean effective stress (i.e. shear-induced pore pressure) are related to the critical state conditions described by the MIT-S1 model. The magnitude of σ'/σ'_{vo} increases substantially with OCR, but is approximately constant over a radial zone of $r_o/R \leq 4$ as the large strains produce critical state conditions. Similarly, contours fo cavity shear stress, $(\sigma'_r-\sigma'_\theta)/2\sigma'_{vo}$, are qualitatively similar for all OCR's.

Test Type	Parameter / Symbol	Physical Contribution / Meaning	Boston Blue Clay (BBC)
Hydrostatic or 1-D Compression (Triaxial, Oedometer or CRS apparatus)	e_o	Void ratio at reference stress on virgin consolidation line	1.12
	λ	Compressibility of virgin normally consolidated clay	0.184
	C	Non-linear volumetric swelling behavior	22.0
	n		1.60
	h	Irrecoverable plastic strain	0.2
K_0-oedometer or K_0-triaxial	K_0^{NC}	K_0 for virgin normally consolidated clay	0.48
	2G/K	Ratio of elastic shear to bulk modulus (Poisson's ratio for initial unload)	1.05
Undrained Triaxial Shear Tests: OCR=1; CK_0UC OCR=1; CK_0UE (OCR>1; CK_0UC optional)	φ'_{TC}	Critical state friction angles in triaxial compression and extension (large strain failure criterion)	33.4°
	φ'_{TE}		45.9°
	c	Undrained shear strength (geometry of bounding surface)	0.86
	S_t	Amount of post-peak strain softening in undrained triaxial compression	4.5
	w	Non-linearity at small strains in undrained shear	0.07
	γ	Shear pore pressure for OC clay	0.5
Resonant Column	κ_o	Small strain stiffness at load reversal	0.001
Drained Triaxial	Ψ_o	Rate of evolution of anisotropy (rotation of bounding surface)	100.0

Table 3.1: Input material properties used by the MIT-E3 model (Whittle, 1987)

Test Type	Parameter / Symbol	Physical Contribution / Meaning	Boston Blue Clay (BBC)
Hydrostatic or 1-D Compression (Triaxial, Oedometer or CRS apparatus)	ρ_c	Compressibility of normally consolidated (NC) clay	0.178
	D	Non-linear volumetric swelling behavior	0.04
	R		0.85
	h	Irrecoverable plastic strain	6.0
K_0-oedometer or K_0-triaxial	K_0^{NC}	K_0 for NC clay	0.49
	μ'_o	Poisson's ratio at stress reversal controlling $2G_{max}/K_{max}$	0.24
	ω	Non-linear Poisson's ratio; Stress path in 1-D unloading	1.0
Undrained Triaxial Shear Tests: OCR=1; CK_0UC OCR=1; CK_0UE (OCR>1; CK_0UC optional)	φ'_{cs}	Critical state friction angle in triaxial compression	33.5°
	φ'_m	Geometry of bounding surface. Stress path of undrained CK_0UTC/TE tests	46.0°
	m		0.80
	ω_s	Small strain non-linearity in shear	8
	ψ	Rate of evolution of anisotropy (rotation of bounding surface)	15
Shear wave velocity / Resonant Column	C_b	Small strain stiffness at load reversal	450

Table 3.2: Input material properties used by the MIT-S1 Model (Pestana, 1994)

Node	r_o/R	Node	r_o/R
1	1.00000	24	3.16219
2	1.00445	25	3.44810
3	1.00746	26	3.73622
4	1.02156	27	4.12302
5	1.04530	28	4.60968
6	1.07794	29	5.09893
7	1.11866	30	5.83621
8	1.16661	31	6.57637
9	1.22093	32	7.56626
10	1.28079	33	8.55850
11	1.34545	34	9.55236
12	1.41425	35	11.04522
13	1.48661	36	12.04144
14	1.56202	37	14.03550
15	1.72040	38	16.03103
16	1.88672	39	18.02755
17	1.97223	40	20.02477
18	2.10289	41	30.01638
19	2.23598	42	40.01217
20	2.41652	43	50.00963
21	2.59991	44	70.00669
22	2.78559	45	100.00440
23	2.97312	46	150.00000

Table 3.3: Radial coordinates used to model pile installation via the cylindrical Cavity Expansion Method (CEM)

Node	r_0/R	Node	r_0/R	Node	r_0/R
1	0.09000	31	3.46000	61	15.90000
2	0.11000	32	3.50000	62	16.00000
3	0.13000	33	3.54000	63	16.10000
4	0.19000	34	3.96000	64	18.90000
5	0.21000	35	4.00000	65	19.00000
6	0.23000	36	4.04000	66	19.10000
7	0.29000	37	4.46000	67	21.90000
8	0.31000	38	4.50000	68	22.00000
9	0.33000	39	4.54000	69	22.10000
10	0.39000	40	4.95000	70	24.90000
11	0.41000	41	5.00000	71	25.00000
12	0.43000	42	5.05000	72	25.10000
13	0.46000	43	5.95000	73	27.90000
14	0.50000	44	6.00000	74	28.00000
15	0.54000	45	6.05000	75	28.10000
16	0.96000	46	6.95000	76	30.80000
17	1.00000	47	7.00000	77	31.00000
18	1.04000	48	7.05000	78	31.20000
19	1.46000	49	7.95000	79	40.80000
20	1.50000	50	8.00000	80	41.00000
21	1.54000	51	8.05000	81	41.20000
22	1.96000	52	8.95000	82	50.60000
23	2.00000	53	9.00000	83	51.00000
24	2.04000	54	9.05000	84	51.40000
25	2.46000	55	9.90000	85	80.60000
26	2.50000	56	10.00000	86	81.00000
27	2.54000	57	10.10000	87	84.40000
28	2.96000	58	12.90000	88	110.60000
29	3.00000	59	13.00000	89	111.00000
30	3.04000	60	13.10000	90	111.40000

Table 3.4: Radial coordinates of the nodal points in front of the tip of the pile used to model pile installation via the Strain Path Method (SPM)

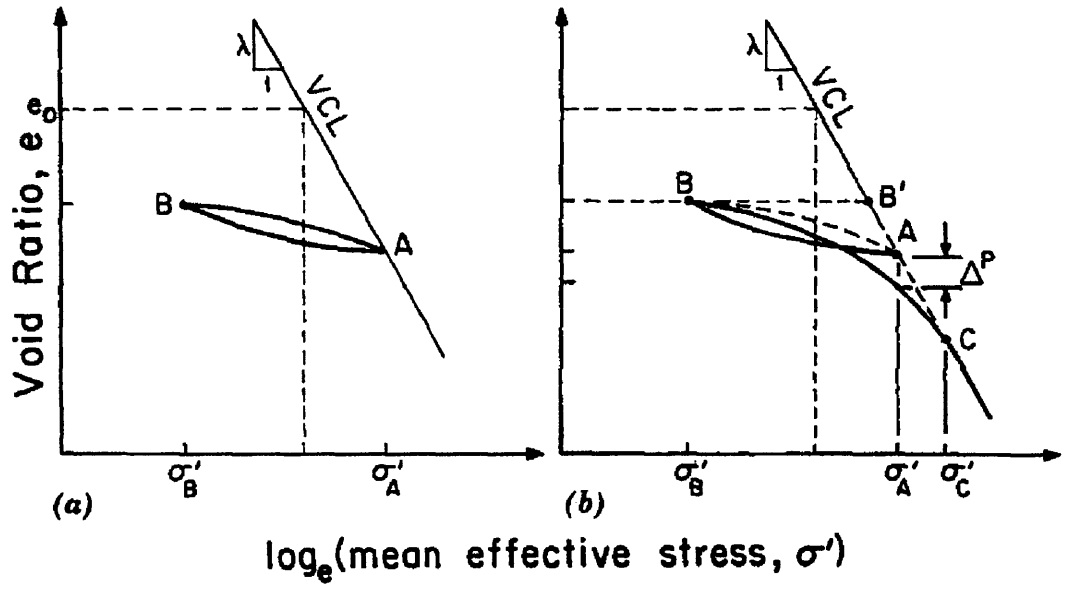

Figure 3.1: Conceptual model of unload-reload used by MIT-E3 for hydrostatic compression: (a) perfect hysteresis; (b) hysteresis and bounding surface plasticity

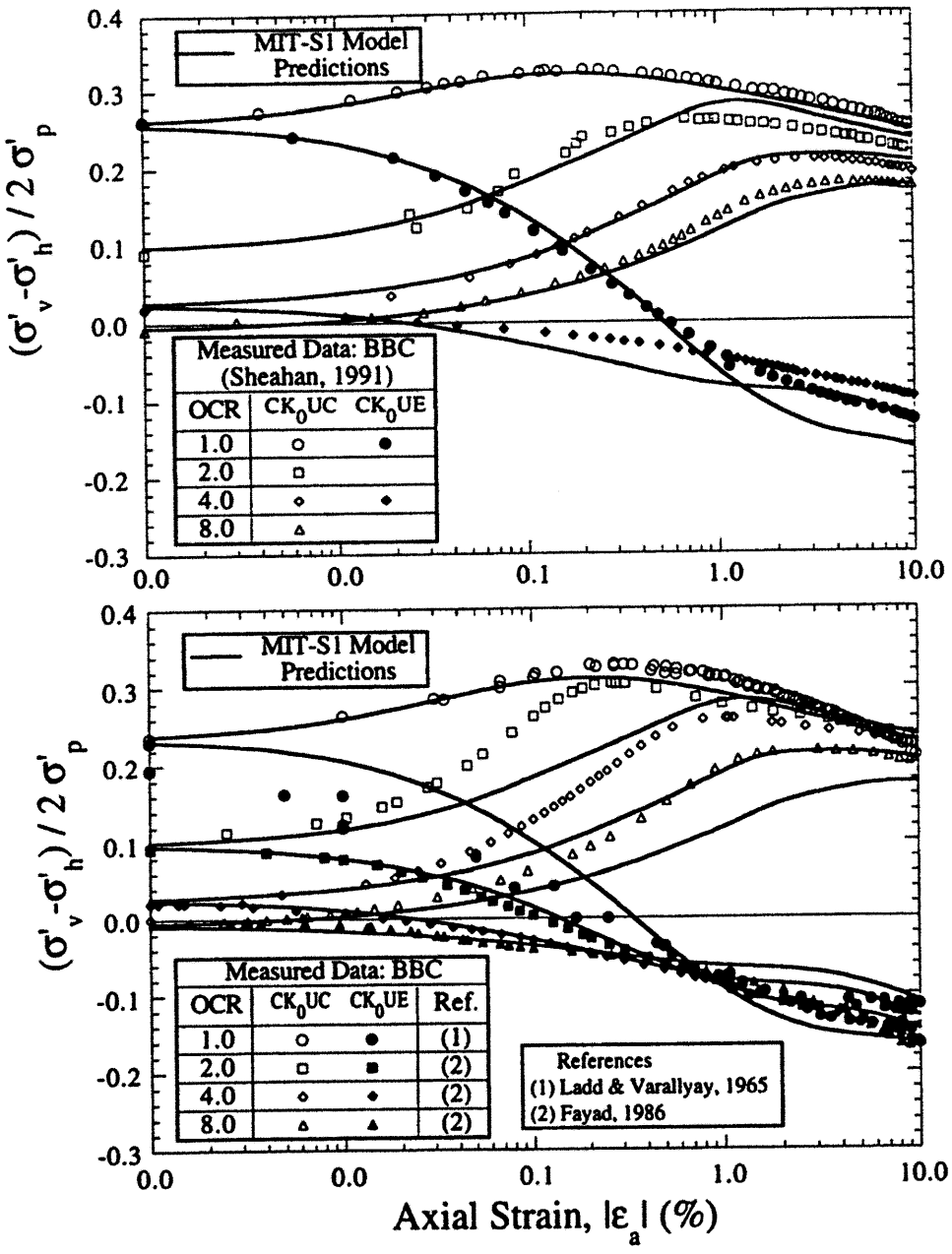

Figure 3.2: Comparison of MIT-S1 predictions and measured data for undrained triaxial compression (CK_0UC) and extension (CK_0UE) on K_0-consolidated Boston Blue Clay (Pestana, 1994)

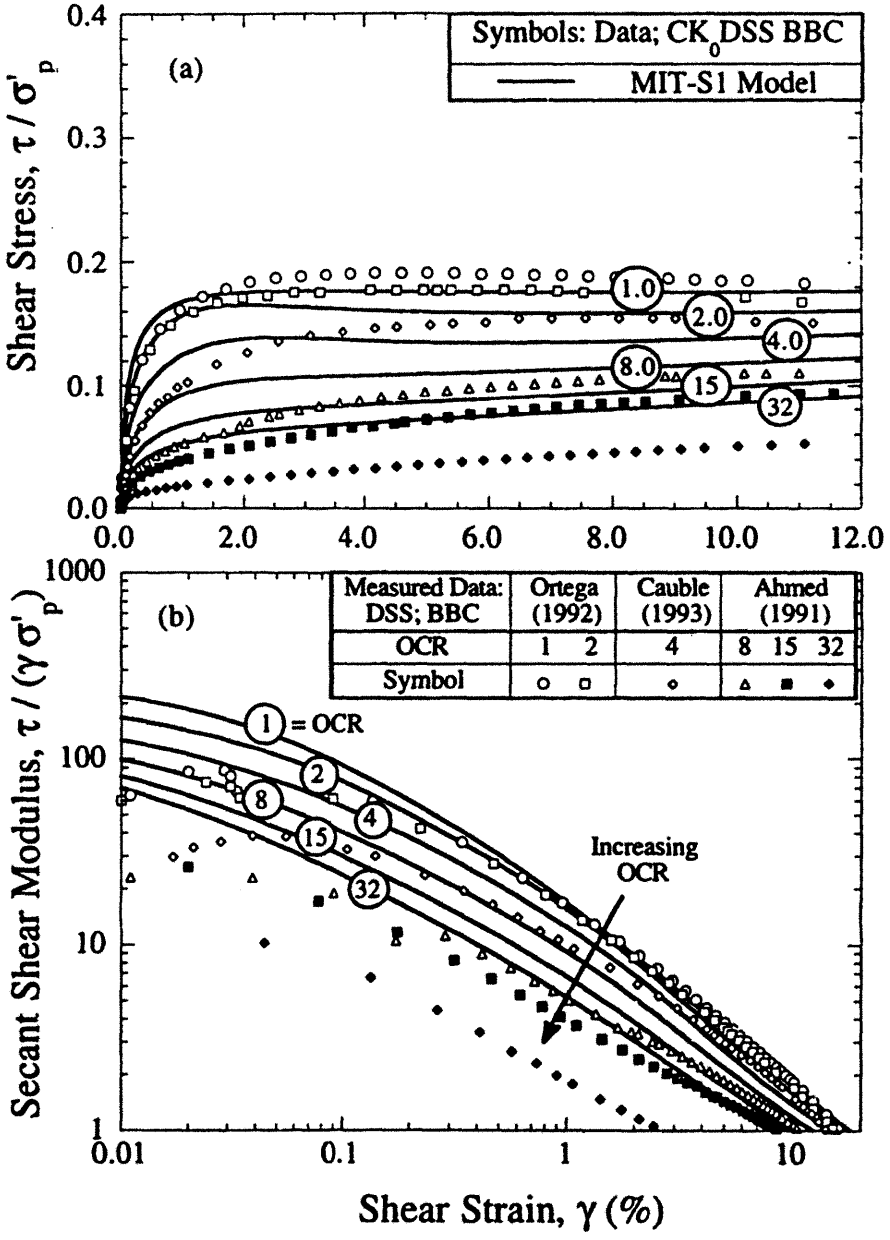

Figure 3.3: Comparison of MIT-S1 predictions and measured data for undrained Direct Simple Shear tests (CK_0UDSS) on K_0-consolidated Boston Blue Clay: (a) shear stress-strain response, (b) secant shear modulus (Pestana, 1994)

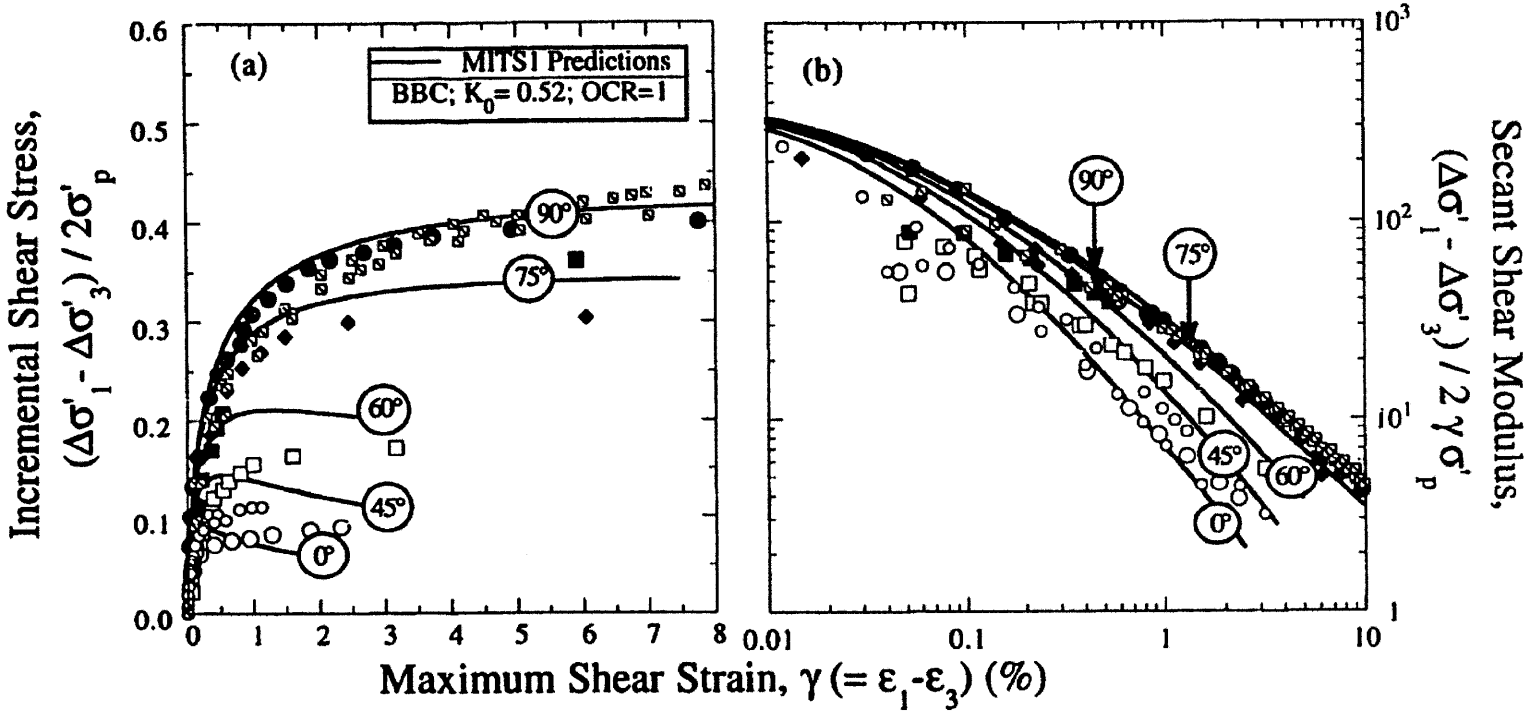

Measured Data:	DSC (Seah, 1990)	Plane Strain (Ladd et al. 1971)
δ_{inc} (°)	0 45 60 75 90	0 90
Symbol:	○ □ ◆ ■ ●	○ ▧

Figure 3.4: Comparison of MIT-S1 predictions and measured data for Directional Shear Cell (DSC) on K_0-consolidated Boston Blue Clay: (a) shear stress-strain response, (b) secant shear modulus (Pestana, 1994)

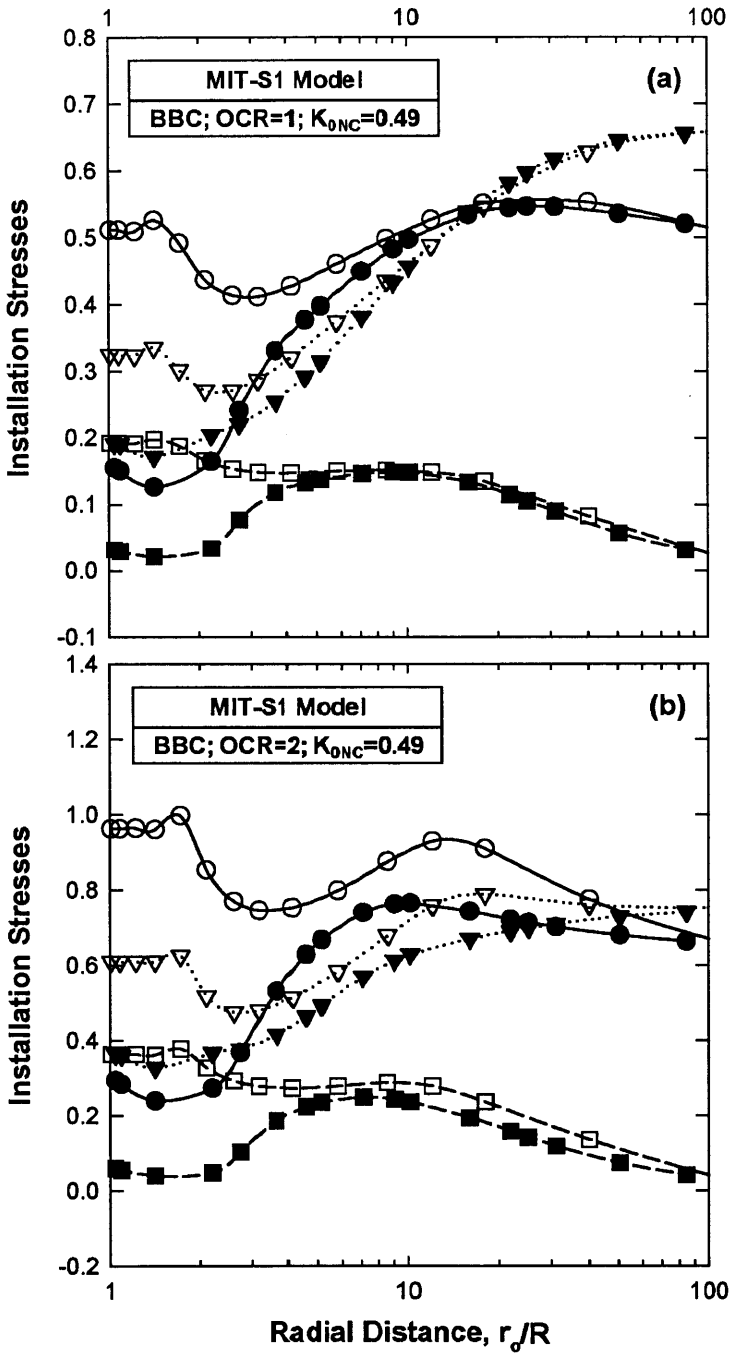

Figure 3.5: Effect of method of analysis on predictions of installation stresses for (a) OCR=1, (b) OCR=2

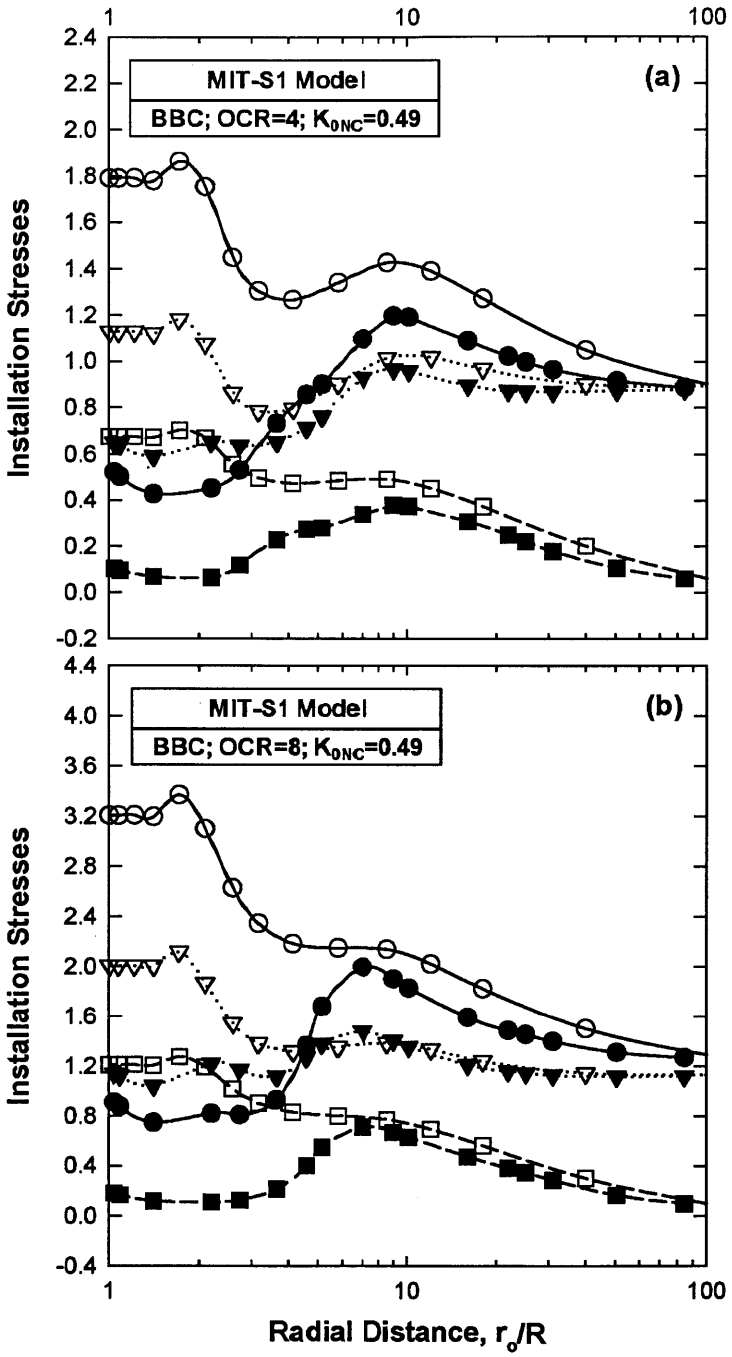

Figure 3.6: Effect of method of analysis on predictions of installation stresses for (a) OCR=4, (b) OCR=8

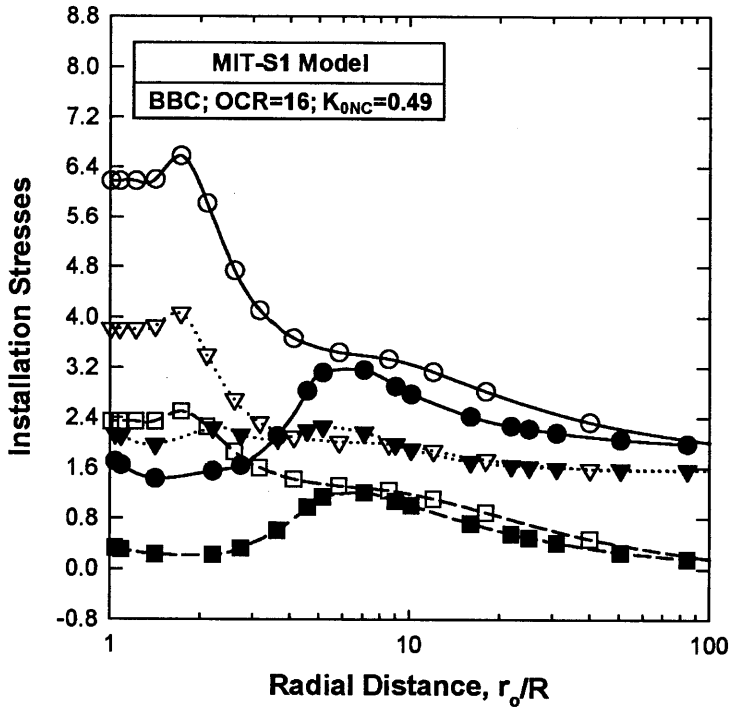

Figure 3.7: Effect of method of analysis on predictions of installation stresses for OCR=16

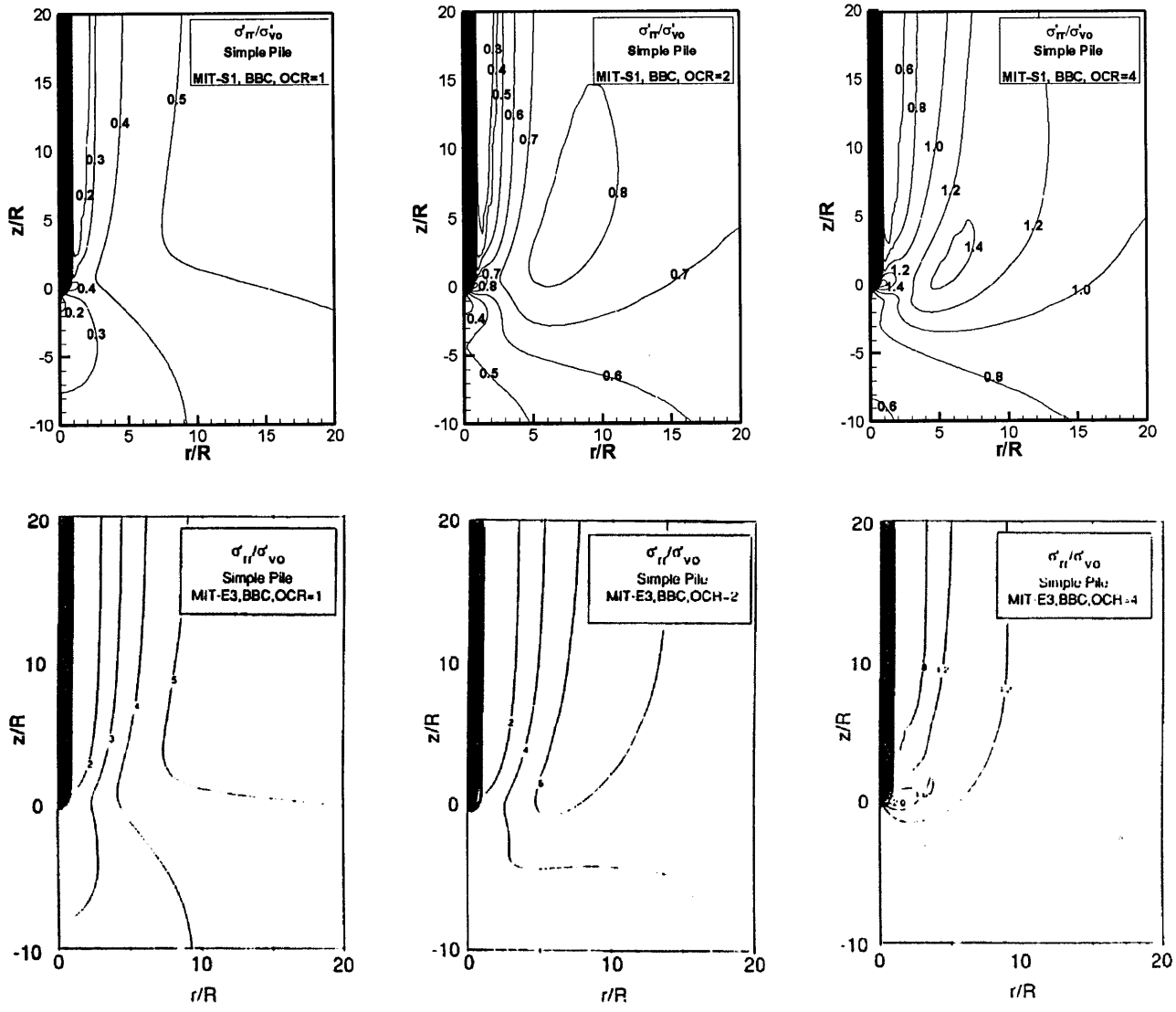

Figure 3.8: Effect of soil model on predictions of installation stresses, σ'_r/σ'_{vo}

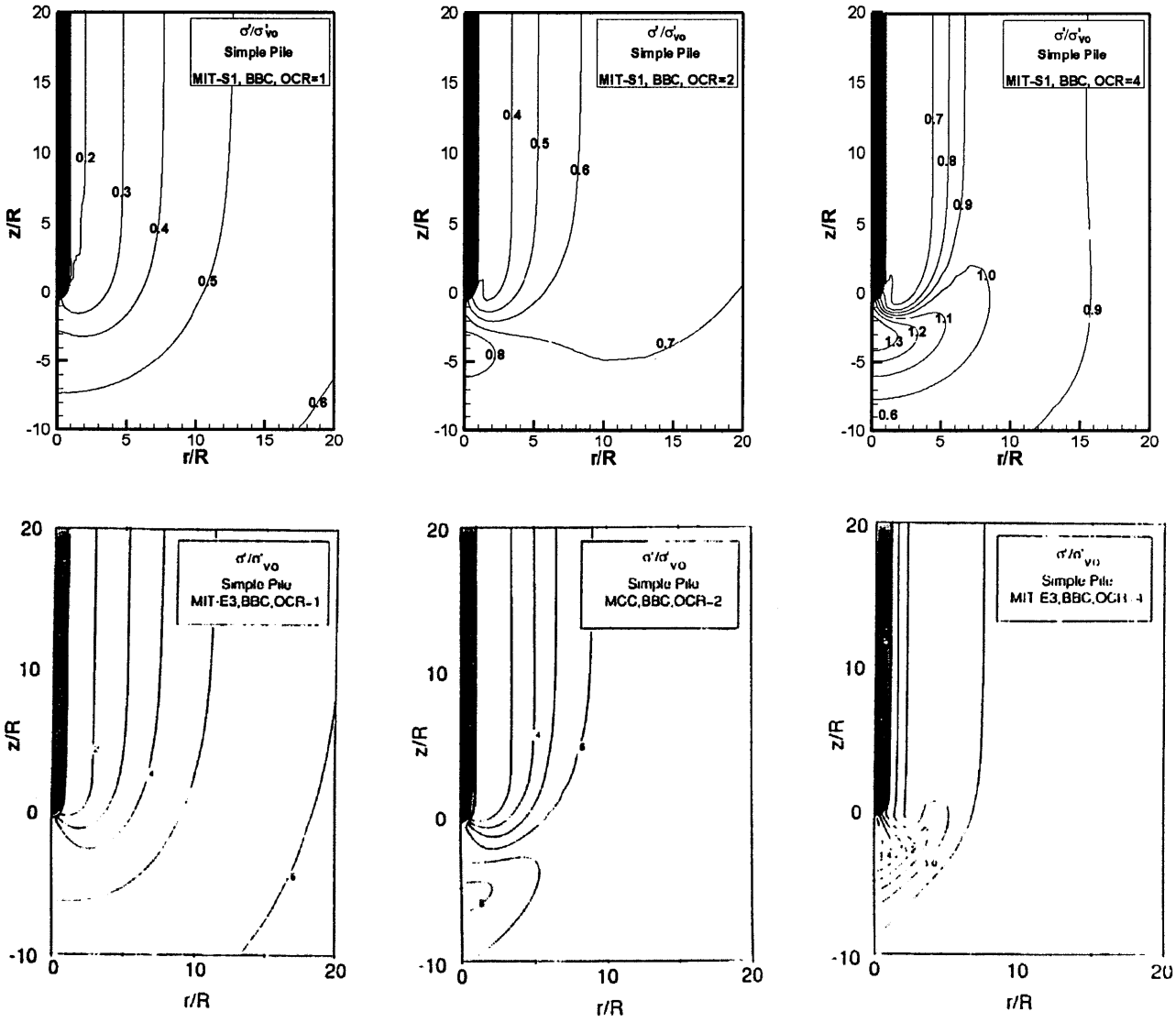

Figure 3.9: Effect of soil model on predictions of installation stresses, σ'/σ'_{vo}

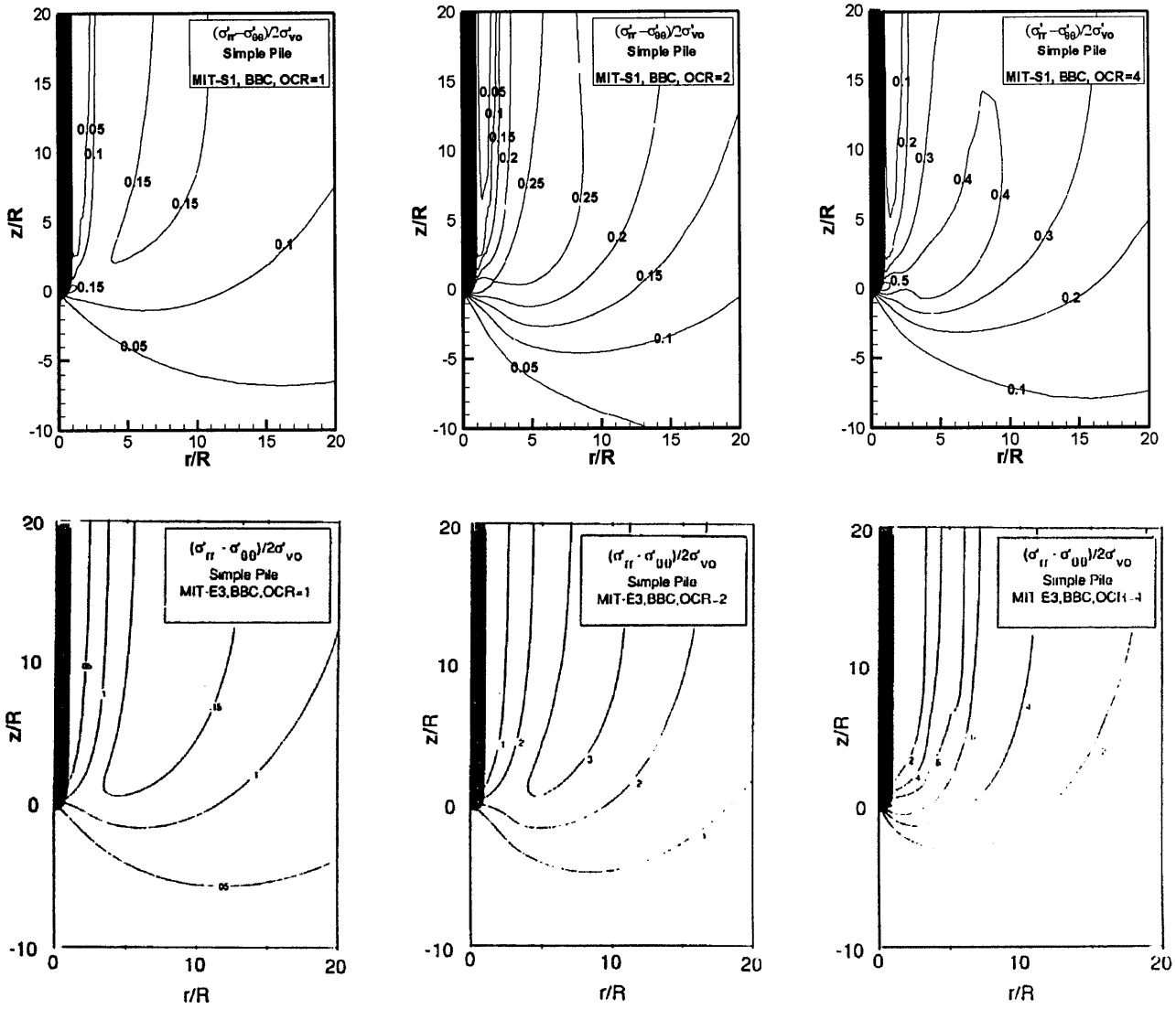

Figure 3.10: Effect of soil model on predictions of installation stresses, $(\sigma'_r-\sigma_\theta)/2\sigma'_{vo}$

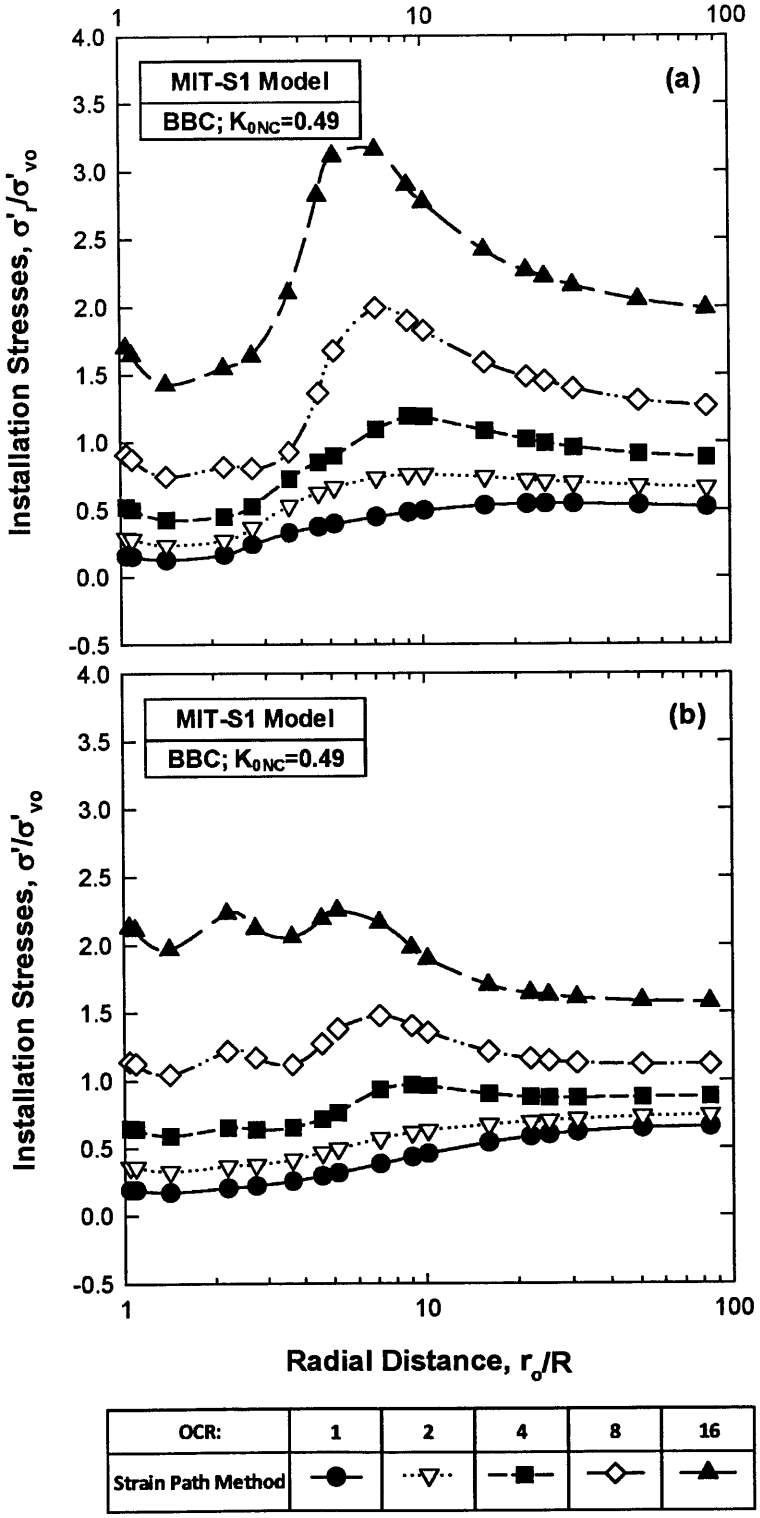

Figure 3.11: Effect of overconsolidation ratio (OCR) on predictions of installation stresses; (a) σ'_r/σ'_{vo}, (b) σ'/σ'_{vo}

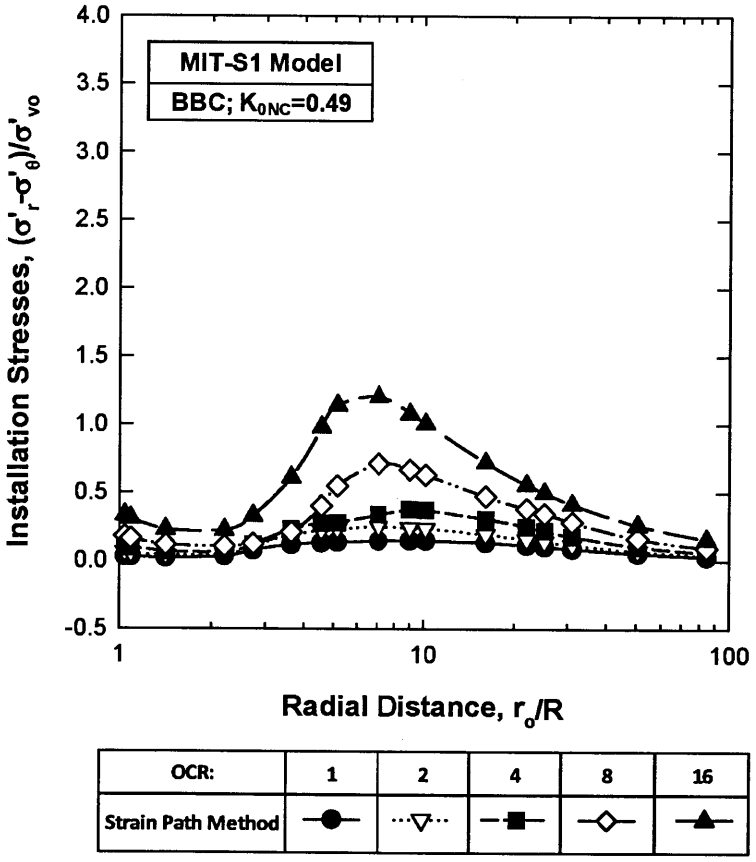

Figure 3.12: Effect of overconsolidation ratio (OCR) on predictions of installation stresses, $(\sigma'_r-\sigma_\theta)/\sigma'_{vo}$

4. PENETRATION PORE PRESSURES

4.1 INTRODUCTION

Pore-water pressures occupy a central position in modern soil mechanics for conceptual and practical reasons. Conceptually, effective stresses control most soil behavioral aspects of interest to geotechnical engineers, while total stresses are controlled by equilibrium considerations. Therefore, pore pressures are necessary to estimate effective stresses from calculated total stresses and thus allow a rational interpretation and/or prediction of the deformation response of soil masses.

The undrained penetration of a pile or any intrusive test device (e.g. piezocone, field vane, dilatometer, etc.) in low permeability clay leads to the development of excess pore pressure in the soil. For normally and moderately overconsolidated clays, these pore pressures are large and dominate other soil stresses and hence hold the key to the understanding of skin friction mechanisms and ultimately the rational prediction of shaft resistance of driven piles.

The pore pressures generated in the clay due to steady pile penetration, $\Delta u=u-u_o$, are the sum of two components: i) the increase in octahedral normal total stress, $\Delta\sigma$, and; ii) the shear induced pore pressure, Δu_s. The main objective of this chapter is to calculate the installation pore pressures around the shaft of a pile in K_0-consolidated Boston Blue Clay (BBC). An evaluation of the installation predictions will follow by comparing the analytical results with field/laboratory measurements from several sites.

4.2 PENETRATION PORE PRESSURES USING SPM

According to Baligh (1985), the effects of gravity on stress changes in deep foundation problems are negligible, thus the equilibrium equations in a cartesian frame can be expressed in terms of total stresses as:

$$\frac{\partial \sigma_{ij}}{\partial x_j} = 0 \tag{4.1}$$

in which, x_i ($=x_1,x_2,x_3$) are the coordinates of a material point and repeated indices imply summation. By invoking the effective stress principle, $\sigma_{ij}=\sigma'_{ij}+\delta_{ij}u$, it can be shown that,

$$\frac{\partial u}{\partial x_i} = -\frac{\partial \sigma'_{ij}}{\partial x_j} = g_i \tag{4.2}$$

Alternatively, from a known field of deviatoric stresses, the changes in mean total stress, $\Delta\sigma$, is determined from:

$$\frac{\partial \sigma}{\partial x_j} = -\frac{\partial s_{ij}}{\partial x_j} \tag{4.3}$$

whereupon, the excess pore pressure can be computed from:

$$\Delta u = \Delta\sigma + \Delta u_s \tag{4.4}$$

For axi-symmetric problems, the equilibrium equations in terms of effective stresses can be expressed in a cylindrical coordinate frame as:

$$-\frac{\partial u}{\partial r} = \frac{\partial \sigma'_{rr}}{\partial r} + \frac{\partial \sigma'_{rz}}{\partial z} + \frac{\sigma'_{rr} - \sigma'_{\theta\theta}}{r} \tag{4.5}$$

$$-\frac{\partial u}{\partial z} = \frac{\partial \sigma'_{zz}}{\partial z} + \frac{\partial \sigma'_{rz}}{\partial r} + \frac{\sigma'_{rz}}{r} \tag{4.6}$$

According to the Strain Path Method, the excess pore pressures are derived by integrating in either the radial (*Equation 4.5*) or the vertical (*Equation 4.6*) direction. This condition is only satisfied if the strain paths are compatible with the model used to determine the stresses. However, from the first step of the SPM, the strains are approximated using potential flow theory and are not compatible with the soil model used afterwards.

An approach suggested by Baligh (1985) can ameliorate the difficulties associated with the path dependent pore pressures by taking the divergence of *Equation 4.2*,

$$\nabla^2 u = -\nabla g = -q \tag{4.7}$$

In general, Poisson pore pressures fields will not satisfy either equilibrium equation exactly. However, the Poisson solution does not rely upon an arbitrary selection of an integration path; it therefore provides a flexible method for extending SPM solutions to penetrometers of general shape.

In principle, the flux term, q, can be calculated by numerical differentiation of the stress components from the SPM. However, accurate numerical evaluation of second derivatives is very difficult to achieve, especially in regions of high stress gradients. Considerable simplifications in computing can be achieved using the divergence theorem to estimate an average flux within a given finite element:

$$\int_{V} q \, dV = \int_{A} g \cdot n \, dS \tag{4.8}$$

$$\overline{qV} = \sum_{i=1}^{n} (g \cdot n)_i \ \Delta S_i \tag{4.9}$$

where, V is the volume of the element, g is the pore pressure gradient vector on side i of the n-sided element, n is the unit vector normal to side i of the element and S_i is the surface area of side i of the element.

Regarding to the first derivatives of the effective stresses (g_r,g_z), Aubeny (1992) obtained accurate numerical solutions using an isoparametric interpolation scheme. The same procedure has been adopted in this research.

4.3 INSTALLATION PORE PRESSURES

This section presents predictions of pore pressure changes, ($u-u_o$), following pile penetration in K_0-consolidated Boston Blue Clay (BBC). Predictions are made to assess the effects of: i) method of analysis (CEM & SPM); ii) soil model (MIT-E3 & MIT-S1); and iii) stress history (OCR=1, 2, 4, 8 & 16) on excess pore pressure distribution.

4.3.1 Effect of installation analysis

The cylindrical Cavity Expansion Method (CEM) predictions are obtained by means of the method described thoroughly in *Section 3.2.2.1.* Integration of the equilibrium equation in the radial direction begins at a radius equal to 150 times the radius of the cavity where the initial (K_0) stresses and the ambient (hydrostatic) pore pressures are imposed.

The Strain Path Method (SPM) predictions are determined by means of the method described extensively in *Section 4.2.2*. *Figure 4.1* shows the finite element mesh used in the pore pressure calculations representing a cylindrical pile using the Simple Pile Solution. Subsequent studies of pore pressures around the pile shaft are selected at an elevation z=20R above the tip. At this elevation, there is minimal variation of stresses (see *Section 3.3.3*) in the vertical direction and thus no significant change occurs in the same direction for pore pressures as well.

Figure 4.2 presents Strain Path (SPM) and cylindrical Cavity Expansion (CEM) predictions of installation pore pressures, $(u-u_o)/\sigma'_{vo}$, using the MIT-S1 soil model for five overconsolidation ratios, OCR=1.0, 2.0, 4.0, 8.0 and 16. The following remarks can be made:

- For all OCR's, the CEM analyses predict pore pressures at the pile shaft which are 25 to 55% larger than those predicted by the SPM analyses, except for the case of OCR=1.
- The shape of excess pore pressure distribution around the shaft exhibits characteristic trends for all OCR's. More specifically, all Cavity Expansion solutions predict an almost logarithmic[12] increase of the excess pore pressure in the region close to the cavity (i.e. $r_o/R<10$), since the stresses are approximately constant[13] in this region. The Strain Path Method predicts an almost constant distribution of the excess pore pressure in the immediate vicinity of the pile (i.e. $r_o/R<2$) for every overconsolidation ratio.

[12] shown as linear in the semi-log plot
[13] indicating that the Critical State is reached

4.3.2 Effect of soil model

Pestana (1994) has shown that much more realistic predictions of the behavior of highly overconsolidated clays (with OCR≤32) measured in laboratory tests can be achieved using the MIT-S1 soil model. *Figure 4.3* shows installation pore pressures, $(u-u_o)/\sigma'_{vo}$, around the Simple Pile for OCR's=1, 2 and 4. When compared with the predictions for the MIT-E3 model (*Figure 4.3*) the following effects of soil model can be observed:

- Predictions of the MIT-E3 and MIT-S1 models are very similar in all respects. This confirms that the MIT-S1 captures all aspects of the MIT-E3 model providing better predictions for overconsolidated clays.
- Major difference between the two soil models, MIT-E3 and MIT-S1, is related to the region where the maximum excess pore pressures occur. For OCR's=1 and 2, the MIT-E3 model predicts that maximum excess pore pressure appears at locations along the face of the pile. The excess pore pressures around the face ($-0.5\leq z/R\leq 1.7$) are up to 30-40% lower for the MIT-E3 model as compared to MIT-S1 results for OCR=1 and 2. At locations far above the tip, however, the two soil models give very similar results of $(u-u_o)/\sigma'_{vo}$ acting on the pile wall.
- The MIT-S1 compared to the MIT-E3 model predicts a much larger zone of disturbance (i.e. $(u-u_o)/\sigma'_{vo}$) around the pile. This difference between these two models increases as the OCR increases.

4.3.3 Effect of stress history

Figure 4.4 summarizes the predictions of installation pore pressures around the Simple Pile for the base case analysis (MIT-S1; K_0-consolidated BBC) at OCR's=1, 2, 4, 8 and 16. The excess pore pressures are reported at locations: (a) radially around the shaft of the penetrometer at steady state conditions (far above the tip of the penetrometer), and (b) along the centerline (ahead of the tip) and surface of the penetrometer geometry. The results present the following:

- The shape of excess pore pressure distribution along the radial direction is similar for all OCR's. However, as OCR increases there is a significant increase in $(u-u_o)/\sigma'_{vo}$ at the pile shaft.
- According to *Figure 4.4b*, the maximum excess pore pressures, $(u-u_o)/\sigma'_{vo}$ >2-3, occur at the tip of the pile. More modest changes occur at locations around the pile shaft. This last observation explains up to a point the satisfactory agreement between one-dimensional radial solutions $(u-u_o)/\sigma'_{vo}$ (e.g. Whittle, 1987) and two-dimensional solutions on the shaft far above the pile tip.

4.4 EVALUATION OF INSTALLATION PREDICTIONS

In this section, the analytical predictions of pile installation are compared directly with field/laboratory data from separate sites. These comparisons are trying to illustrate the capabilities and limitations of the Cavity Expansion and Strain Path analyses for predicting the installation pore pressures following the penetration of a pile.

4.4.1 Field Tests and Laboratory Experiments

Simultaneous measurements of shaft pore pressures and lateral earth pressures (radial total stresses; σ_r) during installation have been obtained at a number of sites using: i) instrumented pile shaft elements or probes (PLS cell, Morrison, 1984; t-z and x-probes, Bogard et al., 1985; IMP, Coop & Wroth, 1989); instrumented model piles (Kalsrud & Haugen, 1985; Kalsrud et al., 1992; Bond et al., 1991). Further measurements of installation pore pressures are associated with the development of in-situ testing devices such as the piezocone and include both filed tests and laboratory experiments in large scale calibration chambers.

Before proceeding to a direct comparison of the analytical results with the measured data, a brief outline of the seven (7) well-documented cases reported herein, will be given. These cases are: i) Saugus, MA (Morisson, 1984); ii) St Alban, Quebec (Roy et al., 1981); iii) Onsøy, Norway (Kalsrud et al., 1992); iv) Empire, LA (Azzouz & Lutz, 1986); v) Haga, Norway (Kalsrud & Haugen, 1985); vi) Inchinnan, Scotland (May, 1987); and vii) Kaolin (May, 1987; Nyirenda,1989).

4.4.1.1. Saugus, MA

In-situ measurements on a closed-ended model pile shaft referred to as the Piezo-lateral Stress cell (PLS) were performed at the station 246 of the I-95 test embankment in Saugus, Massachusetts (Morisson, 1984). Extensive field and laboratory testing has been carried out at the site to establish stratigraphy and engineering properties of the site. *Figure 4.5* shows the soil profile, index properties and stress history at the site. In situ overconsolidations ratios range from OCR=7 at depth d=30 ft. to OCR=1.23 at d=120 ft.

4.4.1.2. St Alban, Quebec

A full scale investigation with six instrumented test piles has been carried out on the Saint Alban test site in order to study the behavior of friction piles in soft sensitive soils (Roy et al., 1981). The test site is located about 80 km west of Quebec City at the northern fringe of the Saint-Laurent low lands. The typical soil profile consists of 0.4 m of top soil, 1.2 m of weathered clay crust, 8.2 m of soft silty clay of marine origin, 4.0 m of very soft clayey silt, and a deep layer of dense sand extending from a depth of 13.7 m to more than 25 m. *Figure 4.6* shows the soil profile, index properties and stress history at the site.

4.4.1.3. Onsøy, Norway

Onsøy clay is a thick deposit of highly uniform marine clay. The test site is situated in southeastern Norway. A wide variety of in situ devices and different laboratory tests have been used to investigate the properties of the material (Kalsrud et al., 1992). *Figure 4.7* shows the plasticity data of Onsøy clay (Lunne et al., 2003). Overconsolidation ratio values have been determined directly from oedometer tests and range from OCR≃5 at depth d=5 m. to OCR≃1.5 at d=35 m.

4.4.1.4. Empire, LA

The test site at Empire is situated in the Mississippi Delta, approximately 40 miles south of New Orleans. The site has been used for several research programs since 1975, which studied the behavior of friction piles. *Figure 4.8* presents a profile of index

properties, stresses and undrained shear strength as reported by Azzouz & Lutz (1986) based on pre-1984 laboratory data.

4.4.1.5. Haga, Norway

The Norwegian Geotechnical Institute conducted one of the most comprehensive pile load-test programs at the Haga test site, 50 km outside of Oslo, between 1980 and 1984 (Kalsrud & Haugen, 1985). The program included both monotonic and cyclic axial load tests on 16 heavily instrumented piles and 11 non-instrumented piles on the same dimension. *Figure 4.9* shows the soil profile at the test site, comprising a lean marine clay (Haga clay) extending to 4.5 m depth. The preconsolidation pressures measured by incremental oedometer tests give overconsolidation ratios decreasing from OCR=7 at 5 at depth d=1 m. to OCR=3 at d=5 m.

4.4.1.6. Inchinnan, Scotland

The test site at Inchinnan is located just over 1 km to the south of Glasgow's Abbotsinch Airport. The first phase of site investigation at this specific site was carried out using the 1 cm^2 and 5 cm^2 Oxford piezocone and a 10 cm^2 Fugro piezocone. The second phase of the investigation consisted of a borehole, which produced 13 consecutive samples giving a complete recovery from 1.2 m to 13.1 m. The details of the material grading and Atterberg limits are given on *Figure 4.10*.

4.4.1.7. Kaolin

The principal objective of this small scale laboratory experiment was to measure the change in radial stress at the calibration chamber wall wall due to probe penetration at the center of the chamber of radius, R_c=50 cm (May, 1987; Nyirenda, 1989). The test described above was performed on speswhite kaolin clay with the corresponding properties shown in *Table 4.1.*

4.4.2 Comparison with measured data

Figure 4.11 compares MIT-S1 predictions of excess pore pressures at the pile shaft during steady penetration in K_0-consolidated BBC with measurements obtained from the sites mentioned above. In general, the measured data are very consistent at low OCR (i.e. $(u-u_o)/\sigma'_{vo}=2\pm0.4$ for OCR<3), but exhibit large scatter in the more overconsolidated clay (i.e. OCR>3). Significantly lower installation pore pressures (i.e. $(u-u_o)/\sigma'_{vo}$=1.2-1.3) have been reported from laboratory calibration chamber tests in kaolin (May, 1987; Nyirenda, 1989). As a rule, the Strain Path predictions underestimate the measured pore pressures, particularly at low OCR, while there is a better agreement with results from CEM analyses. On the other hand, there is a better agreement between the SPM predictions and the pore pressures measured in kaolin for the entire range of OCR (i.e. 1<OCR<10), which are the only results measured in the laboratory.

Figure 4.12 compares MIT-S1 predictions of the excess pore pressure distribution using both methods of analysis (i.e. SPM and CEM) for K_0-consolidated BBC at OCR i) field measurements (Roy et al., 1981) around an instrumented pile installed in St Alban clay at OCR≃2.3; and ii) measurements around the shaft of a cone penetrometer installed

in speswhite kaolin clay within a large calibration chamber (of radius, Rc=50cm). In general, CEM analyses do not describe accurately the shape of the pressure distribution and hence, overestimate $(u-u_o)/\sigma'_{vo}$ at the shaft while underestimating pore pressures measured in the far field. In contrast, the SPM predictions at OCR=1 are in very good agreement with penetration pore pressures measured in kaolin. In the case of St Alban clay, the SPM predictions at OCR=2 capture overall the shape of the pore pressure distribution but they tend to underestimate both the magnitude and the radial extend of the disturbance zone.

Soil Properties	Values
Liquid Limit, LL	66%
Plasticity Index, PI	33%
Specific Gravity, G_s	2.65
Peak Friction Angle	23o
Coefficient of consolidation, c_v	0.5 mm^2/sec
Slope of virgin consolidation line, λ	0.25
Slope of swelling line, κ	0.05
Normally consolidated rigidity index, $I_r=G/c_u$	150-250*

*Note: These values were measures in standard CIU triaxial tests from initial loading and unload-reload loops. Displacements were measured external to the cell on the loading ram

Table 4.1: Soil properties of speswhite kaolin clay, (May, 1987; Nyirenda, 1989)

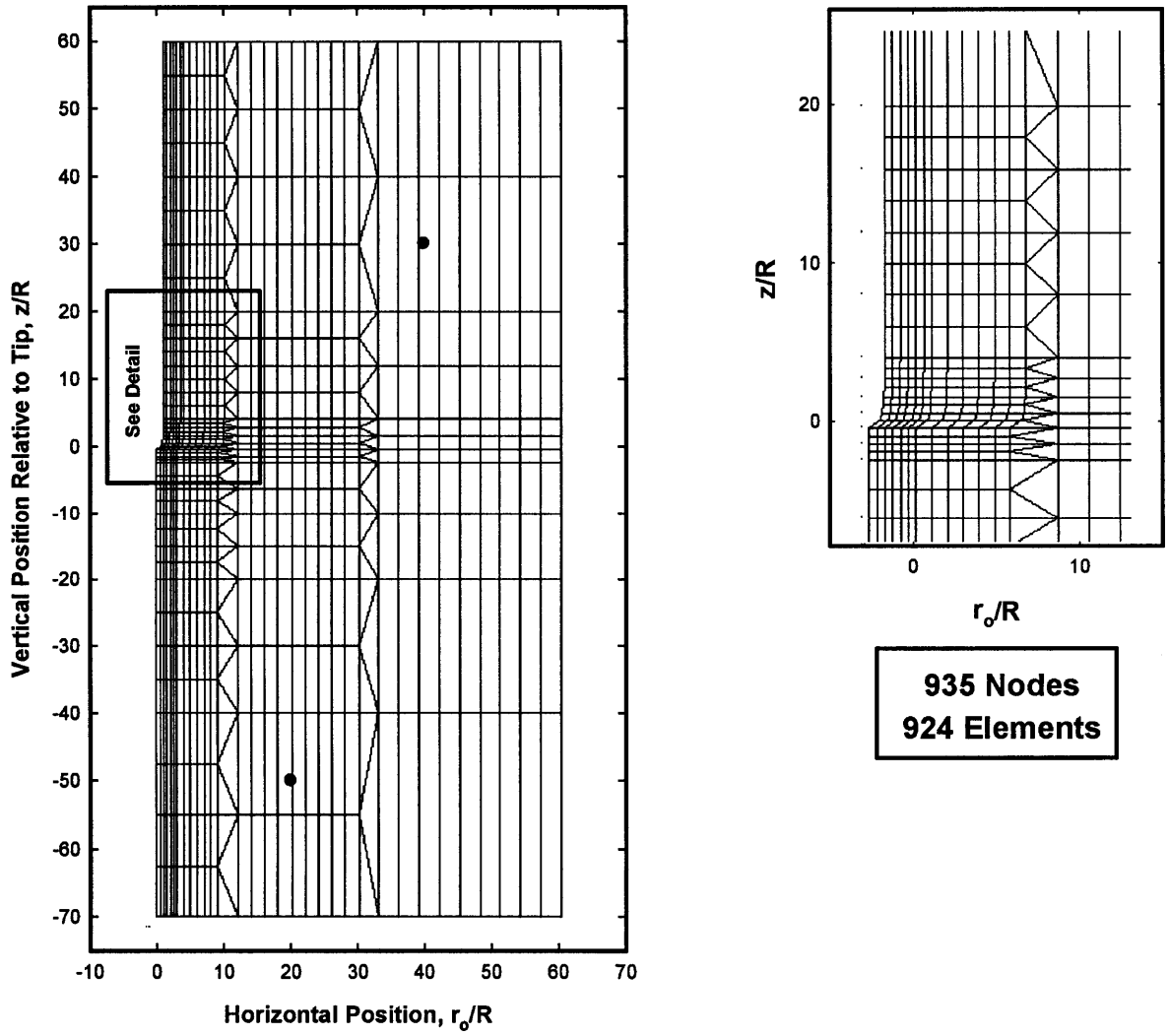

Figure 4.1: Finite Element Mesh for Strain Path Method (SPM) Analysis

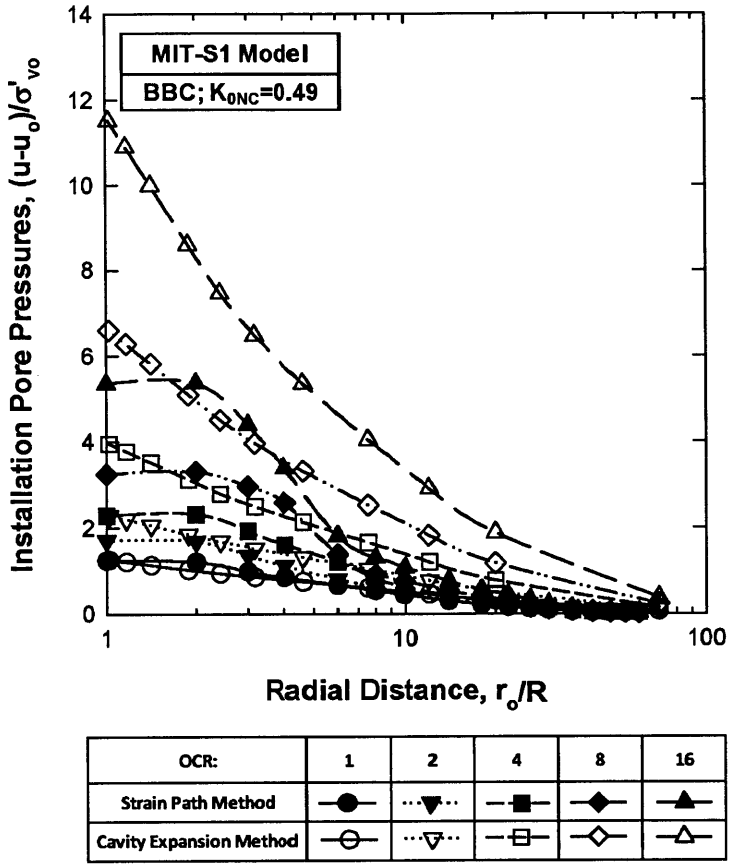

Figure 4.2: Effect of overconsolidation ratio (OCR) on predictions of installation pore pressures, $(u-u_o)/\sigma'_{vo}$ in BBC using the MIT-S1 soil model

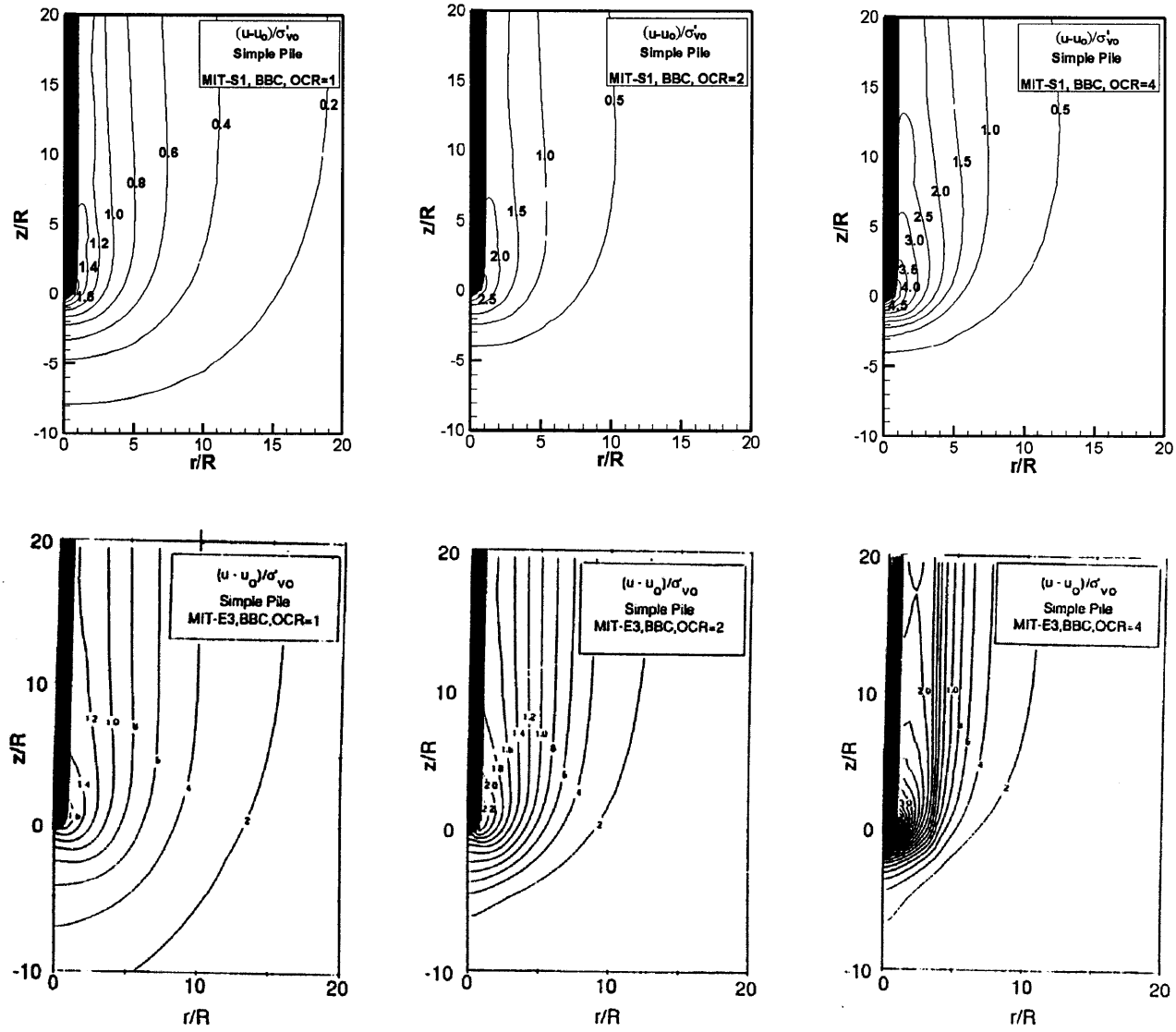

Figure 4.3: Effect of soil model on predictions of installation pore pressures, $(u-u_o)/\sigma'_{vo}$

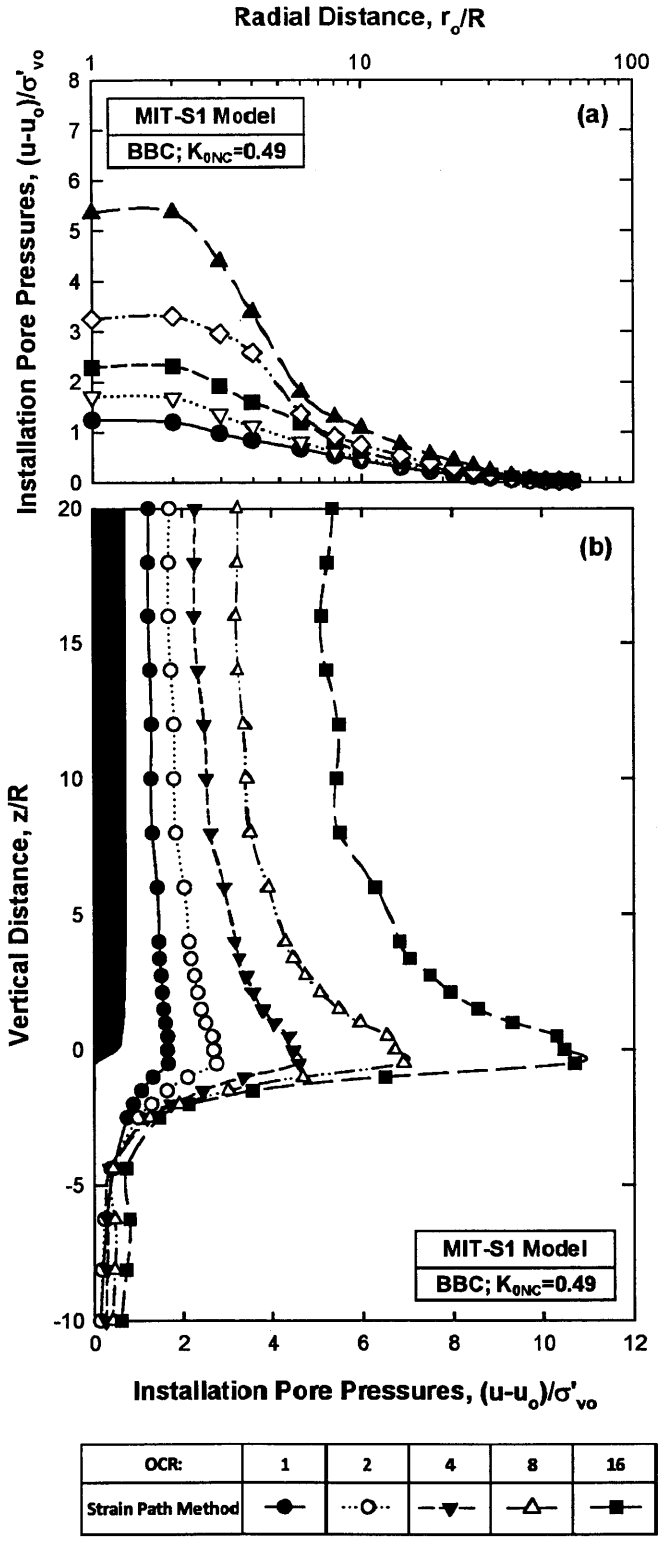

Figure 4.4: Effect of overconsolidated ratio (OCR) on predictions of installation pore pressures, $(u-u_o)/\sigma'_{vo}$, in BBC using MIT-S1 (a) radial distribution around shaft; (b) vertical distribution along surface of penetrometer

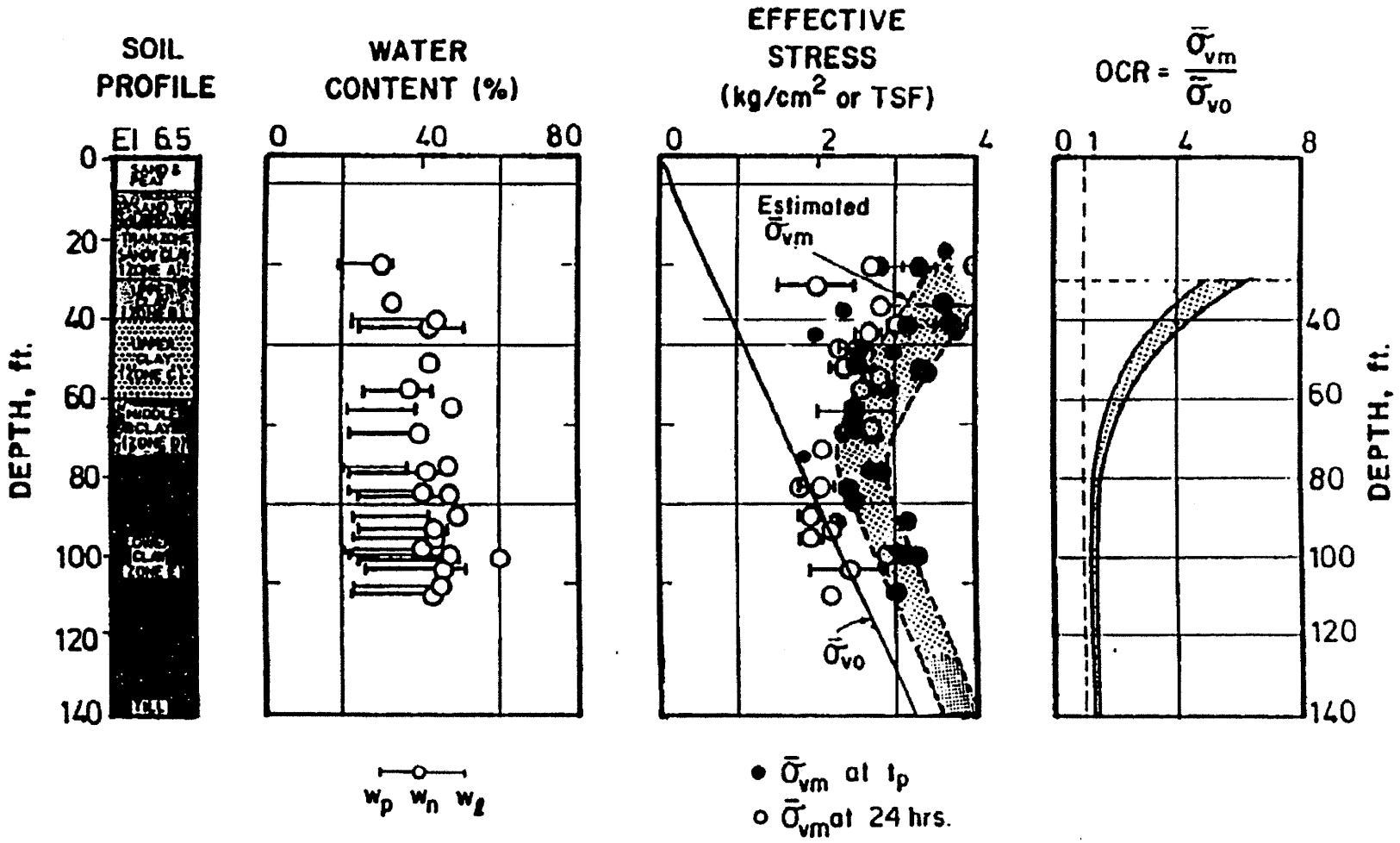

Figure 4.5: Index properties and stress history, Saugus test site (Morisson, 1984)

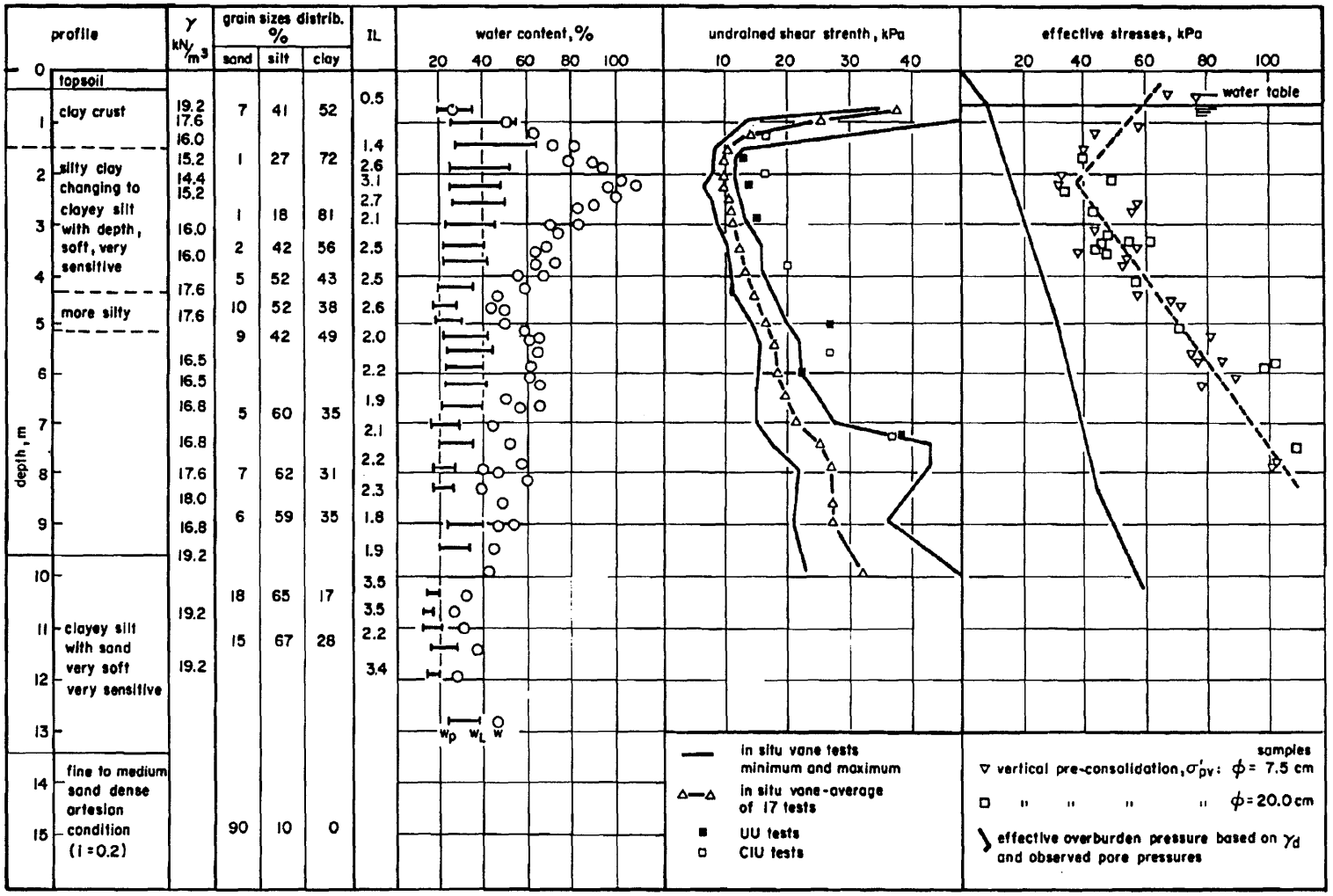

Figure 4.6: Index properties, undrained shear strength and stress history, St Alban test site (Roy et al., 1981)

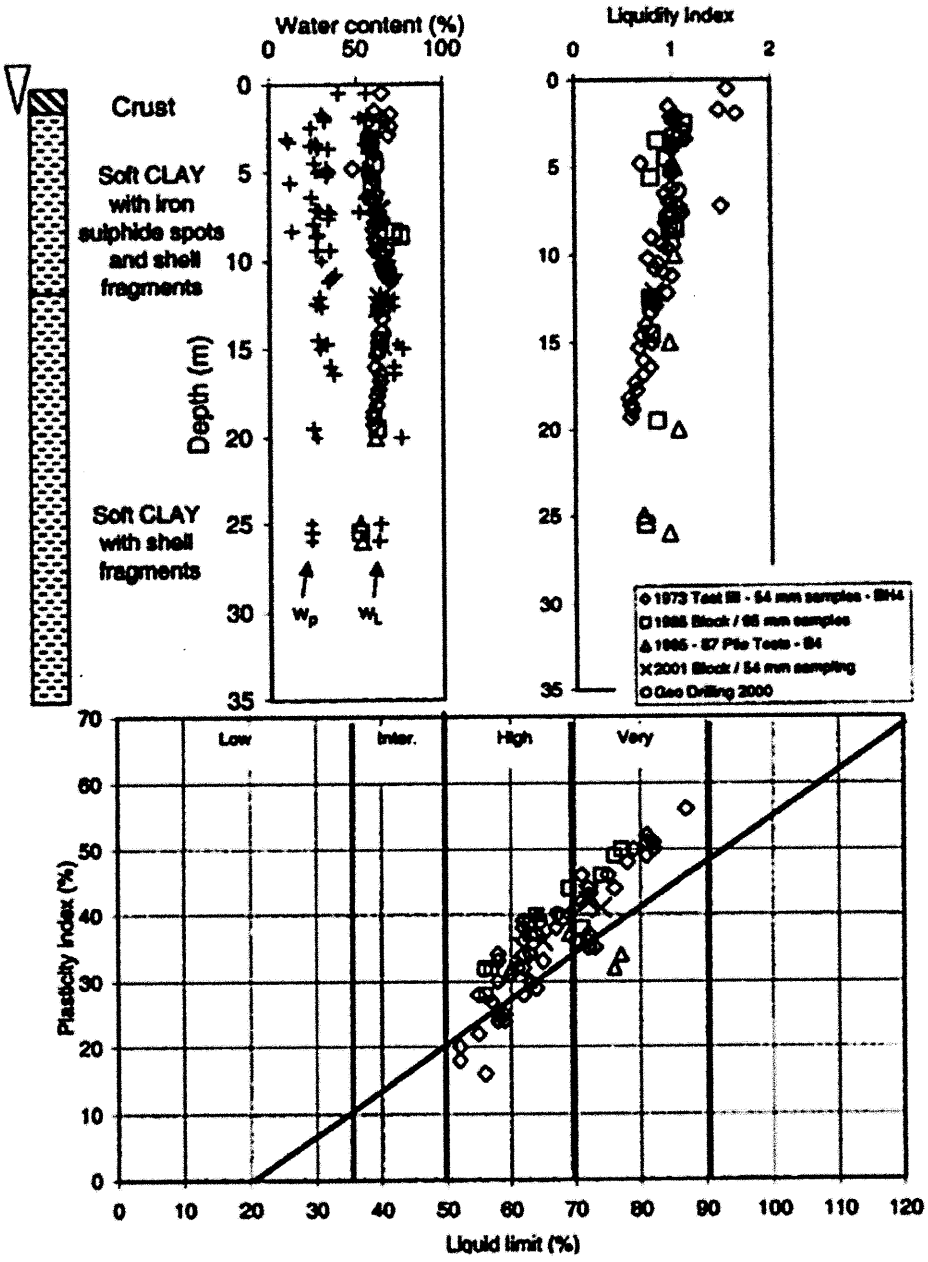

Figure 4.7: Index properties, Onsøy test site (Lunne et al., 2003)

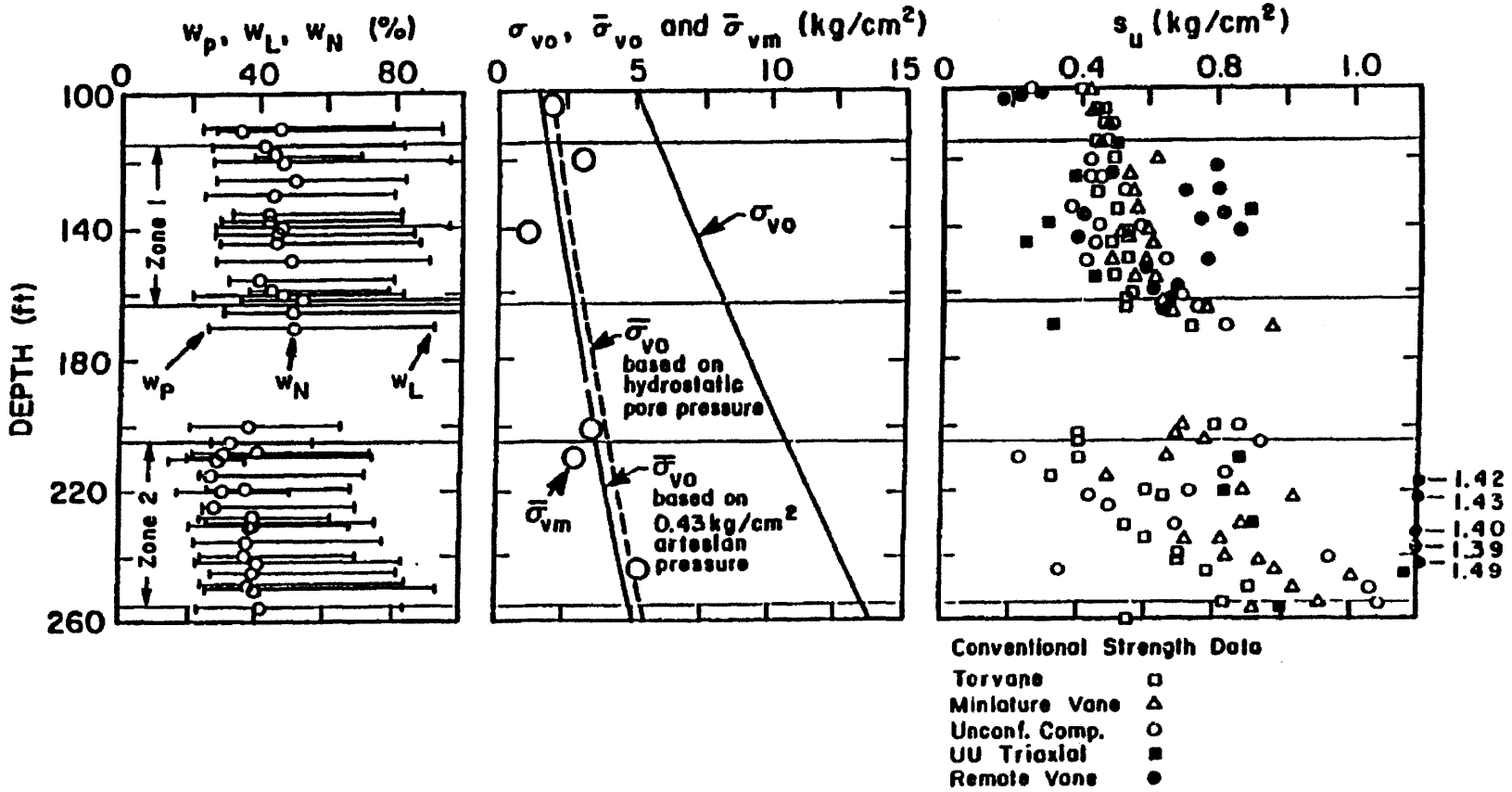

Figure 4.8: Index properties, undrained shear strength and stress history, Empire test site (Azzouz & Lutz, 1986)

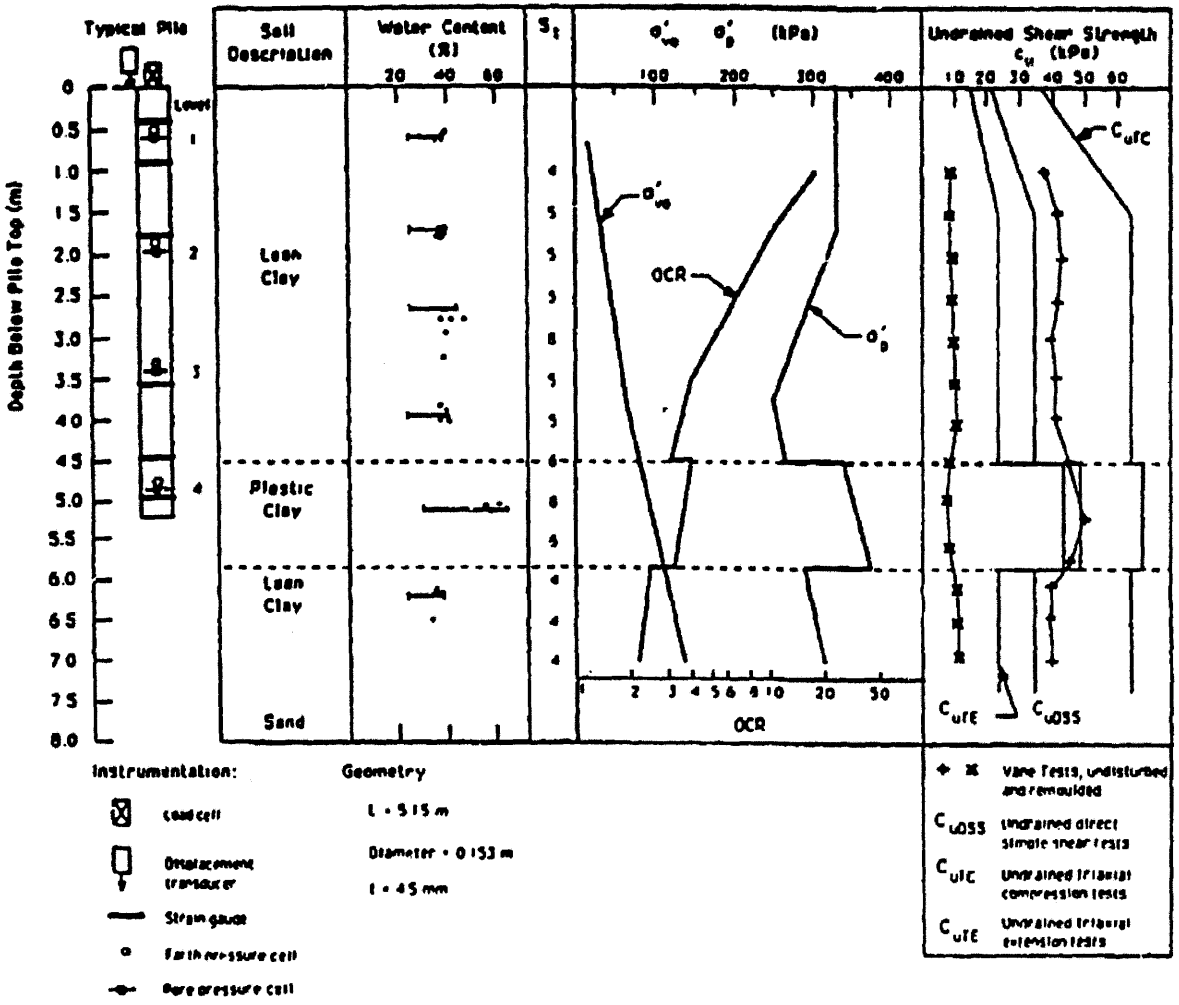

Figure 4.9: Index properties, undrained shear strength and stress history, Haga test site (Kalsrud & Haugen, 1985)

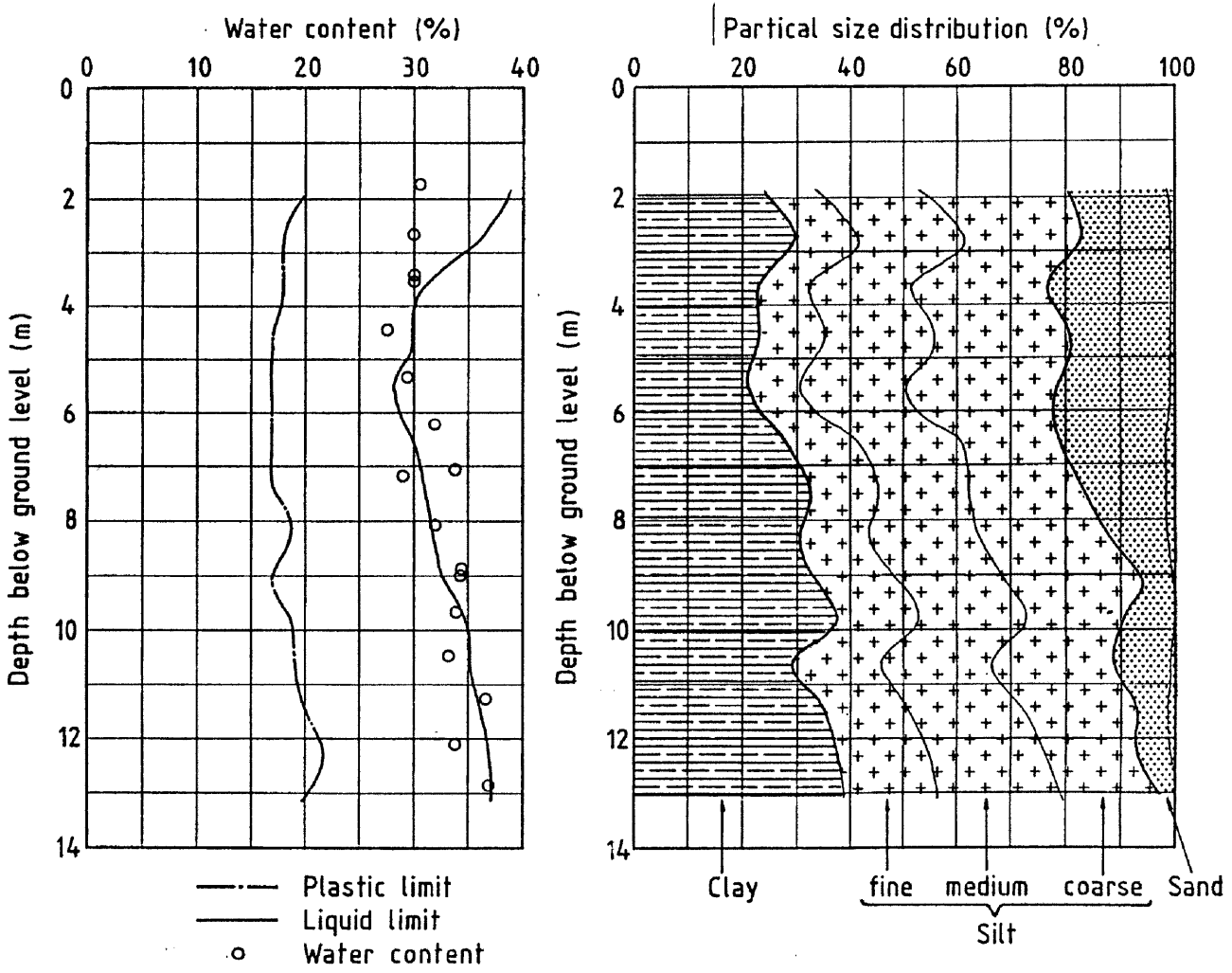

Figure 4.10: Index properties and particle size distribution, (May, 1987)

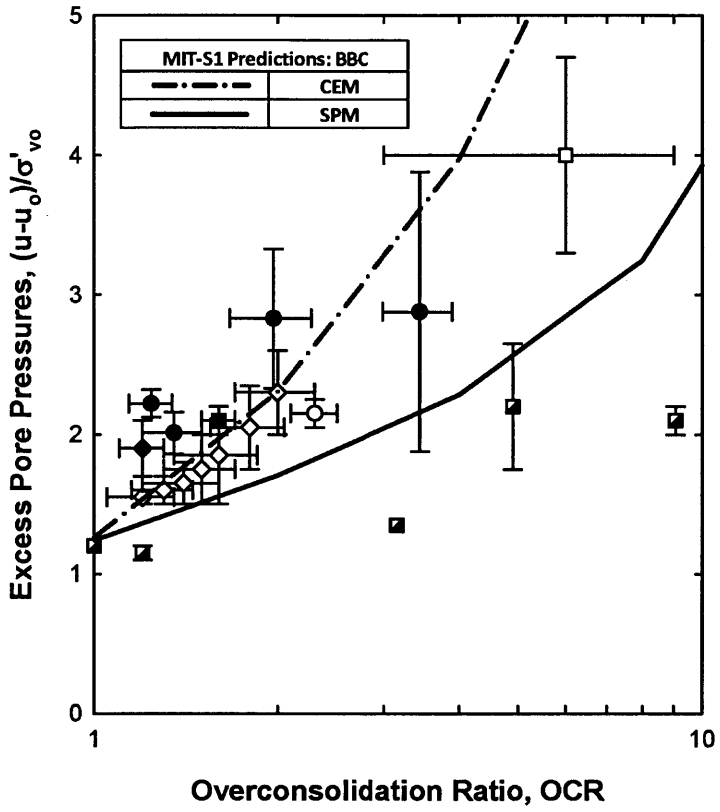

Measured Data		
Symbol	**Clay**	**Reference**
●	BBC	Morrison (1984)
○	St Alban	Roy et al. (1981)
◆	Onsøy	Karlsrud et al. (1992)
■	Empire	Azzouz & Lutz (1986)
□	Haga	Karlsrud & Haugen (1985)
◇	Inchinnan	May (1987)
◪	Kaolin	May (1987); Nyirenda(1989)

Figure 4.11: Evaluation of installation pore pressures at pile shaft

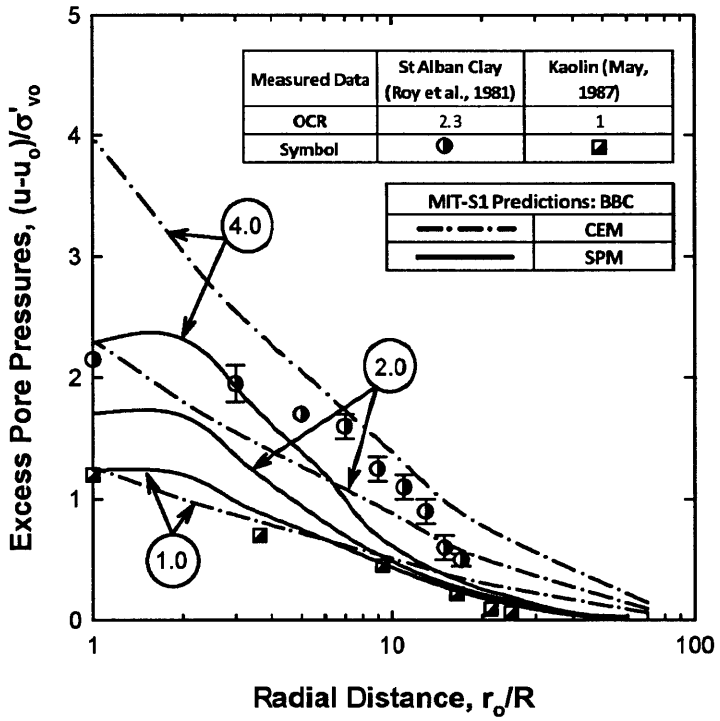

Figure 4.12: Distribution of excess pore pressure during installation

5. CONSOLIDATION AROUND DRIVEN PILES

5.1 INTRODUCTION

The previous chapters (*Chapters 3 and 4*) have described the effective stresses and excess pore pressures which develop during steady penetration of driven piles in low permeability clays. When the penetration process is interrupted, excess pore pressures dissipate and there are concomitant changes in the effective stresses. This process corresponds to a process of radial consolidation around the shaft of the pile.

It is well established fact that the shaft resistance of piles in clay increases with time due to soil consolidation. However, the time taken to reach the maximum resistance varies significantly with: i) soil properties (e.g. permeability, compressibility); and ii) pile conditions (e.g. radius, permeability). The objective of soil consolidation analyses around pile shafts is to estimate the time dependent changes in effective stresses within the soil mass around the pile shaft. Stress conditions close to the pile shaft play a crucial role in controlling subsequent pile loading and hence control pile capacity.

This chapter summarizes the existing methods used to analyze consolidation around the pile shaft. Numerical algorithms used to integrate the MIT-S1 soil model in the general purpose finite element code ABAQUS[14] are described in *Section 5.3*. Predictions of consolidation along with numerical issues encountered in the application of MIT-S1 are presented in detail in *Section 5.4*. Finally *Section 5.5* compares results of the current analyses using the MIT-S1 with prior solutions using MIT-E3 (Whittle, 1992).

[14] ABAQUS is commercially available from SIMULIA and is made available through an academic license

5.2 BACKGROUND

Consolidation studies are generally treated by means of one of two theories: i) the Terzaghi (1923) - Rendulic (1936) uncoupled theory which treats the excess pore pressures independent of the total stresses during consolidation; and ii) Biot (1935) coupled theory where the interaction between total stresses and pore water pressures is considered.

5.2.1 Consolidation Theories

Terzaghi (1923) formulated the one-dimensional consolidation theory to rationalize observations of time-dependent settlements of soil. His theory still represents the backbone of consolidation analyses in geotechnical engineering and is based on the assumption that, at any time, the strain in the soil is controlled by changes in effective stresses.

To avoid the oversimplification of one-dimensionality, Rendulic (1936) formulated a three-dimensional consolidation theory based on the assumption that the mean total stress, σ, does not change during consolidation. Viggiani (1970) and Davis & Poulos (1970) show that in a wide range of practical problems Rendulic's theory predicts fairly well the pore pressure dissipation profiles but has serious limitations in predicting the changes in effective stresses during consolidation.

Biot (1935) formulated a general coupled consolidation theory, which is based on the assumptions:

- The soil is fully saturated.

- Soil deformation is associated with infinitesimal strains and rotations, i.e. geometric non-linearities are neglected. However, non-linearities resulting from the constitutive law are included.
- Soil deformations and pore fluid flow occur under quasi-static conditions.
- Consolidation occurs under isothermal conditions, which means that the conservation of energy law is redundant.

Under these conditions, the Biot theory can be derived from the conservation laws of Mechanics: i) the Conservation of Momentum; and ii) the conservation of mass, as follows:

$$\nabla \cdot \boldsymbol{\sigma} + \mathbf{f} = 0 \tag{5.1}$$

$$\nabla \cdot \left[\mathbf{k} \cdot \nabla \left(u - u_o \right) \right] = -\rho g \dot{\varepsilon} \tag{5.2}$$

where, $\boldsymbol{\sigma}$ is a total stress tensor, $\mathbf{f}$ is a vector of body forces/volume of soil, $\mathbf{k}$ is the hydraulic conductivity tensor, $(u-u_o)$ is excess pore water pressure, ρ is the pore fluid density, g is the acceleration of gravity and $\dot{\varepsilon}$ is the volumetric strain rate.

In general, these two equations must be solved simultaneously in conjunction with a constitutive law for the stress-strain behavior of the soil. As a result, the consolidation problem involves coupling of the change in effective stresses with the pore pressures.

For a linear isotropic elastic soil, Sills (1975) shows that for the case of radial consolidation around piles, around piles the general Biot theory reduces to the uncoupled form:

$$c\nabla^2 \left(u - u_o \right) = \frac{\partial u}{\partial t} \tag{5.3}$$

where, the differential operator is defined as:

$$\nabla^2 = \frac{\partial^2}{\partial r^2} + \frac{1}{r}\frac{\partial}{\partial r} \tag{5.4}$$

and c is the coefficient of consolidation given by:

$$c = \frac{k}{\gamma_w} \cdot \frac{3K(1-\nu')}{(1+\nu')} \tag{5.5}$$

where, γ_w is the unit weight of water, K is the bulk moduli and ν' is the drained Poisson's ratio.

The limitations of this analytic solution are obvious: the soil is assumed linear, elastic and isotropic, which is not a realistic assumption for soils. Thus, the main reason for presenting Sills analytic solution is to check the results of the Finite Element numerical discussed hereafter rather than to obtain realistic predictions for the pore pressure dissipation rates.

5.2.2 Theoretical Framework

The flow chart in *Figure 5.1* summarizes the analyses that are used to predict the dissipation of penetration-induced pore pressures in clay. The calculations are subdivided into two phases: i) simulation of undrained pile penetration conditions using either the Strain Path Method (SPM) or the cylindrical Cavity Expansion Method (CEM); and ii) finite element calculations of pore pressure dissipation. During penetration, the changes in soil stresses can be computed by either total stress or effective stress soil models, while pore pressures are obtained from equilibrium conditions. Two types of analyses are then possible for the dissipation phase:

1. Total stress soil models and Uncoupled consolidation (T-U Method).

   Simple total stress soil models (EPP-elastic perfectly-plastic; or HPP-hyperbolic-elastic, perfectly plastic) can provide realistic predictions of the shear stresses and excess pore pressures caused by undrained pile penetration in clays (Baligh & Levadoux, 1980; Teh & Houlsby, 1991). However, these same total stress models cannot describe changes in the effective stresses that occur during consolidation and hence, cannot simulate the process of set-up at the pile shaft. The dissipation of excess pore pressures, $(u-u_o)$, is then modeled as an uncoupled, linear consolidation problem. The dimensionless time factor for uncoupled consolidation is given by:

$$T = \frac{c \cdot t}{R^2} \tag{5.6}$$

   where, c is the coefficient of consolidation; t is the time after the pile installation; and R is the radius of the pile.

2. Effective stress soil models and Coupled consolidation (E-C Method).

   Analyses using effective stress soil models (MIT-E3, MIT-S1 etc.) can simulate the non-linear stress-strain behavior of the soil consistently throughout the installation and dissipation phases. This type of analyses is more complex involving non-linear soil behavior and coupling between pore pressures and total stress changes in the soil during the consolidation phase. All previous E-C analyses have assumed that pore water flow in the soil is controlled by D' Arcy's law, with constant (homogeneous) hydraulic conductivity, k. Hence, non-linearity

is controlled exclusively by stiffness changes of the soil skeleton. The time factor for the E-C analyses is then defined as:

$$T = \frac{\sigma'_o \cdot k \cdot t}{\gamma_w \cdot R^2} \tag{5.7}$$

where, σ'_o is the initial mean effective stress in the ground; k is the soil permeability (assumed isotropic and constant); t is the time after the pile installation; γ_w is the unit weight of water; and R is the radius of the pile.

5.2.3 One-dimensional non-linear consolidation

This section describes numerical procedures used to compute one-dimensional, non-linear, coupled consolidation around a driven pile. Consolidation is analyzed in this chapter assuming:

- The soil is fully saturated.
- Soil deformations and fluid flow occur under quasi-static conditions.
- Soil particles and the pore fluid are assumed to be incompressible.

The computations are performed using the finite element code ABAQUS. The relevant equations for coupled consolidation are based on: i) equilibrium, which can be expressed in terms of the principle virtual work,

$$\int_v \boldsymbol{\sigma} : \boldsymbol{\delta\varepsilon} dV = \int_s t \cdot \delta v dS + \int_v f \cdot \delta v dV \tag{5.8}$$

where, δv is a virtual velocity field, $\boldsymbol{\delta\varepsilon}$ is the virtual rate of deformation, $\boldsymbol{\sigma}$ is the true Cauchy stress, t are the surface tractions per unit area and f are the body forces per unit volume; and ii) continuity for fluid flow, which can be expressed as,

$$\int_V \frac{d}{dt}\left(\rho_w \frac{dV_w}{dV}\right)dV + \int_S \rho_w n v_w dS = 0 \tag{5.9}$$

where, V_w is the fluid volume within the control volume, V is the control volume and ρ_w is the fluid density. Discretization and solution of these equations are discussed in the ABAQUS Theory Manual (HKS, 2007).

Figure 5.2 displays a finite element mesh of 52 elements and 263 nodes extending to a radial distance 150 times the pile radius ($r_o/R=150$), which was used for solving the one-dimensional, non-linear, coupled consolidation around the shaft of a pile. The analyses use mixed elements with eight displacement nodes and four pore pressure corner nodes, which enable quadratic interpolation of displacements and linear interpolation of pore pressures. The selected boundary conditions during consolidation include the following considerations:

- At locations around the pile shaft, there is radial dissipation of pore pressures and radial displacements in the soil. Thus, the vertical displacement should be zero, $w_z=0$, and $\partial u/\partial z=0$ along the upper (CD) and lower (AB) boundary.
- Symmetry along the pile shaft requires that the horizontal displacement should be zero, $w_r=0$, and $\partial u/\partial r=0$ along the left boundary (AD), which represent the interface between the soil and the pile wall.
- On the far radial boundary (BC), the excess pore pressures $\Delta u=0$ and $\sigma'_r=\sigma'_{ho}$ corresponding to the in situ K_0 conditions prior to penetration.

In non-linear problems, it is possible that the solution procedure may not converge with the default convergence criteria or may use an excessive number of increments and iterations. Thus, it is quite common to use less stringent tolerance to achieve

convergence. This approach has been recommended in the past by Hashash (1992) for MIT-E3 finite element analyses using ABAQUS.

This section presents a brief synopsis of the two (2) solution control parameters modified to achieve convergence in a typical one-dimensional, non-linear, coupled consolidation analysis using MIT-S1. These parameters are the following:

1. The force residual control, R_n^a, is the ratio of the largest residual, r^a_{max}, to the corresponding average force, q^a. Most non-linear engineering calculations will be sufficiently accurate if the error in the residuals is less than 0.5%. Therefore ABAQUS normally uses:

$$r^a_{\max} \le R^a_n q;\ R^a_n = 0.005 \tag{5.10}$$

2. The displacement correction control, C_n^α is the ratio of the largest displacement correction, c^a_{max}, to the largest corresponding incremental displacement, Δu^a_{max}. For this control parameter ABAQUS uses:

$$c^a_{\max} \le C^a_n \Delta u^a_{\max};\ C^a_n = 0.01 \tag{5.11}$$

The preceding parameters are modified accordingly at each step of the following consolidation analyses based on successive iterations, until a converged state is achieved. The solution control parameters along with the iterations needed per step are reported separately at each one of the succeeding analyses.

5.3 MIT-S1 IMPLEMENTATION IN ABAQUS

This section outlines the explicit integration method used for the MIT-S1 model in the ABAQUS finite element code. A similar algorithm was used previously for the MIT-

E3 model (Hashash, 1992). In order to achieve accurate, stable solutions, the algorithm should used in conjunction with the following:

- Sub-stepping (sub-incrementation).

  The explicit integration scheme only converges to the 'exact' solution for $\Delta\varepsilon/\Delta T \rightarrow \dot{\varepsilon}$. However, numerical accuracy can be evaluated by comparing the response (stress path) for integration over n substeps, $d\varepsilon$, where $\Delta\varepsilon = nd\varepsilon$ (e.g. Hermann et al., 1987; Faruque & Desai, 1985) Thus, for a given soil model, the user can estimate the maximum allowable size $|d\varepsilon|^{15}_{max}$ to achieve numerically accurate solution (i.e. within prescribed tolerance). However, experience reported in the literature shows that there is no general prescriptive method for estimating $|d\varepsilon|_{max}$ a priori.

- Drift Correction.

  If the plastic consistency is not imposed in the integration algorithm, the stress point tends to 'drift' away from the yield surface, even for small (sub-stepping) strain increments, $|d\varepsilon| < |d\varepsilon|_{max}$. To avoid accumulating errors, a shortest path return-to-surface correction is applied after each sub-step to ensure that the stress point always remains in contact with the bounding surface.

Figure 5.3 shows the flow chart of the computational procedure used in explicit (Euler) integration of the MIT-S1 model. In order to achieve numerically accurate solutions, the maximum sub-step size is set to be $d\varepsilon_{max}=0.001\%$. A return drift correction is applied at the end of each sub-step to ensure that plastic consistency is satisfied.

[15] $|d\varepsilon|$ is a norm of the tensor

Appendix B contains a complete listing of the subroutine responsible for the integration of MIT-S1 in ABAQUS.

5.3.1 Intersection with Bounding Surface

Plastic behavior of soil elements which are consolidated along radial effective stress paths ($\tilde{\eta}=\frac{\tilde{s}}{\sigma'}$=constant) in MIT-S1, is described by a yield/bounding surface which is initially oriented along the direction of consolidation. The MIT-S1 model introduces a bounding surface (yield surface for normally consolidated specimens) which has the form of a distorted lemniscate surface, as shown in *Figure 5.4* (in triaxial stress space):

$$f = p'^2\left[(\mathbf{n}-\mathbf{b}):(\mathbf{n}-\mathbf{b})-\zeta^2\left(1-\left(\frac{p'}{\alpha'}\right)^m\right)\right]=0 \qquad (5.12)$$

$$\zeta^2 = c^2+\mathbf{b}:\mathbf{b}-2\mathbf{n}:\mathbf{b}$$

where, p' is the mean effective stress, **n** is the current stress ratio tensor, α is the size of the bounding surface, **b** is the orientation tensor for the bounding surface, c controls the aperture of the surface for p'→0 and the constant m describes the shape (slenderness) of the yield surface.

One of the most important corrective procedures in integration is the method used to determine the intersection point when the current stress point crosses the bounding surface. The algorithm used for this procedure is based on the Intermediate Value Theorem and is called Bisection Method (Burden & Faires, 1985).

Figure 5.5 illustrates the flow chart of the subroutine used to locate the intersection point according to the Bisection Method by considering stress states a and b at t_n and t_{n+1} respectively. At each step the method divides the interval in two by computing the

midpoint, m=(a+b)/2 and the value of the bounding surface f(m) at that point. Unless m is itself a root (which is very unlikely, but possible) there are now two possibilities: i) f(a) and f(m) have opposite signs and bracket a root; or ii) f(m) and f(b) have opposite signs and bracket a root. The method selects the subinterval that is a bracket as a new interval to be used in the next step. In this way the interval that contains the root of f is reduced in width by 50% at each step. The process is continued until the absolute value of f(m) is below a specified tolerance (in this case TOL=10^{-5}).

The Bisection Method, though conceptually clear, is relatively slow to converge, since the number of iterations can become quite large before $|f_m| \leq TOL$. However the significant feature of this method is that always converges to a solution and for that reason is used compared to more sophisticated and time-efficient numerical methods.

Figure 5.6 shows a numerical experiment which demonstrates the accuracy, stability and convergence properties of the Bisection Method as integrated in MIT-S1 model. More specifically at this case, the stress point crosses the bounding surface and thus the intersection subroutine is activated to restore the stress point on the bounding surface.

5.3.2 Model Input Parameters

Table 3.2 summarizes the input parameters used by the MIT-S1 model together with their physical significance and proposed laboratory tests from which these properties can be determined (Pestana, 1994). In addition to these material constants, the MIT-S1 model uses the following state variables:

- The effective stress tensor (σ', **S**)
- The size and orientation of the bounding surface (α', **b**)

- Effective stresses at the most recent reversal state (σ'_{rev}, S_{rev})
- The strains accumulated since the last reversal state (Δl_{ε}, Δl_{E})
- The size of the bounding surface at the last reversal state, α'_{rev}; and the size of the load surface at first yield, α'_{oi}

Initial values of these state variables must be implemented in ABAQUS at the start of an analysis. *Appendix B* presents a typical layout of the input file used to specify these parameters.

5.4 MIT-S1 PREDICTIONS

This section presents one-dimensional solutions for non-linear, coupled consolidation around a driven pile following penetration in K_0-consolidated BBC. More specifically, the effects of: i) installation analysis (CEM, SPM); and ii) constitutive model (MIT-E3, MIT-S1) on consolidation predictions will be investigated subsequently.

5.4.1 The effects of installation analysis

The installation stress and pore pressure fields obtained using SPM analyses are more realistic than those obtained by CEM analyses. For completeness, *Figures 5.7a and 5.8a* present predictions of the radial consolidation behavior of a soil element adjacent to the pile shaft according to the cylindrical Cavity Expansion (CEM) and Strain Path (SPM) method respectively. The results show the variation of excess pore pressures, $(u-u_o)$ and effective radial stress, σ'_r all normalized with respect to the initial vertical effective stress, σ'_{vo}, with time as expressed using the dimensionless time factor, T:

- The consolidation behavior is qualitatively similar regardless the method used for the initial stress and pore pressure fields. This behavior involves a monotonic increase in radial effective stress, while the excess pore pressure decreases with T. Similar behavior suggests that the mechanism of consolidation is not controlled by the method of analyzing pile installation. On the contrary, the mechanism of consolidation is, in fact controlled primarily by the constitutive model used in the analysis.
- The rate of pore pressure dissipation for CEM conditions is more rapid than for SPM conditions especially at early times during consolidation. This is mainly due to the differences in the shape of the pore pressure fields during installation (*Figure 4.12*).
- Complete dissipation of excess pore pressures occurs for $T \simeq 10$ based on SPM predictions. In contrast, CEM predictions require further time for pore pressures to dissipate completely, since $(u-u_o)/\sigma'_{vo} \neq 0$ for $T=10$.

Figures 5.7b and 5.8b show the fields of effective stresses, σ'_r/σ'_{vo}, σ'_v/σ'_{vo}, $\sigma'_\theta/\sigma'_{vo}$ predicted at the end of consolidation for each installation analysis.

- Adjacent to the pile shaft, for both installation analyses, the radial effective stress, σ'_r/σ'_{vo}, is the major principal effective stress while the vertical stress, σ'_v/σ'_{vo}, and tangential stress, $\sigma'_\theta/\sigma'_{vo}$, are the intermediate and minor principal effective stresses, respectively.
- In the region $7 \leq r_o/R \leq 45$, numerical oscillations occur at the field of effective stresses for both installation analyses. These numerical oscillations seem to affect

mainly the vertical stresses, σ'_v/σ'_{vo}, with less impact on the radial effective stresses, σ'_r/σ'_{vo}.

- In the far field, the vertical effective stresses $\sigma'_v/\sigma'_{vo} \simeq 1.0$ based on the SPM predictions corresponding to the in situ K_0 conditions prior to consolidation. On the other hand, CEM predictions do not simulate efficiently the far field conditions, since $\sigma'_v/\sigma'_{vo} < 1.0$. This behavior is linked to the incomplete dissipation of pore pressures, $(u-u_o)/\sigma'_{vo}$, observed in *Figure 5.7a*.

The numerical oscillations that occur in the region $7 \leq r_o/R \leq 45$ are primarily the outcome of the convergence tolerance relaxation at the last steps of consolidation. *Figure 5.9* shows graphically the convergence characteristics for both CEM and SPM analyses with respect to the number of steps and the dimensionless time factor, T. Based on this figure the default convergence criteria were insufficient for the solution to converge at the last steps, i.e. Steps 7 and 8 and thus the control parameters were increased. More specifically, the force residual control, R_n^a is increased by a factor of 18 in the case of the SPM analysis, while the displacement correction control, C_n^α is increased by a factor of 20 in the case of the CEM analysis. The relaxation of the control parameters explains to a certain degree the numerical instabilities but not the specific region that they affect consistently.

Further interpretation of the soil behavior after consolidation is given in *Figure 5.10*, which shows the volumetric behavior (i.e. mean effective stress, σ'/σ'_{max}, and volumetric strain, $\Delta\varepsilon_{vol}$) for two radial distances (i.e. $r_o/R=1$, 9) using both installation analyses (CEM,SPM) along with the K_0-Virgin Consolidation Line (K_0-VCL) predicted for the undisturbed clay (using MIT-S1). The initial stress states in these figures correspond to

the conditions predicted at the end of pile installation. It can be seen that both installation analyses follow the same trend, which justifies previous conclusion that the controlling mechanism of consolidation is the constitutive model used in the analysis. For both radial distances, $r_o/R=1$, 9, effective stress paths exhibit an initial decrease in shear stress level during installation, followed by a gradual return towards the K_0-VCL during consolidation. In any case, the final state (end of set-up) corresponds to a net reduction in mean effective stress and void ratio. This behavior reflects the intense shearing of the soil during pile installation which completely alters the anisotropic structure of the material.

Regarding the numerical oscillations, the previous analyses at radial distance $r_o/R=9$ do not provide an additional insight to the problem located in the region $7 \leq r_o/R \leq 45$. Therefore, further investigation is required establishing that these oscillations are not derived from any modeling parameters, such as: i) boundaries; and ii) mesh. These parameters are investigated thoroughly in the following sections, presenting only SPM predictions.

5.4.1.1. Effect of boundaries

The predictions notably for CEM in *Figure 5.7b* indicate that the far radial boundary (BC) affects the far field predictions, since $\sigma'_v/\sigma'_{vo}<1.0$ at $r_o/R \rightarrow 150$. Thus, it is well justified to investigate effect of the location of the far field radial boundary (BC). Three trial analyses have been performed with the boundaries located at $r_o/R=60$, 150 and 300.

Figure 5.11 shows in detail these three (3) finite element meshes used for solving the one-dimensional, non-linear, coupled consolidation around the shaft of a pile along with

the selected boundary conditions. The analyses use eight node isoparametric elements with pore pressure degrees of freedom at the corner nodes.

The primary parameter of interest in *Figure 5.12b* is the distribution of effective stress components (σ'_r/σ'_{vo}, σ'_v/σ'_{vo}, $\sigma'_\theta/\sigma'_{vo}$) at the end of consolidation for the radial region of $7 \leq r_o/R \leq 45$. For informational purposes, *Figure 5.12a* shows excess pore pressures, $(u-u_o)/\sigma'_{vo}$, and radial effective stresses, σ'_r/σ'_{vo}, at selected time factors, T, during intermediate stages of consolidation. The following remarks can be made:

- Adjacent to the pile shaft, the predictions of the normalized stresses either with time (T) or with radial distance (r_o/R) seem not to be affected by the location of far radial boundary (BC).
- In the region $7 \leq r_o/R \leq 45$, numerical oscillations occur in the field of effective stresses for each finite element mesh. Moreover, no specific pattern is recognized at the way these oscillations distribute through space.
- In the far field, the finite element extending to a radial distance 150 times the pile radius ($r_o/R=150$), appears to capture the soil behavior sufficiently. Thus, no further extension of the far field boundary is needed.

5.4.1.2. Effect of mesh

Reviewing the effect of the far field boundary to the numerical instabilities, the finite element mesh is investigated thoroughly thereafter. *Figure 5.13* exhibits the geometry of the two finite element meshes used to produce one-dimensional solutions for non-linear, coupled consolidation around a driven pile. The second mesh introduced in this section, consists of 99 elements and 498 nodes extending to a radial distance 150 times the pile

radius (r_o/R=150). Both analyses share the same boundary conditions and elements as described above.

The principal objectives of this study are: i) examining the adequacy of the mesh density close to the pile; and ii) eliminating the numerical oscillations throughout the problematic region. Following the same format, *Figures 5.14a and 5.14b* display excess pore pressures, $(u-u_o)/\sigma'_{vo}$, and radial effective stresses, σ'_r/σ'_{vo}, at selected times at the pile shaft and selected stress components (σ'_r/σ'_{vo}, σ'_v/σ'_{vo}, $\sigma'_\theta/\sigma'_{vo}$) at the end of consolidation throughout the entire radial range. These predictions suggest the following:

- Adjacent to the pile shaft, similar predictions are achieved using both mesh geometries. Thus the original finite element mesh captures adequately the problem in this region and no further refinement is needed.
- In the region $7 \leq r_o/R \leq 45$, the numerical instabilities deteriorate by refining the mesh geometry. In general, it can be observed that the instabilities tend to follow the frequency of the integration points, which is quite common to unstable solutions.
- In the far field, no particular effect is witnessed related to the density of the mesh.

Having analyzed all the obvious modeling parameters that can cause the numerical noise, it is reasonable to assume that the problem may be linked to the implementation of MIT-S1 in ABAQUS. However, reliable conclusions can be drawn at the regions close to the pile (i.e. $r_o/R<7$) and in the far field ($r_o/R>45$), since these are unaffected in each scenario.

5.5 COMPARISON WITH MIT-E3 PREDICTIONS

In order to assess the role of the MIT-S1 soil model in the predictions of consolidation behavior, results of consolidation analyses performed by means of the MIT-S1 model are compared with MIT-E3 predictions (Whittle, 1987). Initial conditions from pile installation are based on the SPM analysis.

Figures 5.15a and 5.15b display excess pore pressures, $(u-u_o)/\sigma'_{vo}$, and radial effective stresses, σ'_r/σ'_{vo}, at selected times at the pile shaft and selected stress components (σ'_r/σ'_{vo}, σ'_v/σ'_{vo}, $\sigma'_\theta/\sigma'_{vo}$) at the end of consolidation for the complete radial range. From these results, it is difficult to separate the effects of constitutive models on consolidation behavior from their effects on pile installation. However, the following observations may be made:

- The MIT-E3 and MIT-S1 models give generally different predictions of effective stresses at the pile shaft (i.e. $r_o/R<7$) at the end of consolidation.
- Comparing qualitatively the predictions of the effective stress components not only in the far field ($r_o/R>45$) but also in the problematic region ($7\leq r_o/R\leq 45$), both models give generally similar results. Thus, it is safe to assume that MIT-S1 predictions can simulate the soil behavior even at this radial range.
- The MIT-E3 model predicts more rapid pore pressure dissipation than the MIT-S1 model. This behavior is a reflection of differences in the pore pressure fields predicted during installation. Following the same logic, the increase rate of radial effective stresses, σ'_r/σ'_{vo}, is different for the two soil models.

Figure 5.16 compares the effective stress paths and volumetric behavior of soil elements adjacent to the pile shaft based on MIT-E3 (Whittle, 1993) and MIT-S1 results. The K_0-Virgin Consolidation Line (K_0-VCL) is estimated for the undisturbed clay using MIT-S1. Both soil models generate large shear induced pore pressures (reductions in σ') during pile installation associated with severe shearing of the soil at constant water content. During re-consolidation MIT-S1 predicts much stiffer response with smaller volumetric strains than MIT-E3.

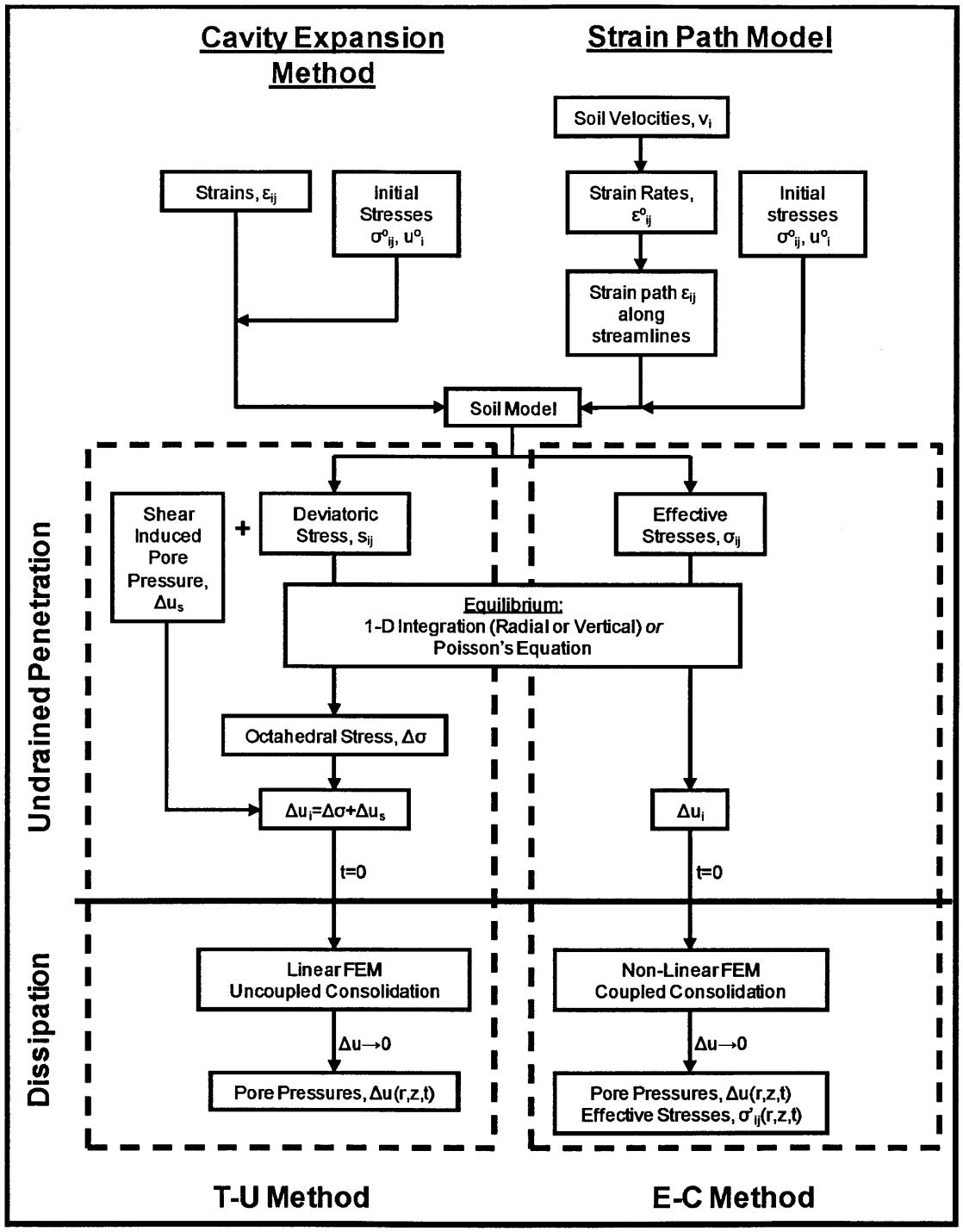

Figure 5.1: Overview of the method of analysis used to compute stress, strain and pore pressure during penetration and dissipation of driven piles

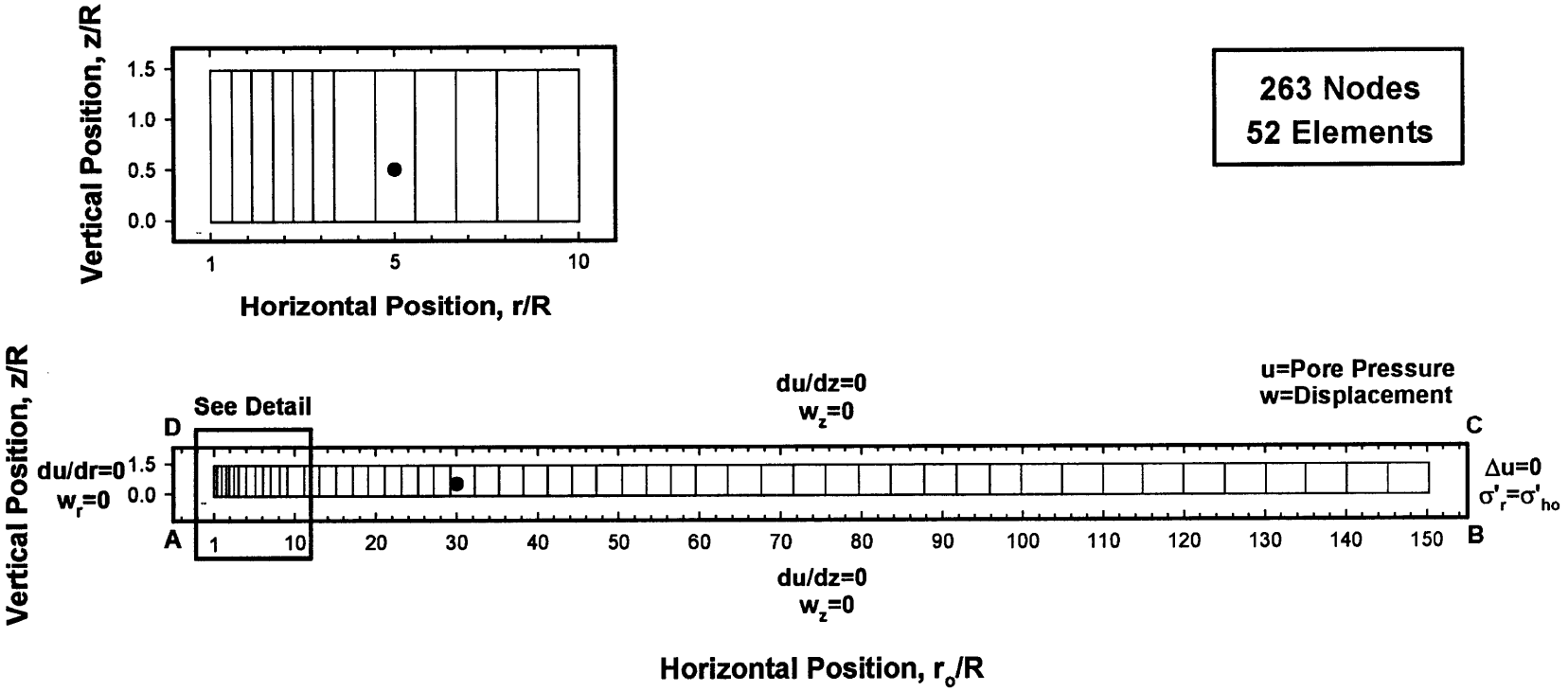

Figure 5.2: Boundary conditions and typical finite element mesh for one-dimensional, non-linear, coupled consolidation around a driven pile

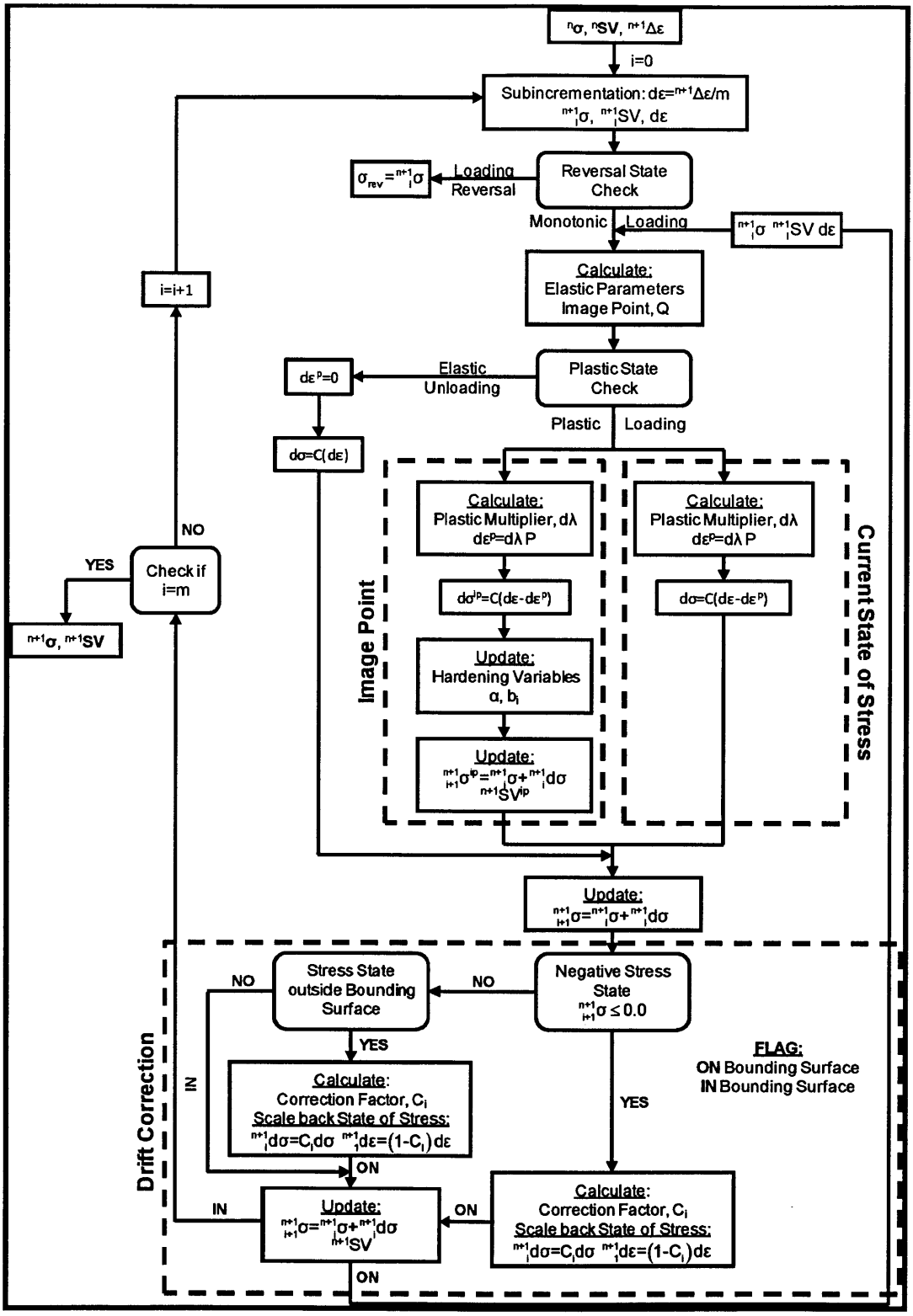

Figure 5.3: Flow chart of MIT-S1 explicit integration algorithm

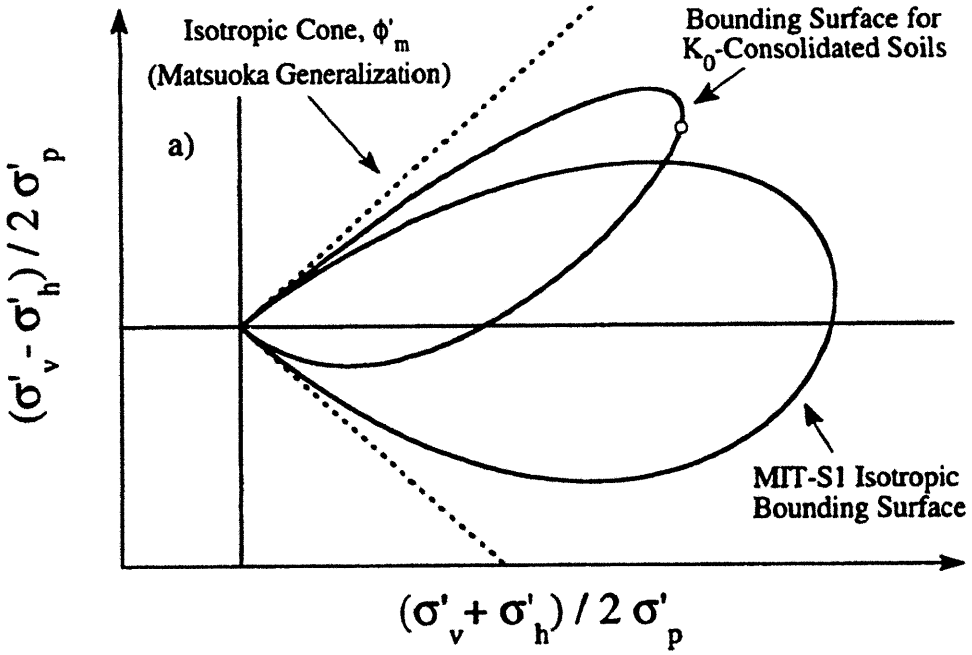

Figure 5.4: Anisotropic and isotropic bounding surfaces in MIT-S1 (Pestana, 1994)

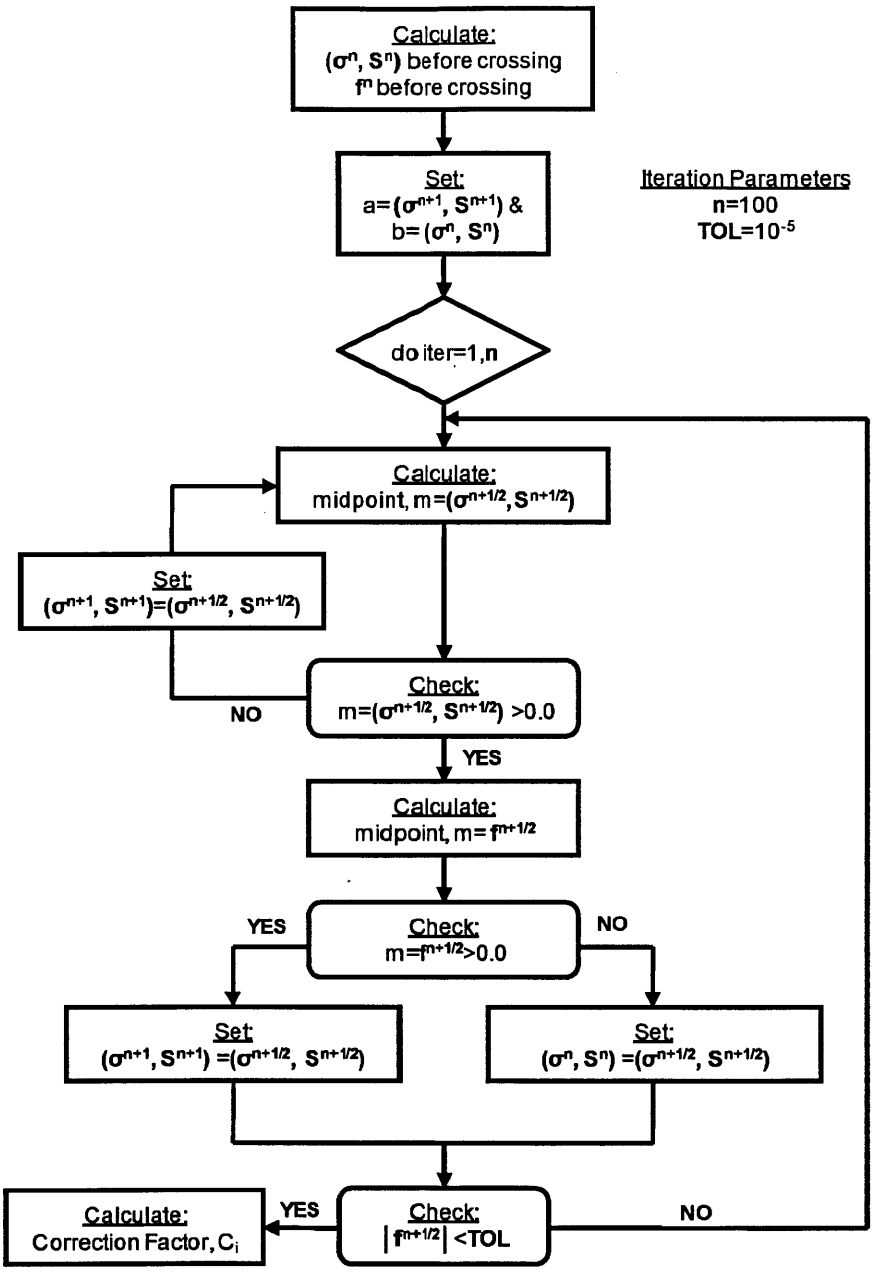

Figure 5.5: Flow chart of intersection subroutine

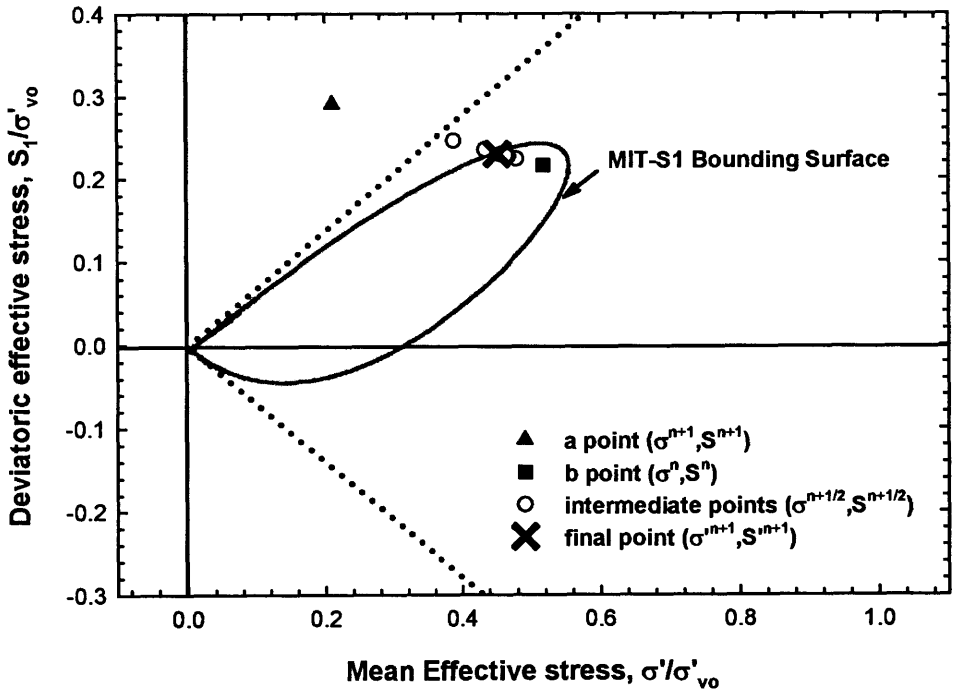

Figure 5.6: Numerical example of intersection subroutine (n=14 iterations)

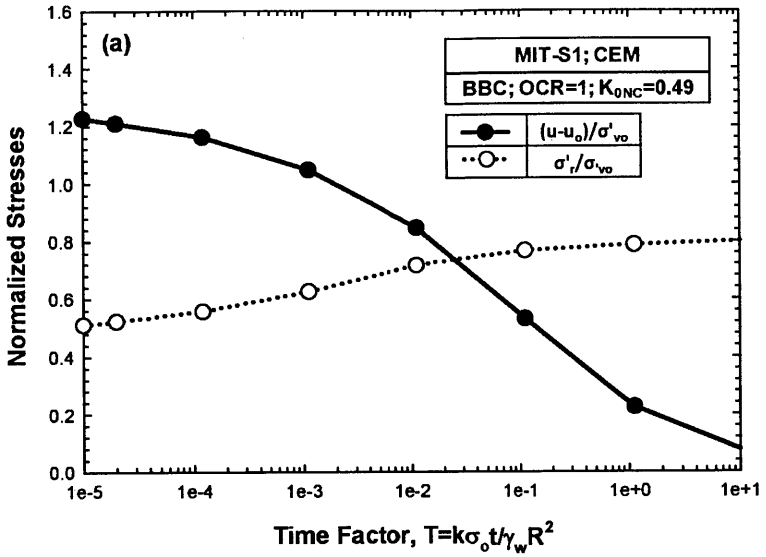

Figure 5.7a: Set-up behavior at pile shaft

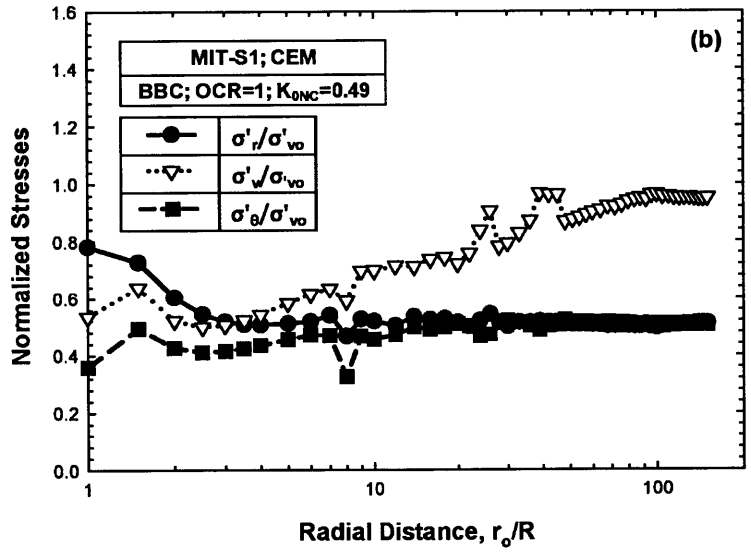

Step	Time Factor	Iteration	Force Residual, R_n^α	Displacement Correction, C_n^α
1	0.00001	2	0.005	0.01
2	0.0001	3	0.005	0.01
3	0.001	6	0.005	0.01
4	0.01	4	0.005	0.01
5	0.1	6	0.005	0.01
6	1	5	0.02	0.1
7	10	9	0.01	0.2

Figure 5.7b: Distribution of effective stress at the end of set-up

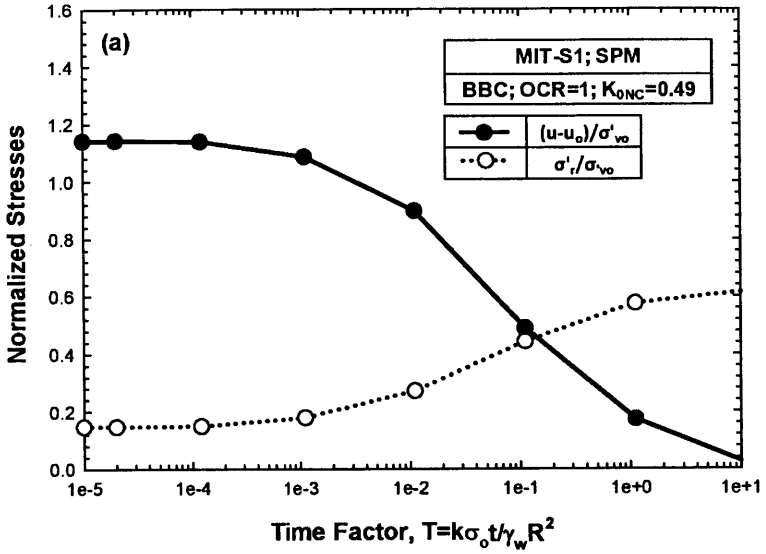

Figure 5.8a: Set-up behavior at pile shaft

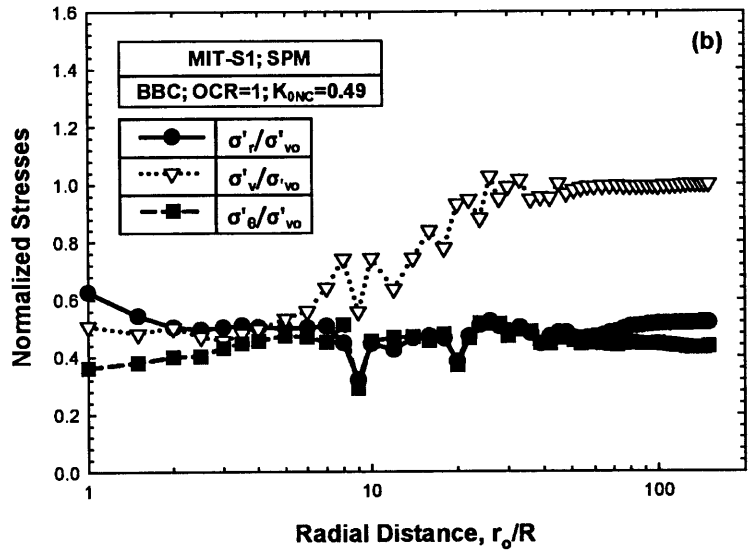

Step	Time Factor	Iteration	Force Residual, R_n^α	Displacement Correction, C_n^α
1	0.00001	2	0.005	0.01
2	0.0001	3	0.005	0.01
3	0.001	3	0.005	0.01
4	0.01	3	0.005	0.01
5	0.1	18	0.005	0.01
6	1	5	0.04	0.11
7	10	9	0.09	0.14

Figure 5.8b: Distribution of effective stress at the end of set-up

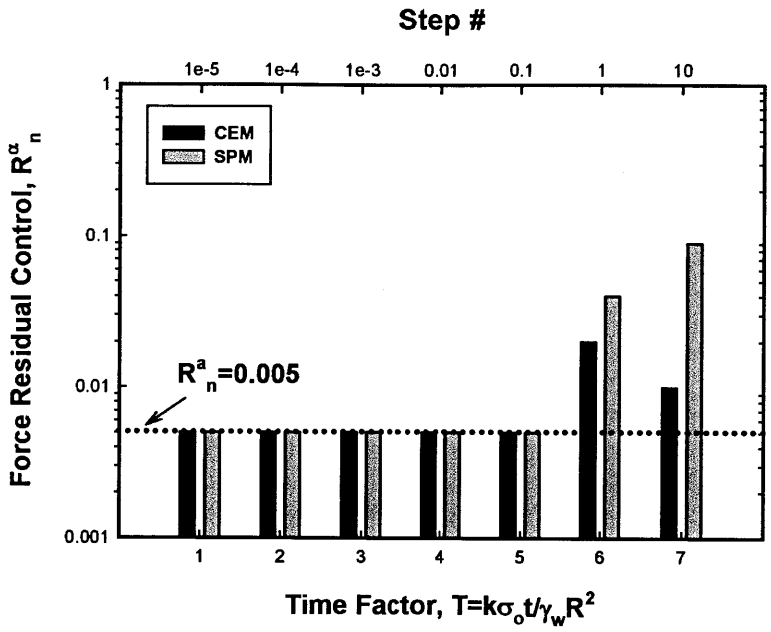

Figure 5.9a: Force residual control R_n^a during pile set-up

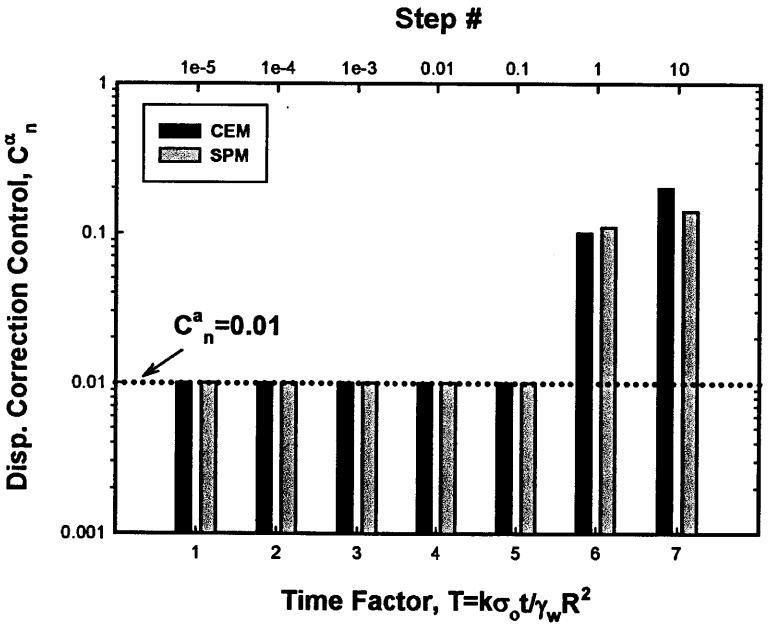

Figure 5.9b: Displacement correction control C_n^{α} during pile set-up

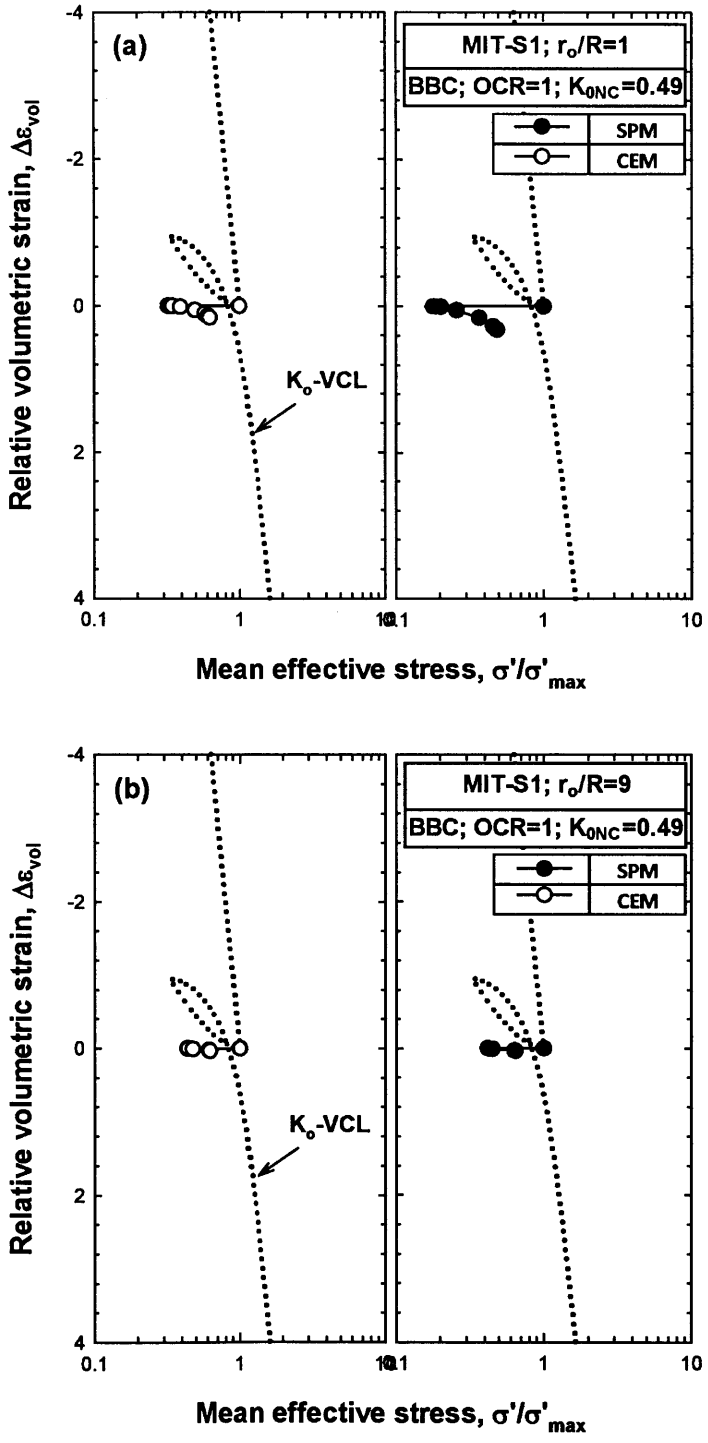

Figure 5.10: Predicted volumetric behavior of soils elements using CEM and SPM at: i)r_o/R=1; and ii) r_o/R=9

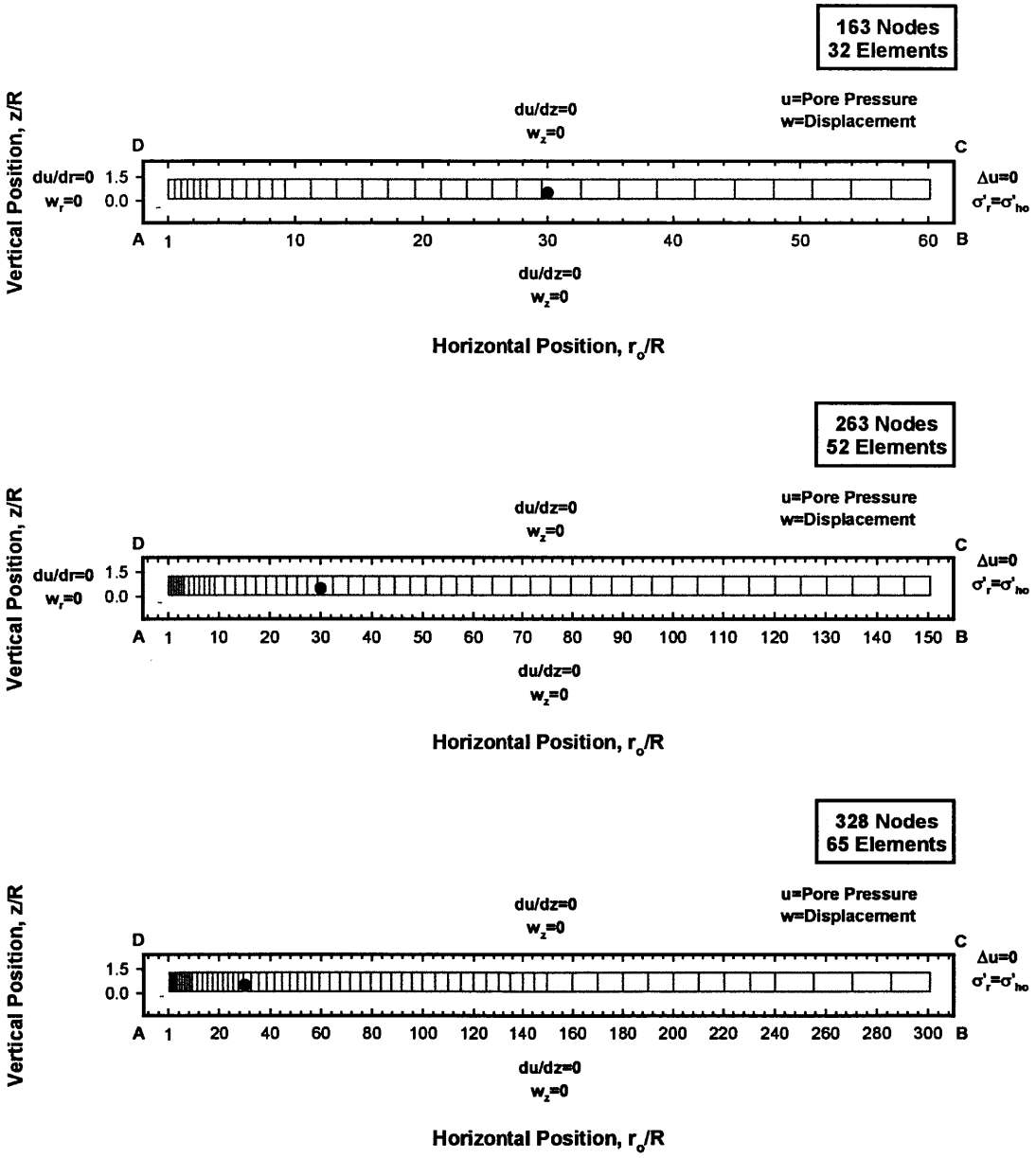

Figure 5.11: Three mesh geometries for one-dimensional, non-linear, coupled consolidation around a driven pile extending to a radial distance r_o/R=60, 150 and 300

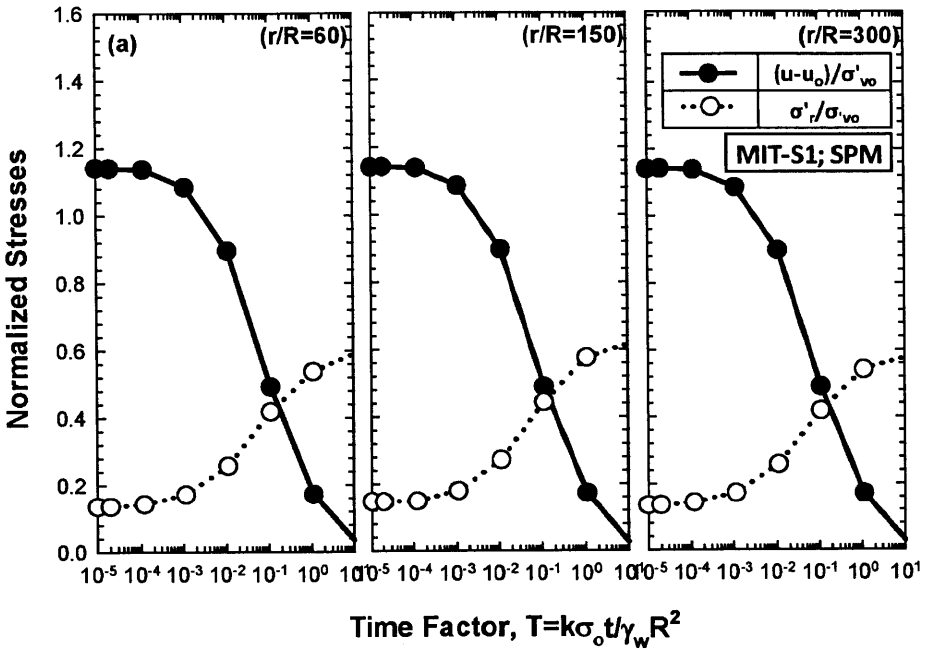

Figure 5.12a: Effect of boundary conditions on set-up at shaft

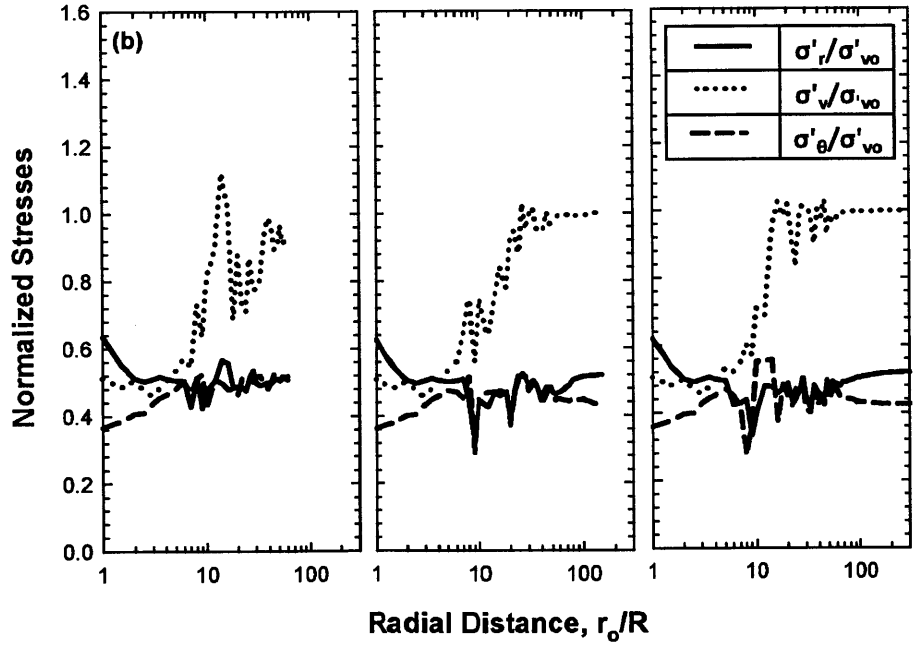

Figure 5.12b: Effect of boundary conditions on distribution of effective stress at the end of set-up

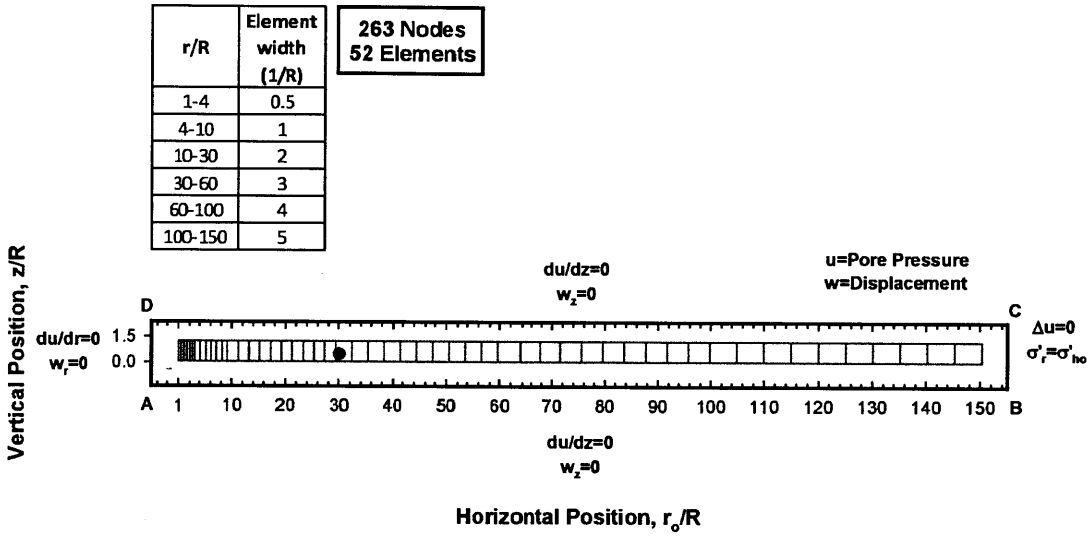

Figure 5.13a: Coarse finite element mesh for one-dimensional, non-linear, coupled consolidation around a driven pile

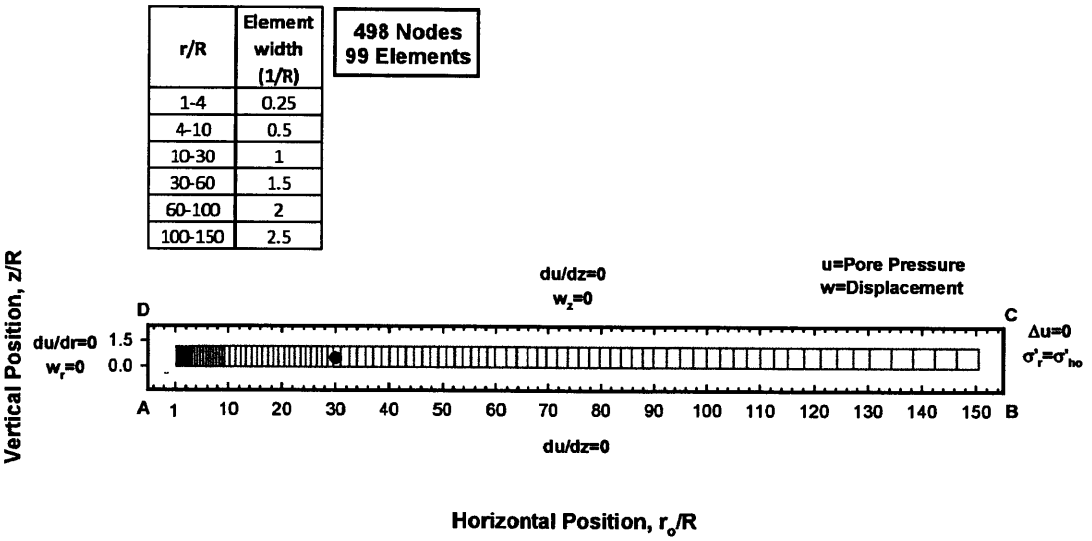

Figure 5.13b: Dense finite element mesh for one-dimensional, non-linear, coupled consolidation around a driven pile

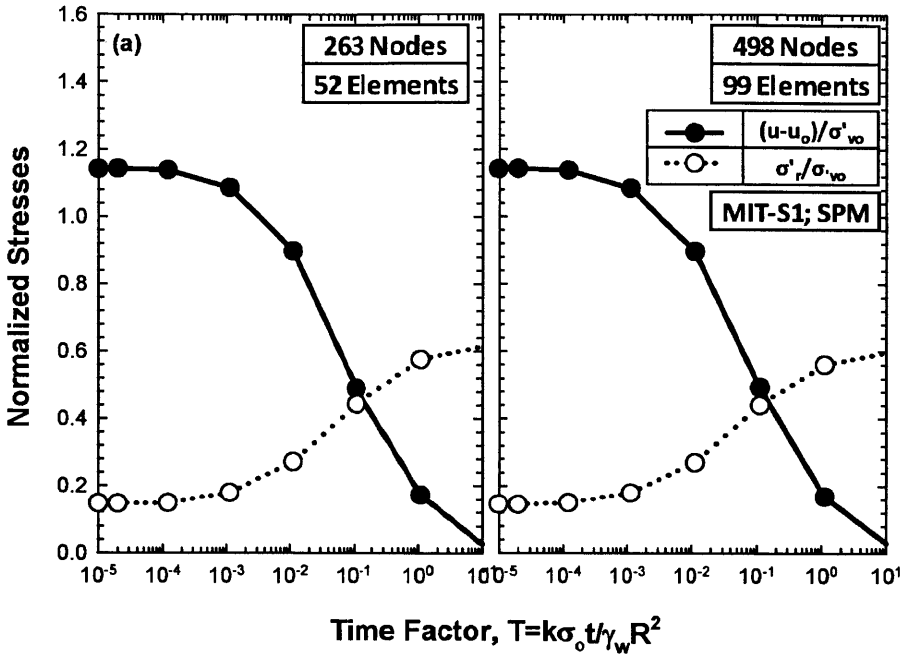

Figure 5.14a: Effect of mesh on set-up at shaft

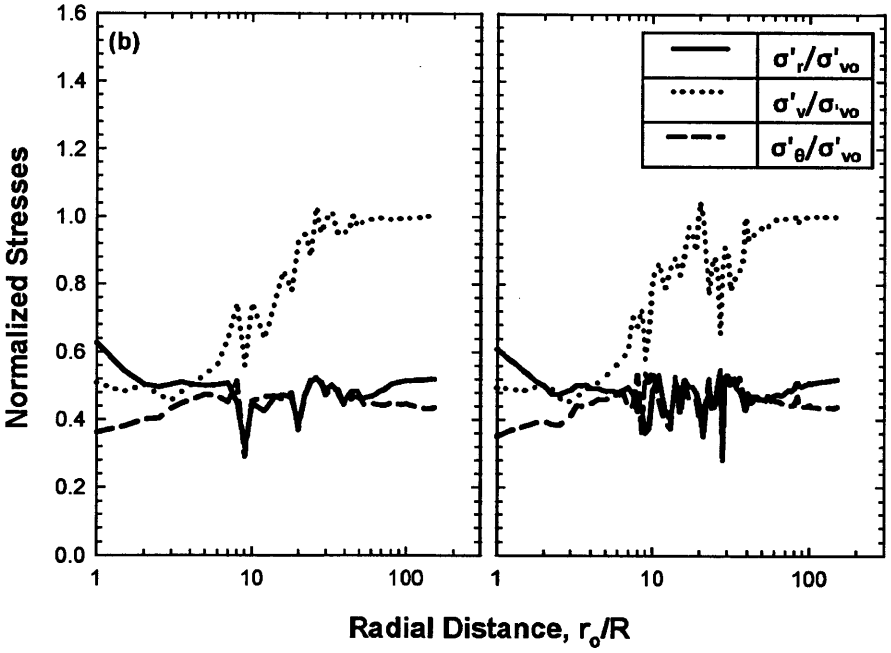

Figure 5.14b: Effect of mesh on distribution of effective stress at the end of set-up

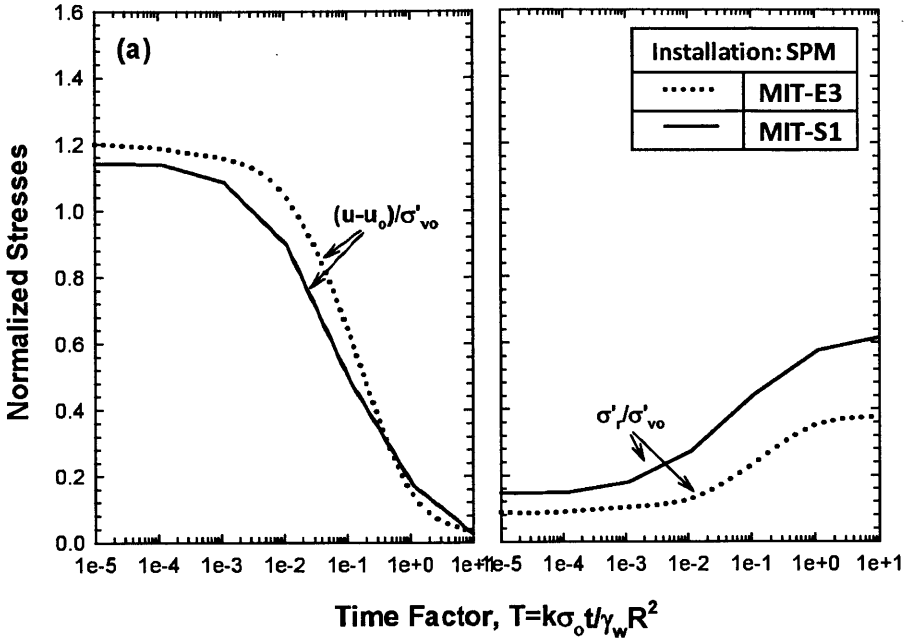

Figure 5.15a: Effect of soil model on set-up at shaft

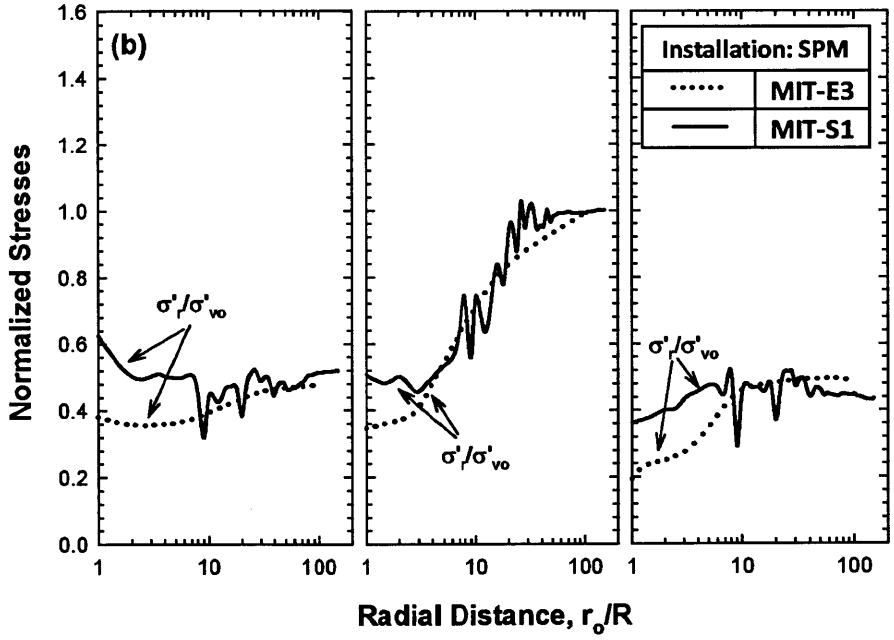

Figure 5.15b: Effect of soil model on distribution of effective stress at the end of set-up

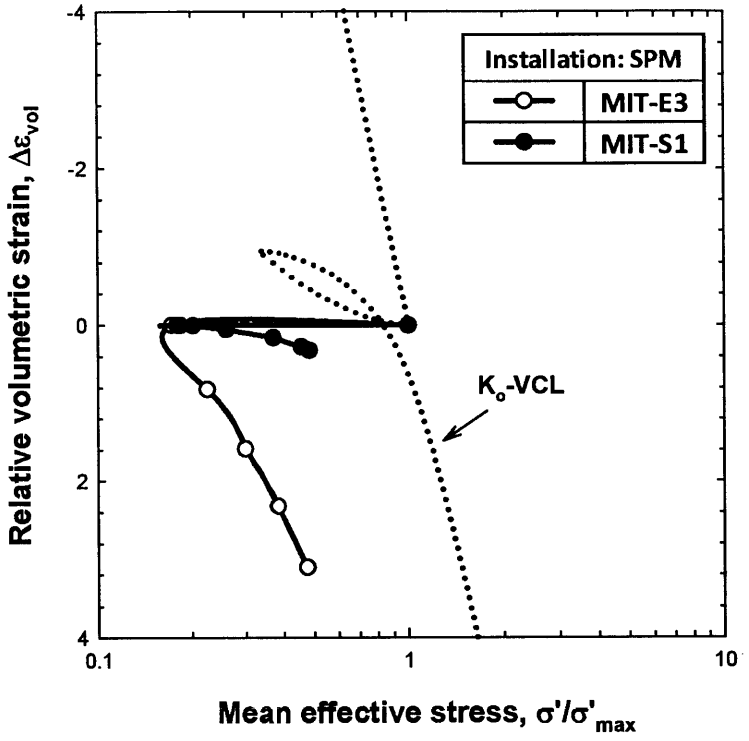

Figure 5.16: Predicted volumetric behavior of soils elements using SPM adjacent to the pile shaft

6. SUMMARY AND CONCLUSIONS

This research represents an effort to develop a better understanding of the mechanisms governing the development of axial capacity of piles driven in overconsolidated clays. A rational approach for analyzing the performance of friction piles in clays is made by estimating the changes in effective stresses and pore pressures caused by: i) pile installation; and ii) consolidation around the pile shaft. These predictions depend mainly on the method used to simulate pile installation but also the model used to describe the mechanical behavior of the clay. The following sections summarize the principal conclusions and findings reached in this study.

6.1 PILE INSTALLATION

The effective stresses and pore pressures caused by steady state pile installation are predicted using the MIT-S1 model in combination with the Strain Path (SPM) and the cylindrical Cavity Expansion (CEM) methods of analysis in normally to highly overconsolidated clays (OCR=1.0, 2.0, 4.0, 8.0 and 16.0). Trying to assess the parameters affecting the mechanics of pile installation, the effect of: i) method of analysis; ii) soil model; and iii) stress history, are investigated thoroughly.

The results may be summarized as follows:

- For radial distances less than about 10R, there are significant differences in the stress fields predicted by SPM and CEM analyses at all OCR's. At the pile shaft,

cavity expansion analyses (CEM) always predict much larger values of σ'_r/σ'_{vo}, σ'/σ'_{vo} and $(\sigma'_r-\sigma'_\theta)/2\sigma'_{vo}$ than are found using the strain path method (SPM).

- Pile installation leads to the development of excess pore pressures, $(u-u_o)/\sigma'_{vo}$, extending to a distance 60 times the pile radius (r/R=60) based on SPM predictions. In contrast, CEM predictions produce excess pore pressures, $(u-u_o)/\sigma'_{vo}$, extending to distances greater than 60 times the pile radius (r/R>60).
- The pore pressures, $(u-u_o)/\sigma'_{vo}$, predicted at the pile shaft are between 25 to 55% higher for CEM analyses than for SPM analyses for all OCR's, except for the case of OCR=1.
- The zone of disturbance in terms of excess pore pressures (i.e. $(u-u_o)/\sigma'_{vo}$) around the pile generated by the MIT-S1 model is much larger compared to MIT-E3 predictions. This discrepancy between the two model predictions increases as the OCR increases.
- For lightly overconsolidated clays (OCR≤2) the maximum excess pore pressures, $(u-u_o)/\sigma'_{vo}$, appear around the face ($-0.5\leq z/R\leq 1.7$) of the pile according to MIT-S1 analyses. On the contrary, MIT-E3 predicts that maximum excess pore pressure appears at locations along the face of the pile above the tip ($1.0\leq z/R\leq 2.5$).
- The radial effective stresses, σ'_r/σ'_{vo}, and pore pressures, $(u-u_o)/\sigma'_{vo}$, induced at the pile shaft increase significantly with OCR.

The MIT-S1 model predictions of $(u-u_o)/\sigma'_{vo}$ using both installation analyses (SPM, CEM) may be evaluated by comparison with field/laboratory data from separate sites. The evaluations may be outlined as follows:

- For normally to lightly overconsolidated clays, the CEM analyses have a good agreement with the experimental data while the SPM tends to underestimate the measured pore pressure.
- Overall the SPM compared to CEM predictions seem to capture more accurately both the magnitude and the radial extend of the disturbance zone. Hence, CEM analyses incline to overestimate $(u-u_o)/\sigma'_{vo}$ at the shaft while underestimating pore pressures in the far field.

6.2 CONSOLIDATION

The predominant aims of the consolidation analyses are to estimate the net changes in effective stresses around the pile shaft as well as the rates of pore pressure dissipation and radial effective stress set-up (at the pile shaft). The final radial effective stress at the pile shaft, σ'_r/σ'_{vo}, is believed to be the most important prediction of the analysis as it controls the subsequent frictional behavior during axial loading. The rates of dissipation and set-up are particularly important to assess the time required for pile loads to be applied safely.

Predictions of the consolidation behavior are obtained using the MIT-S1 model in conjunction with the general purpose finite element code ABAQUS. The complexity of the model precludes the use of the efficient implicit integration scheme. Hence, the implementation of MIT-S1 is achieved using an explicit integration scheme, with correction for drift from the bounding surface, and local sub-incrementation. A numerical example is presented to demonstrate the accuracy and convergence characteristics of drift correction.

Predictions are produced for initial conditions corresponding to installation using CEM and SPM analyses and compare the effects of soil model (using the MIT-E3 model) for OCR=1. The main results may be summarized as follows:

- The logarithmic increase of the excess pore pressure in the region close to the cavity (i.e. $r_o/R<10$) leads to a more rapid rate of pore pressure dissipation for CEM conditions compared to SPM conditions.
- For soil elements adjacent to the pile shaft ($r_o/R<7$), at the end of consolidation, the MIT-S1 model predicts that σ'_r/σ'_{vo} is the major principal effective stress for both CEM and SPM installation analyses.
- At the region $7\leq r_o/R\leq 45$, numerical oscillations occur at the field of effective stresses for both installation analyses. Investigating all the modeling parameters (e.g. boundaries, mesh) possibly related to numerical instabilities, it is concluded that the problem may be linked to the implementation of MIT-S1 into ABAQUS and affects specifically this radial region.
- At the far field ($r_o/R\rightarrow 150$), the stress state corresponds to the in situ K_0 conditions prior to consolidation and thus the soil behavior is simulated efficiently at this region.
- In general, the MIT-E3 and MIT-S1 models give different predictions of effective stresses and particularly close to the pile shaft (i.e. $r_o/R<7$) at the end of consolidation. This discrepancy can be attributed to the observed differences in the installation stresses discussed above.

- For soil elements adjacent to the pile shaft ($r_o/R<7$), different soil behavior is predicted by the two soil models, with MIT-S1 revealing a stiffer behavior compared to MIT-E3 analysis.

REFERENCES

[1] Abu-Farkash, M., Voyiadjis, G.Z. & Turnay, M. (1997). "Numerical analysis of the miniature piezocone penetration tests (CPT) in cohesive soils" Int. Journal for Numerical and Analytical Methods in Geomechanics, 22, 197-808.

[2] Ahmed, I. (1990). "Investigation of normalized behavior of resedimented Boston Blue Clay using Geonor Direct Simple Shear Apparatus" SM Thesis, Massachusetts Institute of Technology, Cambridge, MA.

[3] Aubeny, C.P. (1992). "Rational interpretation of in situ tests in cohesive soils" Ph.D. Thesis, Massachusetts Institute of Technology, Cambridge, MA.

[4] Azzouz, A.S. & Lutz, D.G. (1986). "Shaft behavior of a model pile in plastic Empire clays" ASCE Journal of Geotechnical Engineering, 112, 389-406.

[5] Azzouz, A.S., Baligh, M.M. & Whittle, A.J. (1990). "Shaft resistance of friction piles in clay" ASCE Journal of Geotechnical Engineering, 116, 205-221.

[6] Baligh, M.M. & Levadoux, J.N. (1980). "Pore pressure dissipation after cone penetration" Research Report, R80-11, MIT Dept Civ Engrg, Cambridge, MA.

[7] Baligh, M.M. (1985). "Strain Path Method" ASCE Journal of Geotechnical Engineering, 111(9), 1108-1136.

[8] Baligh, M.M. (1986a). "Undrained deep penetration: I Shear Stresses" Geotechnique, 36, 471-485.

[9] Baligh, M.M. (1986b). "Undrained deep penetration: II Pore pressures" Geotechnique, 36, 487-501.

[10] Biot, M.A. (1935). "Le problem de la consolidation de matieres argileuses sous une charge" Anna;es de la Societe Scientifique de Bruxelles, 55, 110-113.

[11] Bogard, D., Matlock, H., Audibert, J.M.E. & Bamford, S.R. (1985). "Three years' experience with model pile segment tool tests" Proc. 17th Offshore Tech. Conf., Houston, Paper 4848.

[12] Bond, A.J. & Jardine, R.J. (1991). "Effects of installing displacement piles in a high OCR clay" Geotechnique, 41, 341-363.

[13] Bond, A.J., Jardine, R.J. & Dalton, C.P. (1991). "Design and performance of the Imperial College instrumented pile" ASTM Geotechnical Testing Journal, 14, 413-425.

[14] Burland, J. (1973). "Shaft friction of piles in clay - A simple fundamental approach" Proceedings, Ground Engineering, 6, 30-42.

[15] Cauble , D.F. (1993). "The behavior of resedimented Boston Blue Clay at OCR=4 in cyclic and post-cyclic undrained Direct Simple Shear" SM Thesis, Massachusetts Institute of Technology, Cambridge, MA.

[16] Chandler, R.J. (1968). "The shaft friction of piles in cohesive soils in terms of effective stress" Civil Engrg. And Public Works Review, 63, 48-51.

[17] Coop, M.R. (1987). "The axial capacity of driven piles in clay" PhD Thesis, Dept. of Engineering Science, University of Oxford.

[18] Coop, M.R. & Wroth, C.P. (1989). "Field studies of an instrumented model pile in clay" Géotechnique, 39, 679-696.

[19] Davis, E.H. & Poulos, H.G. (1970). "Discussion of 'An analysis of consolidation theories'" by. Schiffman, R.L., Chen, A.T.F. & Jordan, J.C., ASCE Journal of the Soil Mechanics and Foundations Division, 96, 334-336.

[20] Eide, O., Huthcinson, J.N. & Landva, A. (1961). "Short and long term test loading of a friction pile in clay" Proceedings of the 5th ICSMFE, Paris, France, 2, 45-53.

[21] Elsworth, D. (1991). "Dislocation analysis of penetration in saturated porous media" Journal of Engineering Mechanics, 117(2), 391-408.

[22] Elsworth, D. (1993). "Analysis of piezocone dissipation using dislocation methods" Journal of Geotechnical Engrg., 119(10), 1601-1623.

[23] Faruque, M.O. & Desai, C.S. (1985). "Implementation of a general constitutive model for geological material" Int. Journal for Numerical and Analytical Methods in Geomechanics, 9, 1099-1114.

[24] Fayad, P. (1986). "Aspects of the volumetric and undrained shear behavior of Boston Blue Clay" SM Thesis, Massachusetts Institute of Technology, Cambridge, MA.

[25] Flaate, K. (1968). "Baereevne av friksjonspeler i leire" om Beregnong av Baereevne pa qrunnlag av Geotekniske Undersokelser, Oslo Veglaboratoriet, Norway.

[26] Flaate, K. & Selnes, P. (1977). "Side friction of piles in clay" Proceedings of the 9th ICSMFE, Tokyo, Japan, 1, 517-522.

[27] Hashash, Y.M.A. (1992). "Analysis of deep excavations in clay" Ph.D. Thesis, Massachusetts Institute of Technology, Cambridge, MA.

[28] Hawkins, A.B., Larnach, W.J., Lloyd, I.M., & Nash, D.F.T. (1989). "Selecting the location, and initial investigation of the SERC soft clay test bed site" Quarterly Journal of Engineering Geology, 22, 281-316.

[29] Heydinger, A.G. & O'Neil M.W. (1986). "Analysis of axial pile-soil interaction in clay" Int. Journal for Numerical and Analytical Methods in Geomechanics, 10, 367-381.

[30] Herrmann, L.R., Kaliakin, V., Shen, C.K., Mish, K. & Zhu, Z.Y. (1987). "Numerical implementation of plasticity model for cohesive soils" ASCE J. Engrg. Mech., 113, 500-519.

[31] Hight, D.W., Bond, A.J., & Legge, J.D. (1992). "Characterisation of Bothkennar clay: an overview" Geotechnique, 42, 303-348.

[32] HKS (2007). "ABAQUS Version 6.7 User's Manual" Hibbit, Karlson and Sorenson, Inc., Providence, R.I.

[33] Jardine, R.J. (1985). "Investigations of pile-soil behavior, with special reference to the foundations of offshore structures" Ph.D. Thesis, Imperial College of Science, Technology and Medicine, London, UK.

[34] Karlsrud, K. & Haugen, T. (1985). "Axial static capacity of steel model piles in overconsolidated clay" Proc. 11th Intl. Conf. on Soil Mechs and Found. Engrg., San Francisco, 1401-1406

[35] Karlsrud, K., Borg Hansen, S., Dyvik, R. & Kalsnes, B. (1992). "NGI's pile tests at Tilbrook and Pentre - Review of testing procedures and results" Proc. ICE Conf. on Recent Large Scale Fully Instrumented Pile Tests in Clay, London.

[36] Kavvadas, M. (1982). "Non-linear consolidation around driven piles in clays" Ph.D. Thesis, Massachusetts Institute of Technology, Cambridge, MA.

[37] Ladd, C.C., Bovee, R., Edgers, L. & Rixner, J.J. (1971). "Consolidated-Undrained Plane Strain tests on Boston Blue Clay" Research Report, R71-13, MIT Dept Civ Engrg, Cambridge, MA

[38] Lehane, B.M. (1992). "Experimental investigations of pile behavior using instrumented field piles" Ph.D. Thesis, Imperial College of Science, Technology and Medicine, London, UK.

[39] Lehane, B.M. & Jardine R.J. (1994). "Displacement pile behavior in glacial clay" Canadian Geotechnical Journal, 31, 79-90.

[40] Lehane, B.M. & Jardine R.J. (1994). "Displacement-pile behavior in a soft marine clay" Canadian Geotechnical Journal, 31, 181-191.

[41] Levadoux, J.N. (1980). "Pore pressures in clays due to cone penetration" Ph.D. Thesis, Massachusetts Institute of Technology, Cambridge, MA.

[42] Levadoux, J.N. & Baligh, M.M. (1980). "Pore pressures during cone penetration in clays" Research Report, R80-15, MIT Dept Civ Engrg, Cambridge, MA.

[43] Lunne, T., Long, M. & Forsberg, C.F. (2003). "Characterization and engineering properties of Onsoy clay" Characterization and Engineering Properties of Natural Soils, Swets & Zeitlinger B.V., Lisse, The Netherlands.

[44] Marsland, A., & Powell, J.J.M. (1985). "Field and laboratory investigations of the clay tills at the Building Research Establishment test site at Cowden, Holderness" Proceedings of the International Conference on Construction in Glacial Tills and Boulder Clays, Edinburgh, Scotland, 147-168.

[45] May, R.E. (1987). "A study of the piezocone penetrometer in normally consolidated clay" PhD Thesis, Dept. of Engineering Science, University of Oxford.

[46] Meyerhof, G.G. (1976). "Bearing capacity and settlement of pile foundations" ASCE JGED, 102, 197-228.

[47] Morrison, M.J. (1984). "In situ measurements on a model pile in clay" Ph.D. Thesis, Massachusetts Institute of Technology, Cambridge, MA.

[48] Nyirenda, Z.M. (1989). "The piezocone in lightly overconsolidated clay" PhD Thesis, Dept. of Engineering Science, University of Oxford.

[49] O'Neil, D.A. (1985). "Undrained strength anisotropy of an overconsolidated thixotropic clay" SM. Thesis, Massachusetts Institute of Technology, Cambridge, MA.

[50] Ortega, O.J. (1992). "Computer automation of the consolidated undrained Direct Simple Shear test" SM. Thesis, Massachusetts Institute of Technology, Cambridge, MA.

[51] Peck, R.B. (1958). "A study of the comparative behavior of friction piles" Highway Research Board, Specialty Report 36.

[52] Pestana, J.M., (1994). "A unified constitutive model for clays and sands" ScD Thesis, Massachusetts Institute of Technology, Cambridge, MA.

[53] Ponniah, D.A. (1989). "Instrumentation of a jacked in pile" Proceedings of the Conference on Instrumentation in Geotechnical Engineering, British Institution of Civil Engineers, Nottingham, England, 207-220.

[54] Randolph, M.F. & Wroth C.P. (1979). "Driven piles in clay: Effects of installation and subsequent consolidation" Géotechnique, 29(4), 361-393.

[55] Randolph, M.F., Carter, J.P. & Wroth C.P. (1979). "Driven piles in clays: Effects of installation and subsequent consolidation" Int. Journal for Numerical and Analytical Methods for Geomechanics, 2, 217-229.

[56] Randolph, M. F. & Murphy, B. S. (1985). "Shaft capacity of driven piles in clay" Proc. 17th Ann. Offshore Technol. Conf., Houston, 1,371–378.

[57] Rendulic, L. (1936). "Porenziffer und poren passerdruck in tonen" Der Bauingenieur, 17, 559-564.

[58] Roy, M., Blanchet, R., Tavenas, F. & LaRochelle, P. (1981). "Behavior of a sensitive clay during pile driving" Canadian Geotechnical Journal, 18, 67-85.

[59] Seah, T.H. (1990). "Anisotropy of normally consolidated Boston Blue Clay" ScD Thesis, Massachusetts Institute of Technology, Cambridge, MA.

[60] Sheahan, T.C. (1991). "An experimental study of the time-dependent undrained shear behavior of resedimented clay using automated stress path triaxial equipment" ScD Thesis, Massachusetts Institute of Technology, Cambridge, MA.

[61] Sills, G.C. (1975). "Some conditions under which Biot's Equations of consolidation reduce to Terzaghi's equation", Geotechnique, 25, 129-132.

[62] Smith, P.R., Jardine, R.J., & Hight, D.W. (1992). "The yielding of Bothkennar clay" Geotechnique, 42, 257-274.

[63] Soderberg, L.O. (1962). "Consolidation theory applied to foundation pile time effects" Géotechnique, 12, 217-232.

[64] Sutabutr, T. (1999). "Analyses and interpretation of tapered piezoprobe and application to offshore pile design" ScD Thesis, Massachusetts Institute of Technology, Cambridge, MA.

[65] Teh, C.I. (1987). "An analytical investigation of the cone penetration test" Ph.D. Thesis, University of Oxford.

[66] Teh, C.I. & Houlsby, G.T. (1991). "An analytical study of the cone penetration test in clay" Géotechnique, London, U.K. 41(1), 17-34.

[67] Terzaghi, K. (1936). "Die Berechnung der durchlassigheitsziffer des tones aus dem verlaug der hydrodynamischen spannungserheinungen" Akademie der Wissenchaften in Win, Sitzungsberichte Mathematish Naturwissenschaftliche Klass, Part IIa, 132, 125-138.

[68] Terzaghi, K. & Peck, R.B. (1967). "Soil mechanics in engineering practice" John Wiley and Sons, New York.

[69] Tomlinson, M.J. (1971). "Some effects of pile driving on skin friction" Proceedings of the Conference on Behavior of Piles, London, 107-114.

[70] Van den Berg (1992). "Numerical model for cone penetration" Computer methods and Advances in Geomechanics, Ed. Booker & Carter, Balkema, Rotterdam, 1777-1782.

[71] Van den Berg (1994). "Analysis of soil penetration" Delft University Press, Delft, The Netherlands.

[72] Varney, A. (1998). "A performance comparison between a novel piezoprobe and the piezocone in Boston Blue Clay" SM. Thesis, Massachusetts Institute of Technology, Cambridge, MA.

[73] Vesic, A.S. (1972). "Expansion of cavities in infinite soil mass" Journal of Soil Mechanics and Foundation Engrg., 98 (SM3), 265-290.

[74] Viggiani, C. (1970). "Discussion of 'An analysis of consolidation theories'" by. Schiffman, R.L., Chen, A.T.F. & Jordan, J.C., ASCE Journal of the Soil Mechanics and Foundations Division, 96, 331-334.

[75] Whittle, A.J. (1987). "A model for predicting the behavior of overconsolidated clays with application to the cyclic loading of friction piles" Ph.D. Thesis, Massachusetts Institute of Technology, Cambridge, MA.

[76] Whittle, A.J. (1993). "Assessment of an effective stress analysis for predicting the performance of driven piles in clay" Offshore Site Investigation and Foundation Behavior, Society for Underwater Technology, London, 28, 607-643.

[77] Whittle, A.J. & Kavvadas, M.J. (1994). "Formulation of MIT-E3 constitutive model for overconsolidated clays" ASCE Journal of Geotechnical Engineering, 120 (10), 173-198.

[78] Woodward, R.J., Lundgren, R. & Boitano, J.D. (1961). "Pile loading tests in stiff clays" Proceedings 5th ICSMFE, Paris, France, 2,177-184.

[79] Zeevaert, L. (1959). "Discussion of effect of driving piles into soft clay by Cummings et al." ASCE Trans., 115, 287-292.

APPENDIX A: COMPUTER PROGRAMS

A.1 INTRODUCTION

Appendix A contains the descriptions, manuals and listings of various computer programs modified by the author and used in this thesis. These programs are coded according to the 1977 standard for Fortran (Fortran 77).

This Appendix contains the following programs:

1. A computer program for the cylindrical Cavity Expansion Method (CEM)
2. A computer program for the Strain Path Method (SPM)

Both computer programs use a generic library (Release 8.0) which contains all the subroutines associated with the effective soil models implemented into these programs.

A.2 COMPUTER PROGRAM FOR CEM

This program computes the effective stresses and excess pore pressures during the undrained expansion of a cylindrical cavity using one of the following soil models:

1. Linear Isotropic Model
2. Modified Cam-Clay
3. MIT-E1
4. MIT-E3
5. MIT-S1

The program reads the initial values of the state variables required by the model to be used in the analysis and the number and location of points where stresses and pore pressures will be computed. It prints the effective stresses, excess pore pressures and remaining state variables at these points.

A.2.1 User's manual

The program reads input from units 09 and 28. More specifically, the input files related to the MIT-S1 are described herein.

Unit 09 contains the input parameters of the soil model used in the analysis. For MIT-S1, data should be put according to *Table A.1*.

Line #	Variable	Entry
1	ρ_c	rhoc
	C_b	xkb
	σ_{ref}	sigref
	θ	theta
2	$2G/K = 3\cdot\left(1-2\mu/1+\mu\right)$	xnu
	K_0	Ko
	φ_{cs}	phitc
3	m	m
	φm	phimax
	ψ	psi
	p	PQ
4	r	r
	D	D
	ω	w
	ω_s	w2
5	p	gamma
	h	hpo

Table A.1: Input material properties used by the MIT-S1 model

Unit 28 contains the initial conditions and specifically for MIT-S1 is described in the following:

- First line lists the initial stresses, i.e. σ_r, σ_z, σ_θ, σ_{rz}, $\sigma_{z\theta}$, $\sigma_{\theta r}$.
- Second line lists the initial conditions. Accordingly:
  - nsurf: position of the initial stress point, (0 inside yield surface, =1 on the yield surface)
  - alpha: initial size of yield surface (mean initial pressure)
  - e: initial void ratio
  - itip: position of the initial stress point if on the yield surface. 1 implies that initial state is at the tip of the yield surface, 0 implies that initial stress state is not at the tip the yield surface, so exact position needs to be specified on the third line.
  - irev = 0 Reads conditions of SRP (Stress Reversal Point), > 0 implies that initial state is a SRP, -1 Consolidated along Radial Path
- Third line lists the anisotropy tensor in case that the initial stress point is not at the tip of the yield surface.
- The next "n" lines lists the radial coordinates, r_o/R (normalized with the pile radius) of points where program output is computed.

A.2.2 Program output

The program outputs "n" on each of the units 18 and 19. The unit 19 is not used in case of the Linear Isotropic Model. Based on the same logic, only the output files related to MIT-S1 will be reported thoroughly thereafter.

Each record on unit 18 contains information for a point, starting from the point located at the largest distance from the pile. It contains:

1. The radial coordinate r_o/R (normalized with the pile radius)
2. The excess pore pressure
3. The mean effective stress
4. The transformed deviatoric stress components S_1 and S_2

Finally, each record on unit 19 contains the following information:

1. The value of variable "nsurf"
2. The value of variable "alpha"
3. The value of the variables b_1 and b_2

A.2.3 Program listing

```
c      ************************************************************
c      *      Program to Compute Effective Stresses and Pore      *
c      *      Pressures during the Undrained Expansion of a       *
c      *                    Cylindrical Cavity                    *
c      *                                                          *
c      *                  Models implemented:                     *
c      *                                                          *
c      *          model=1......Linear Isotropic model             *
c      *          model=2......MCC                                *
c      *          model=3......MIT-E1                             *
c      *          model=6......MIT-E3                             *
c      *          model=11.....MIT-S1                             *
c      *                                                          *
c      *          Update Aug 16th,2011    D.G. Niarchos           *
c      *                                                          *
c      ************************************************************
c
      implicit real*8(a-h,o-z)
      common /state/ sigma,s(5),n,nsurf,alpha,nsurf2,alpha2,bo,b(5),
     1               prop(30),bk,two_g,vr,sv,cpor,vro,svo
      common /s1mdl/ mdmits,xn(5),xj3n,xnn,x2nb,bb,xx2,c2,dj3dn(5)
      common /hys_b/ sigrev,xnrev(5),evdd,edd(5),ekk,xnuh,pr,pri,
     1               sigmar,sr(5),xx,alphoi,alpho,bki,two_gi
      common /test / ex ,ey(5), evol,octgam,dgammax,gammax, es,
     1               taux,tau(5),tsigma,  octq, deltaq,  qmax, qx,
     2               fevd,fed(5),px,u,xcyc,idx,idz
      dimension      x(51),ed(5),srev(5),a(5),arev(5),ds(5)

      character*40 name09,name28
c
      data two,six/0.7071067812d0,0.4082482905d0/
c
      write (*,157)
157       format ('  Input factor vs (=1 CEP, 0.0975 for B/t=40:')
      read (*,*) vs
      write (*,16)
16    format (' Input filenames, unit09,unit28 :')
      read (*,*) name09,name28
      write (*,17)
17    format (' Input model , No of points :')
      read (*,*) model,np
c
      open (unit=28,file=name28,status='old')
c
      open (unit=09,file=name09,status='old')
      call read_model_properties (model)
      close (09)
c
c     Initialize state variables
c
      call init_routine (model)
      alphoi=alpha
      ao=0.d0
      evdd=0.d0
      do 119 i=1,3
119       edd(i)=0.d0
      p=0.d0
c
      x(np+1)=200.d0
c
c       read normalized with pile radius coordinates
c
      do 15 i=1,np
      read (28,*) x(i)
15    continue
      evd=0.d0
      ed(1)=0.d0
      e2=0.d0
c
      open (unit=18,file='stress',status='new')
      open (unit=19,file='sstate',status='new')
c
      do 100 i=np,1,-1
c     write (9,*) i
      dum=x(i)
      if (x(i).lt.1.0001d0) dum=1.0001d0
      dum=1.d0/dum
      dum=two*dlog(1.d0-vs*dum*dum)
      ed(2)=dum-e2
      e2=dum
      if (model.eq.1) go to 30
c
c     Adjust dlimit
c
      dlimit=1.d-5
c
      call maxinc( evd,ed,3,dlimit,ndiv)
c
30    call model_lib (model,evd,ed,ndiv)
c
c         Compute pore pressure
c
```

```
      dx=x(i)-x(i+1)
      dum=dlog(x(i+1)/x(i))
      dum=dum*(dx*s(2)-x(i)*ds(2))/(dx*two)
      p=p-dsig+six*ds(1)+3.d0*two*ds(2)-dum
      taux=sigma
      tau(1)=s(1)
      tau(2)=s(2)
      tau(3)=0.d0
      tau(4)=0.d0
      tau(5)=0.d0
      call convert (1,1,2,taux,tau)
      write (*,*) i,np,x(i),p
      write (18,145) x(i),p,taux,tau(1),tau(2),tau(3)
3     format (1x,d14.6,4d16.8)
145   format (1x,d14.6,6d16.8)
      if (model.eq.1) go to 100
      if (model.ge.3) go to 21
      write (19,4) nsurf,alpha
      go to 100
21    write (19,4) nsurf,alpha,b(1),b(2),b(3)
4     format (1x,i4,4d16.8)
100       continue
      close(17)
      close(18)
      close(19)
      stop
      end
```

A.3 COMPUTER PROGRAM FOR SPM

This program computes the effective stresses and the remaining state variables across a cylindrical pile, using the Strain Path Method and one of the following soil models:

1. Linear Isotropic Model
2. Modified Cam-Clay
3. MIT-E1
4. MIT-E3
5. MIT-S1

The program processes the strains along a specific stream-line around the tip of the pile and uses the specified soil model to compute the effective stresses and the remaining state variables at each nodal point of the stream-line. After processing the specific stream-line, the program continues to the next stream-lie, where the computations are resumed.

A.3.1 User's manual

The program reads input from units 09, 10, 11 and 28. The input files related to MIT-S1 are listed below.

Unit 09 contains the input parameters of the soil model used in the analysis and its contents are mentioned in *Section A.2.1*.

Unit 10 contains the following control information:

- Type of model

- model = 1; Linear Isotropic Model
- model = 2; Modified Cam-Clay
- model = 3; MIT-E1
- model = 6; MIT-E3
- model = 11; MIT-S1

- Type of output
  - iout = 0; output last data point only for each-stream-line
  - iout = n; output every n^{th} point
- Input file names
- Number of nodal points per streamline (incr) and number of streamlines (nslines)

Unit 11 contains "incr" number of records for each stream-line. Each record contains information for a point along the stream-line starting from points in front of the pile:

- The axial coordinate z (the origin is located at the tip of the pile and the positive z-axis is upwards)
- The radial coordinate r_o/R (the origin is located along the axis of the pile) normalized with the pile radius
- The strain increments $\Delta\varepsilon_z$, $\Delta\varepsilon_r$, $\Delta\varepsilon_\theta$ and $\Delta\varepsilon_{rz}$

Unit 28 follows the same format as the one acknowledged in *Section A.2.1*, except for the last "n" lines including information regarding the radial coordinates, r_o/R.

A.3.2 Program output

The program outputs records on units 29 and 30 (unit 30 is used only if model > 1). Each record contains information for each nodal point of the streamline. Thus, the

number of records outputted on each unit is equal to the number of nodal points (incr) times the number of stream-lines (nslines).

Each record on unit 29 contains:

1. The radial coordinate r_o/R (normalized with the pile radius)
2. The axial coordinate z
3. The effective stresses, i.e. σ_r, σ_z, σ_θ, σ_{rz}

Each record on unit 30 contains:

1. The value of variable "nsurf"
2. The value of variable "alpha"
3. The value of the variables b_1, b_2 and b_3

A.3.3 Program listing

```
c       ************************************************************
c       *      Program for Pile Driving using the Strain Path      *
c       *        method. It computes the Effective Stresses        *
c       *                    far behind the tip of                 *
c       *                     a cylindrical pile.                  *
c       *                                                          *
c       *             MODELS IMPLEMENTED:  (model)                 *
c       *                                                          *
c       *          model=1......Linear Isotropic model    1991     *
c       *          model=2......Modified Cam-Clay         1991     *
c       *          model=3......MIT-E1 (R1.0) & (R2.0)             *
c       *          model=6......MIT-E3 (R4.0)             1992     *
c       *          model=11.....MIT-S1 (R1.0)             1993     *
c       *                                                          *
c       *          Update Sep 7th,2010    D.G. Niarchos            *
c       *                                                          *
c       ************************************************************
c
        implicit real*8(a-h,o-z)
        common /state/ sigma,s(5),n,nsurf,alpha,nsurf2,alpha2,bo,b(5),
     1                 prop(30),bk,two_g,vr,sv,cpor,vro,svo
        common /simdl/ mdmits,xn(5),xj3n,xnn,x2nb,bb,xx2,c2,dj3dn(5)
        common /hys_b/ sigrev,xnrev(5),evdd,edd(5),ekk,xnuh,pr,pri,
     1                 sigmar,sr(5),xx,alphoi,alpho,bki,two_gi
        common /test / ex ,ey(5), evol,octgam,dgammax,gammax, es,
     1                 taux,tau(5),tsigma,  octq, deltaq,  qmax, qx,
     2                 fevd,fed(5),px,u,xcyc,idx,idz
        dimension      ed(5),srev(5),a(5),arev(5),ds(5)
        character*40 name09,name28,name11
c
        open(unit=10,file='pdrive.dat',status='old')
        read (10,*) model
c-----------------------------------------------------------------------
c     read output data
c     iout=0 - output last data point only for each streamline
c     iout=n - output every nth point
c     iout.lt.0 - output data at a specified elevation
c-----------------------------------------------------------------------
        read(10,*)iout
        if(iout.lt.0)read(10,*)zout
c
        read(10,*)name09
        read(10,*)name28
        read(10,*)name11
c
        open(unit=09,file=name09,status='old')
        open(unit=28,file=name28,status='old')
        open(unit=11,file=name11,status='old')
c
c...  Read number of strain steps along the streamlines
c
        read (10,*) incr,nslines
c
c       Read model properties
c
        call read_model_properties (model)
c
c-----------------------------------------------------------------------
c...  Outer loop
c-----------------------------------------------------------------------
c
100     do 250 jj=1,nslines
c
c...  Initialize state variables.
c
        write (18,*) jj
c
        call init_routine (model)
c
        rewind (28)

            evdd=0.d0
            do 22 i=1,3
               edd(i)=0.d0
22          continue
c-----------------------------------------------------------------------
c       Main LOOP
c-----------------------------------------------------------------------
            nnn=0
            e1=0.d0
            e2=0.d0
        e3=0.d0
c-----------------------------------------------------------------------
c...  Inner Loop
c-----------------------------------------------------------------------
        do 200 i=1,incr
        nnn=nnn+1
c
        write (19,*) i
c
c...  Read coordinates z,r and strain increments dez,der,det,derz.
c
```

```
c...  streamline data read from file11
      read (11,4) zzz,rrr,ed(1),evd,ed(2),ed(3)
c...  beware format of input
4     format (f10.5,f10.6,f14.10,f14.10,f14.10,f14.10)
c
      call convert (0,0,3,evd,ed(1),ed(2),ed(3))
          de1=ed(1)
          de2=ed(2)
      de3=ed(3)
      evd=0.d0
      dum=dabs(ed(3))
      do 52 j=1,2
         zum=dabs(ed(j))
         if (zum.gt.dum) dum=zum
52      continue
c
      dlimit=1.d-7
c
      call maxinc( evd, ed, 3, dlimit, ndiv)
c
      call model_lib (model,evd,ed,ndiv)
c
      e1=e1+de1
      e2=e2+de2
          e3=e3+de3
      ee=dsqrt(e1*e1+e2*e2+e3*e3)
      ee2=dsqrt(edd(1)*edd(1)+edd(2)*edd(2)+edd(3)*edd(3))
c
            if(nnn.eq.iout)then
               nnn=0
               taux=sigma
               tau1=s(1)
               tau2=s(2)
               tau3=s(3)
c
               call convert (1,1,3,taux,tau1,tau2,tau3)
c
               write (29,1031) rrr,zzz,taux,tau1,tau2,tau3
               write (30,1032) nsurf,alpha,b(1),b(2),b(3)
c
               if(model.eq.2) then
                                   write (30,113) nsurf,alpha
                               endif
c
               if(model.eq.5)then
                   write (30,106) 0,ao,alphoi,ekk
                   write (30,104) alpha,a(1),a(2),a(3)
                   write (30,104) sigrev,srev(1),srev(2),srev(3)
                   write (30,104) alphrev,arev(1),arev(2),arev(3)
                   write (30,104)evdd,edd(1),edd(2),edd(3)
               endif

            endif
c
 200     continue
c...  %%%%%%%%%%%%%%%%%%%%%%%%%%%%%%%%%%%%%%%%%%%%%%%%%%%%%%%%%%%%%%%%
c
         if(iout.eq.0)then
c
            taux=sigma
            tau1=s(1)
            tau2=s(2)
            tau3=s(3)
            call convert (1,1,3,taux,tau1,tau2,tau3)
c
            write (29,103) rrr,taux,tau1,tau2,tau3
c
            if(model.eq.2) then
                                   write (30,113) nsurf,alpha
                         endif
c
            if(model.eq.5)then
              write (30,106) nsurf,ao,alphoi,ekk
              write (30,104) alpha,a(1),a(2),a(3)
              write (30,104) sigrev,srev(1),srev(2),srev(3)
              write (30,104) alphrev,arev(1),arev(2),arev(3)
              write (30,104)evdd,edd(1),edd(2),edd(3)
            endif
c
 1031          format (2(f10.5,1x),4(d24.16,1x))
 1032          format (i3,7(f10.5,1x))
 103           format (2f11.6,6d15.7)
 107           format (2f11.6,6d15.6)
 104           format (4d25.17)
 106           format(i3,3d25.17)
 113           format (i3,d25.17)
c
         endif
 250   continue
c...  %%%%%%%%%%%%%%%%%%%%%%%%%%%%%%%%%%%%%%%%%%%%%%%%%%%%%%%%%%%%%%%%
       stop
       end
```

APPENDIX B: INTERSECTION SUBROUTINE

B.1 INTRODUCTION

Appendix B contains the complete listing of the subroutine developed by the author to determine the intersection point when the current stress point crosses the bounding surface. The program is coded according to the 1977 standard for Fortran (Fortran 77).

This subroutine is part of the user-defined subroutine responsible for the integration of MIT-S1 in ABAQUS.

B.2 PROGRAM LISTING

```
      subroutine mits1_intersect
     *          (c2,c2a,c2b,zm,sigma,s,n,alpha,b,xn,sigmad,sd,f,y,
     *           noel,npt)
c     ------------------------------------------------------
c     - * Computes intersection with yield/bounding surface  -
c     -   Update: July 7th,2011       Dimitrios G. Niarchos  -
c     ------------------------------------------------------
      implicit real*8(a-h,o-z)
      dimension s(5),ts(5),as(5),bs(5),xs(5),b(5),sd(5),xn(5),
     *          txn(5),xxn(5),dj3dn(5)

c     - * Computes value of yield function before crossing.
      tsigma= sigma - sigmad
      do 1 i=1,n
      ts(i) = s(i) - sd(i)
1     txn(i) = ts(i)/tsigma
      call mits1_auxiliar (c2a,c2b,txn,n,b,
     *                     tc2,txj3n,txnn,tx2nb,tbb,txx2)
      fold  = txnn - tc2 + txx2*(tsigma/alpha)**zm
c     - * Computes lower (b) and upper (a) boundary.
      asigma = sigma
          do 2 i=1,n
2     as(i) = s(i)
      bsigma = tsigma
          do 3 i=1,n
3     bs(i) = ts(i)
      if(fold.lt.0) goto 5
      yx = alpha/tsigma * ((tc2-txnn)/txx2 )**(1.d0/zm)
      sigma = sigma*yx
      do 4 i=1,n
4     s(i) = s(i)*yx
      return

c     ------------------------------------------------------
c     -       Main Loop for finding intersection           -
c     -            Dimitrios G. Niarchos                   -
c     -                 7 JUL 2011                         -
c     ------------------------------------------------------
5     do 30 iter=1,100
      xsigma = asigma - 0.5d0*(asigma-bsigma)
      do 10 i=1,n
      xs(i) = as(i) - 0.5d0*(as(i)-bs(i))
10    xxn(i) = xs(i)/xsigma
      if (xsigma.lt.0.d0) then
             xsigma = 0.d0
             do 12 i=1,n
12           xs(i) = (asigma*bs(i)-bsigma*as(i))/(asigma-bsigma)

                 asigma = xsigma
             do 15 i=1,n
15           as(i) = xs(i)
             goto 5
      endif
      call invariant_xj3 (xxn,n,xj3)
      xc2 = c2a + c2b*xj3
      call mits1_yield (xc2,zm,xsigma,xxn,n,alpha,b,fx)
      if (fx.gt.0.d0) then
         asigma = xsigma
         do 20 i=1,n
20       as(i) = xs(i)
      else
               bsigma = xsigma
         do 25 i=1,n
25       bs(i) = xs(i)
      endif
      DO I=1,N
      WRITE(74,*)B(I),XS(I)
      ENDDO
      if (dabs(fx).lt.1d-5) then
                y = 1.d0-dabs((xsigma-tsigma)/sigmad)
         WRITE(74,*)'inside MITS1_INTERSECT5',NOEL,NPT
         WRITE(74,*)y
         goto 50
30    endif
      write(73,*) ' It didnot converge finding intersection.'
      write(73,*) ' Note: It didnot converge finding intersection.'

50    write(73,*)'NOEL',noel,'NPT',npt
      write(73,1000) iter,sigma,alpha,xn(1),b(1),y
      return
1000  format(' Intersect,iter=',i4,' sigma,alpha,xn,b,y ',5f12.5)
      end
```